UC Santa Barbara
UC Santa Barbara Electronic Theses and Dissertations

Title

Ultra-Clean Mesoscopic Devices in Graphene van der Waals Heterostructures in the Quantum Hall Regime

Permalink

https://escholarship.org/uc/item/4880f6s0

Author

Cohen, Liam Augustus

Publication Date

2024

Peer reviewed|Thesis/dissertation

eScholarship.org Powered by the California Digital Library
University of California

University of California
Santa Barbara

Ultra-Clean Mesoscopic Devices in Graphene van der Waals Heterostructures in the Quantum Hall Regime

A dissertation submitted in partial satisfaction
of the requirements for the degree

Doctor of Philosophy
in
Physics

by

Liam Augustus Cohen

Committee in charge:

Professor Andrea Young, Chair
Professor Chetan Nayak
Professor Zhenghan Wang
Professor Chenhao Jin

March 2024

The Dissertation of Liam Augustus Cohen is approved.

Professor Chetan Nayak

Professor Zhenghan Wang

Professor Chenhao Jin

Professor Andrea Young, Committee Chair

March 2024

Ultra-Clean Mesoscopic Devices in Graphene van der Waals Heterostructures in the Quantum Hall Regime

Copyright © 2024

by

Liam Augustus Cohen

For my Mother, Father, and Claire...

I would not be where I am today if not for your love and support. I love you all more than I could possibly express.

Acknowledgements

The myth of the lone mad-scientist plodding along in their lab, turning knobs and pushing the boundaries of mankind's knowledge does not fit the description of any modern day physicist. I am, of course, no exception to this, and as such there is a long list of people without which my journey thus far would not have been possible.

I would like to start with Alex Potts. You have been one of my closest friends ever since I first arrived at UCSB and we have been in the trenches together ever since. From conquering our P.I.'s condensed matter class to impossibly late nights in the nanofab, we have surmounted many challenges together and consoled each other in many defeats. I will always appreciate your eager ear when I have pontificated on crazy ideas or lamented about experimental frustrations, and I am thankful for all of your helpful suggestions. I am also thankful for our impossibly time inefficient lifting sessions discussing life and physics; they often provided a much needed escape and boost of motivation when I needed it. I'm disappointed that you reached the finish line before me and we were not able to graduate together like we always thought, but I'm so excited to see what you accomplish at Max Planck, Columbia, and beyond; I know it will be amazing.

Noah Samuelson, you also deserve your own paragraph. You are truly one of the most brilliant and hard working scientists I have ever had the pleasure to work with. Without you my PhD would not nearly have been as successful. I appreciate the endless number of conversations we have had discussing our results in the Broida parking lot at 2AM, wanting to go home and sleep, but being drawn back by the excitement of the phenomena we were discovering. I appreciate your intelligence, humor, and the level of excitement and passion you bring when our experiments were working. I also appreciate your steadfast work ethic when everything was broken (which was most of the time), as well as allowing me to complain endlessly. Writing this thesis, it's become evident

that we have accomplished something rather remarkable together; we have managed to accelerate graphene mesoscopics beyond the state of the art of its competing platforms, touched on some key physics results, and possibly even breathed new life into a field that had not seen much progress in a decade. This, truly, again is something that would not have happened without you. I am looking forward to seeing what the remainder of your PhD brings, and I hope that we continue to collaborate for the rest of our careers. Finally, I am thankful for you being a great friend as well as watching Emmy and giving her lots of attention while I was not around.

I would like to thank my early mentors, Eric Spanton, Sasha Zibrov, Haoxin Zhou, Gregory Polshyn, and Fangyuan Yang who all helped me get set up in my early days in the lab, who taught me how to exfoliate, stack, and do nanofab. I would also like thank Charles Tschirhart who has let me distract him for many hours with random ideas, discussions, and a long running debate on the existence of edge states. Also, Marec Serlin who helped me as a TA work through my first condensed matter class here at UCSB.

There are many other people in the lab who have all made it a joy to come into work every day, and I appreciate the infectious passion and dedication that is palpable from every one of you. To Trevor Arp, Ludwig Holleis, Evgeny Redekop, Caitlin Patterson, Heun Mo Yoo, Youngjoon Choi, Yi Guo and Owen Sheekey, thank you. To Yu Saito, Ben Xie, Yiftach Frenkel, Charles Zhang, Toby Chu, Wenting Gong, and Isabella Catanzaro, who have already left the lab, thank you for making my time here wonderful.

I would also like to mention specifically a few additional people working on "Team Quantum Hall," who have contributed to the success of this project. Firstly, Alexandre Assouline, it was a pleasure working with you. There were many great ideas born from our discussions, and although we did not get to work on quantum dots together as originally planned, I'm sure you will do incredible science at CNRS as you put together your own

group. Second, Will Wang, who would have thought a simple conversation at March Meeting would lead to one of the most productive summers I have ever seen. While you have only been here for a short while, you have already had an incredible impact on this project and I think you are going to have a crazy exciting PhD. To Marco Valentini, you are the next generation – there are so many interesting ideas and experiments to try, and you have already demonstrated an incredible passion and drive that I know will produce some amazing physics. I cannot think of a better person to pass the torch on to.

I would like to thank our theorist on call, Taige Wang. You were always willing to get a random slack message from me asking "can you simulate this?" Then a few days later you would already be done. Thank you for your collaboration on all of my projects and always being available for discussion and providing key insights when needed.

Coming towards the end I would like to thank my "second advisor," Mike Zaletel. Discussions with you have always been extremely fruitful and your ideas for different experiments to perform have been exceptionally insightful. Your genuine excitement about our results was infectious and provided motivation when needed; there's nothing better than someone processing your data and sending you a slack message saying "this is so bad-ass."

Outside of the lab I would like to thank my mom and dad who have been nothing but supportive and loving throughout the last six years (and all the time before that). You guys helped me through all the lows even when I did not want to be helped - I will be forever grateful for you guys giving me the tools to follow my dreams. I would also like to thank my girlfriend Claire. The sacrifice you have made allowing me to pursue a PhD at UCSB while you live in New York will be something I will be thankful for, for the rest of my life. Your love and support allowed me to get through the most challenging parts of this endeavor. I would also like to thank my two dearest friends in the world, Charles Simpson-Brown and Jeremy Conway who are like my brothers and who have

always pushed me up. To all of you, I love you so much, and I would not be who I am without all of you.

Finally, I would like to thank my advisor, Andrea Young. When I first came to UCSB, I did not really know who I was. I applied to graduate school trying to both be a theorist and an experimentalist, which ultimately lead to a muddled, confused, and poorly written set of graduate applications. I was rejected from every school that I applied to, however, my undergraduate advisor, Ray Ashoori, managed to get my application in front of Andrea. Andrea, you gave me a chance when my sense of self was crumbling to dust faced with a stream of failure. I will always be grateful for that opportunity. Moreover, I have grown immensely as a scientist working in your group. I've improved as an experimentalist, as a writer, and as a communicator thanks to your attention to detail, focus, and genuine excitement about the physics we are pursuing. I am fortunate to have found my way into your lab, thank you for the last six years.

Curriculum Vitæ
Liam Augustus Cohen

Education

2024	Ph.D. in Physics (Expected), University of California, Santa Barbara.
2021	M.A. in Physics, University of California, Santa Barbara.
2018	B.Sc. in Physics and Electrical Engineering/Computer Science, Massachusetts Institute of Technology

Publications

2024 — Liam A. Cohen, Noah L. Samuelson, Will Wang, Simon Blanch, Taige Wang, Takashi Taniguchi, Kenji Watanabe, Michael P. Zaletel, and Andrea F. Young., *Anyonic statistics and slow quasiparticle dynamics in a graphene fractional quantum Hall interferometer*, **manuscript in preparation**

2024 — Liam A. Cohen, Noah L. Samuelson, Taige Wang, Takashi Taniguchi, Kenji Watanabe, Michael P. Zaletel, and Andrea F. Young., *Spontaneous localization at a potential saddle point from edge state reconstruction in a quantum Hall point contact*, **pre-print**, arXiv:2401.10433

2024 — Alexandre Assouline, Taige Wang, Haoxin Zhou, Liam A. Cohen, Fangyuan Yang, Ruining Zhang, Takashi Taniguchi, Kenji Watanabe, Roger S.K. Mong, Michael P. Zaletel, and Andrea F. Young, *Energy Gap of the Even-Denominator Fractional Quantum Hall State in Bilayer Graphene*, Phys. Rev. Lett. 132, 046603 (2024)

2023 — Liam A. Cohen, Noah L. Samuelson, Taige Wang, Takashi Taniguchi, Kenji Watanabe, Michael P. Zaletel, and Andrea F. Young., *Universal chiral Luttinger liquid behavior in a graphene fractional quantum Hall point contact*, Science 382, 542-547(2023)

2023 — Liam A. Cohen, Noah L. Samuelson, Taige Wang, Kai Klocke, Cian C. Reeves, Takashi Taniguchi, Kenji Watanabe, Sagar Vijay, Michael P. Zaletel, and Andrea F. Young, *Nanoscale electrostatic control in ultraclean van der Waals heterostructures by local anodic oxidation of graphite gates*, Nat. Phys. 19, 1502–1508 (2023)

2022 Haoxin Zhou, Ludwig Holleis, Yu Saito, Liam Cohen, William Huynh, Caitlin L. Patterson, Fangyuan Yang, Takashi Taniguchi, Kenji Watanabe, and Andrea F. Young., *Isospin magnetism and spin-polarized superconductivity in Bernal bilayer graphene.* Science 375, 774-778(2022)

Abstract

Ultra-Clean Mesoscopic Devices in Graphene van der Waals Heterostructures in the Quantum Hall Regime

by

Liam Augustus Cohen

A successful program for improving the quality of graphene based 2DEGs has been the steady removal of charged impurities near the graphene surface. This was first accomplished by using hBN as a substrate and encapsulant, and then further improved by using atomically uniform graphite as a gate electrode instead of amorphous evaporated metal, resulting in the first all 'van der Waals' heterostructure. These improvements lead to the robust observation of even-denominator fractional quantum Hall states in bilayer graphene, as well as many other interesting correlated ground states at zero magnetic field such as superconductivity and ferromagnetism in both twisted and un-twisted graphene multi-layers. Moreover, as many of these states occur at an electron density near charge neutrality, they may be accessed within a single device simply by field-effect gating. However, engineering more complex mesoscopic devices which are designed to interface these exotic phases of electronic matter require fabricating spatially varying potential profiles on the order of the correlation lengths in these systems, typically around 100nm. Additionally, these manufactured potentials need to be energetically uniform, i.e., they must not introduce uncontrolled disorder potentials on the order of the energy gaps of the systems of interest, again typically around 1meV, on the requisite length scales. Here we report on a novel fabrication technique, AFM based local anodic oxidation gate lithography, to pre-pattern graphite gates with critical feature sizes smaller than 100nm which does not introduce any unwanted contaminants or damage to the underlying van der

Waals heterostructure. We then use this technique to fabricate two types of mesoscopic devices operated in the fractional quantum Hall regime, a quantum point contact and an edge-state Fabry-Pérot interferometer. We show that our quantum point contact nearly perfectly mimics a simple model which characterizes electron tunneling between $\nu = 1/3$ and $\nu = 1$ edge modes at any tunneling strength. This indicates that these junctions are nearly disorder-free validating our novel fabrication technique. Moreover, we use our nearly defect free junctions to create an edge-state Fabry-Pérot interferometer operating in $\nu = 1/3$. Here we observe sharp phase jumps in the interference pattern consistent with the expected braiding phase of anyons in the $\nu = 1/3$ state. These results taken together show that our method for fabricating mesoscopic devices within the graphene based van der Waals heterostructure platform, developed over the last four years, makes these devices comparable to the most modern III-V semiconductor quantum wells, which took over 30 years of refinement.

Contents

Curriculum Vitae **ix**

Abstract **xi**

1 Introduction **1**
1.1 How to Read this Thesis 1
1.2 A Note to Future Graduate Students 3
1.3 Overview 4

2 AFM Based Local Anodic Oxidation Lithography of Graphite Gates **9**
2.1 Overview 9
2.2 Atomic Force Microscope Actuated Local Anodic Oxidation Lithography of Graphite (LAFM-AOGL) 17
2.3 Multi-layer Alignment via "Slip-n'-Slide" of AFM Cut Gates 23
2.4 Outlook and Pathways to Improvement in Consistency 26
2.5 Permissions and Attributions 29

3 Quantum Point Contacts in Graphene van der Waals Heterostructures **30**
3.1 Overview 30
3.2 Introduction 31
3.3 Fabrication 33
3.4 Partitioning of Integer Quantum Hall Edge Modes 35
3.5 Partitioning of Fractional Quantum Hall Edge Modes 42
3.6 Tuning Edge Sharpness *in situ* 48
3.7 Additional Effects of Edge State Reconstruction: Spontaneously formed Quantum Dots at an Electrostatic Saddle Point 52
3.8 Demonstration of Universal Chiral Luttinger Liquid Behavior at $\nu = 1/3$ Edge in the Sharp Edge Limit 67

3.9 Perfect Andreev Scattering of e/3 Quasi-particles at a $\nu = 1/3$ to $\nu = 1$ Point Heterojunction 73
3.10 Comparison of Tunneling Characteristics of a $\nu = 1/3$ to $\nu = 1$ Heterojunction to an Exactly Solveable Quantum Impurity Model 75
3.11 Nearly Adiabatic $\nu = 1/3$ to $\nu = 1$ Heterojunction - Making a Dissipationless, Passive, DC Step-up Transformer 79
3.12 Permissions and Attributions 82

4 Edge State Interferometers in Graphene van der Waals Heterostructures 83
4.1 Overview 83
4.2 Introduction 85
4.3 Fabrication and Device Geometry 86
4.4 Interference and Measurement of θ_a at $\nu = 1/3$ 88
4.5 Quasi-particle Dynamics in $\nu = 1/3$ 93
4.6 Evolution of Phase Slips in $\nu = -1$ and Localization Transitions 96
4.7 Measurements at fixed B and A_I but different N_{qp} 101

A Appendix A: QPC Fabrication 105

B Appendix B: Measurement Methods 110
B.1 QPC Experiments Chapter 3, Sections 3.3 - 3.6 110
B.2 QPC Experiments Chapter 3, Section 3.7 111

C Appendix C: Analysis and Supplementary Information for Chapter 3 113
C.1 Paritioning FQH Edge Modes 113
C.2 Luttinger Liquid Tunneling Data Analysis 115
C.3 Universal Chiral Luttinger Liquid Behavior at a Graphene Fractional Quantum Hall Point Contact 117
C.4 Junction Electrostatics: Reconstruction Effects and Resonant Scattering 117
C.5 DC Voltage Transformer from FQH Andreev Scattering 124
C.6 Data Analysis 127
C.7 Additional Data at a different magnetic field 136
C.8 Excess Conductance Observed in IQH-FQH Heterojunctions with $\nu_{FQH} < 1/2$ 138

D Appendix D: Nanofabrication Procesess and Recipes 141
D.1 AFM Cutting Recipes 141
D.2 Lithography and Lift-off of Metal Finger Gates for Quantum Dots 142

Bibliography 144

1

Introduction

1.1 How to Read this Thesis

This thesis is divided up into five main sections. Section I. is the introduction and contains some general overview and current state of the field.

Section II reviews the van der Waals assembly process used in all the devices presented in this work. In particular it focuses primarily on atomic force microscopy based local anodic oxidation gate lithography (AFM-AOGL), the key technological advance which has enabled all of the experiments presented in this thesis. The chapter introduces

the motivation behind the technique as well as demonstrating the various device geometries that may be fabricated using it. Some additional related van der Waals assembly techniques are covered.

Section III describes experiments on an all van der Waals quantum point contact (QPC) in the quantum Hall regime. This section provides a brief overview of the fabrication specific to making a QPC. This section will primarily cover the contents published in, Cohen, Samuelson et al., *Nanoscale electrostatic control in ultraclean van der Waals heterostructures by local anodic oxidation of graphite gates*, Nature Physics; Cohen, Samuelson et al., *Universal chiral Luttinger liquid behavior in a graphene fractional quantum Hall point contact*, Science, and Cohen, Samuelson et. al *Spontaneous localization at a potential saddle point from edge state reconstruction in a quantum Hall point contact*, ArXiv. I will discuss the effects of edge state reconstruction and how they may be mitigated in the presented device geometry, our measurements of edge state tunneling in the fractional quantum Hall regime, as well as the peculiar consequences of charge fractionalization in a quantum Hall QPC.

Section IV. discusses the natural evolution of the experiments presented in section III, i.e., edge state Fabry-Pérot measurements. These experiments require two ultraclean QPCs in series to form a resonant cavity. The section begins similarly to section III discussing the fabrication process specific to the Fabry-Pérot devices. Second, this section presents measurements of highly robust interference in the integer and fractional quantum Hall regimes in monolayer graphene as well as measurements of the anyon phase. The delicate interplay between bulk-edge coupling and non-equilibrium charging effects is discussed.

The appendices A-D include specific recipes for nanofabrication as well as experimental procedures and analysis which should aid anyone attempting to reproduce or extend our results.

1.2 A Note to Future Graduate Students

Before starting to write this thesis, I put some thought into who the audience would be. I came to the conclusion that, most likely, the person reading this thesis – in particular someone who bothered to read the introduction – is a future member of Andrea's lab getting oriented and just starting out on their path to a doctorate. So I thought it would be appropriate, before getting into the physics, to leave a note to his future graduate students.

Take a deep breath. Everything is going to be okay. The journey to getting a physics PhD is a long and arduous one, and it is best to take it step-by-step. More likely than not, you will make stupid mistakes, and if you are anything like me, you will make the same one more than once. Trust me, the stories of failure in this lab can easily fill up volumes. As you progress you will break things, experiments will fail, and devices or experiments you have worked hours, days, weeks, or even months on will blow up right when you are most vulnerable. You will be left, frustrated, lost, hopeless, and feeling like you have two functioning brain-cells and one is on vacation. However, all of this is to say that you are not the only one who has or will feel like this – it is a nearly ubiquitous experience for all graduate students, and you are not alone.

When things are at their most difficult, just remember research is about uncovering new knowledge and doing something that has *never* been done before. This task is far from an easy one. Remaining stalwart in such a storm of uncertainty will test your mind, body, and spirit. However, you can make it through. Your lab mates are all pushing against the same wind and are willing to help you. Reach out for help when you need it, and take everything slowly. We all overestimate what we can accomplish in six months, but we also always under estimate how much we can accomplish in six years.

1.3 Overview

A continued source of improvement for the quality of graphene based 2DEGs, and the emergence of increasingly delicate correlated states of electronic matter in these systems, has been the removal of charged impurities near the sample layer. The first major breakthrough - in 2011 - which substantially improved sample quality without adding a significant increase in fabrication complexity, came from using an additional 2D material, hexagonal Boron-Nitride (hBN), as a substrate and encapsulant [1]. Before this, typically, devices were made by patterning metal contacts directly onto graphene exfoliated onto SiO2 where the bulk conducting Si acted as a global back gate [2]. However, the large number of charge impurities found in the thermally grown oxide along with disorder introduced via standard nano-fabrication processes limited 2DEG mobility. The introduction of hBN as a substrate and the creation of the first "van der Waals heterostructure," started a research revolution for graphene, which directly lead to the observation of the fractional quantum Hall effect in graphene, the demonstration of Hofstader butterfly physics in hBN-graphene Moiré superlattices, and even superconductivity in twisted graphene multi-layers [3, 4, 5, 6, 7, 8, 9].

It took an additional six years before another leap forward was taken - in 2017 - by Zibrov et. al with the introduction of graphite gates [10]. Previously, the charge carrier density in graphene based devices encapsulated by hBN was modulated via amorphous metal gates fabricated using standard lithography and metal evaporation processes. Both the grain structure of evaporated metal as well as the charge traps formed via oxidation of the sticking layer (typically Chrome or Titanium) induced microscopic disorder into the heterostructure obscuring, for example, fractional quantum Hall physics below 20T [10, 5]. Graphite, in stark contrast to evaporated metal, is an atomically flat and uniform crystal (made of several van der Waals bonded sheets of graphene) which behaves like a

semi-metal, even at temperatures below 1K, for sufficiently high layer-index. Much like hBN, graphite can be integrated into a van der Waals heterostructure and the relatively large density of states allows for significant screening of charge impurities from both the underlying SiO2 and from polymer residue on top of the heterostructure.

Using graphite for the gate layers introduced the concept of an “all van der Waals” device; an entire mesoscopic structure where every part is composed of a 2D material. On top of the fact that van der Waals materials appear to be self-cleaning, permanently expelling hydrocarbon contaminants between layers which naturally accumulate due to typical 2D material preparation via mechanical exfoliation [2]. Such atomically uniform dielectric environments for graphene based 2DEGs directly enabled the observation of even-denominator fractional quantum Hall states in bilayer graphene [10]. These states of matter are predicted to host non-abelian anyons which may form the basis for intrinsically fault-tolerant quantum computation and have attracted nearly three decades of intense theoretical and experimental interest[11, 12]. While these states are exceptionally delicate in competing platforms such as GaAs/AlGaAs quantum wells, the energy gaps for the even-denominator states in bilayer graphene all van der Waals heterostructures have been measured to be an order of magnitude larger: nearly 5K in recent experiments [13].

Moreover, the introduction of graphite gates helped elucidate more subtle fractional quantum Hall physics and the effects of quantum Hall ferromagnetism. Demonstration of the multi-component nature of FQH states in bilayer graphene were performed by studying the electric field induced transitions between isospin flavors of different FQH states [10]. Such experiments were even extended to monolayer graphene in 2018 where a multi-component incompressible state was discovered at $\nu = -1/2$ at the degeneracy point between two isospin orientations at high magnetic fields [14].

While a myriad of other works came forward in the years that followed which highlighted the exceptionally high bulk device qualities achieved by dual-graphite gated, hBN

encapsulated, van der Waals heterostructures [15, 14, 16, 17, 18, 19, 20] there remained a fundamental problem. Further study of the delicate correlated electronic states of matter in these devices, in particular the numerous fractional quantum Hall states observed in bilayer graphene, requires in situ manipulation of the underlying quasiparticle excitations or chiral edge modes. Other than a select few carefully implemented thermodynamic measurements, such as measurements of the underlying chemical potential and entropy of these states [13, 21], performing such experiments requires complex gate geometries used to spatially modulate the electronic density in different regions through out the device. These types of devices include quantum point contacts used to bring the chiral edge modes of the quantum Hall effect within a single magnetic length to study their tunneling properties, Fabry-Pérot interferometers which can be used to probe the statistics of many bulk qusiparticles, and quantum dots which can trap single quasiparticles and manipulate them.

Creating the complex gate structures required of these mesoscopic devices is fundamentally in tension with the program of the "graphene revolution." Either the all van der Waals geometry needs to be abandoned and some gates patterned using evaporated metal, or the top graphite gate can be removed post assembly of the heterostructure. Pioneering work done by Zimmerman et al in 2017 made the first successful QPC in a graphene van der Waals heterostructure using evaporated metal split gates [22]. Despite successfully partitioning integer quantum Hall edge modes at high magnetic fields, clear partitioning of fractional quantum Hall edge modes remained ambiguous. In 2021, Deprez et al, using a similar methodology to Zimmerman, managed to fabricated two QPCs in series to form a Fabry-Pérot interferometer [23]. Again, while coherent oscillations were seen for integer quantum Hall states, no such observations were made for the more delicate fractional quantum Hall states.

In 2021 Ronen et. al demonstrated the first successful operation of a Fabry-Pérot

interferometer in an entirely van der Waals geometry [24]. Here the gates defining the interferometer were fabricated by manufacturing a van der Waals heterostructure with an exposed graphite top gate. The top gate was then selectively etched into the interferometer pattern along narrow trenches using standard reactive ion etching and nanolithography techniques. The etch was thoroughly controlled in order to minimally damage the exposed underlying dielectric in critical regions between separated gates. Remarkably in this all van der Waals construction, despite having well formed fractional quantum Hall states in the bulk at 8T no interference fringes were observed for any fractional edge modes. The stark absence of any successful attempt to manipulate the edge modes of even the most robust fractional quantum Hall states makes it clear that disorder in regions between gates at critical junctures, for example within QPCs or along interferometer arms, is unavoidable using standard nanofabrication techniques.

It is here where the work presented in this thesis falls. In order to solve this problem, we introduced a new methodology for fabricating mesoscopic devices in an all van der Waals geometry. The basic premise is to pre-pattern a graphite flake in an entirely resist-free process and then integrate it directly into the heterostructure using a low-strain variant of the canonical dry-transfer technique. To pre-pattern the graphite flake we use electrode free, AFM based, local anodic oxidation gate lithography (AFM-AOGL). The essence of this technique is that a conductive AFM tip is brought into close proximity to an exfoliated grpahite flake and due to capillary action a water meniscus forms between the tip and the flake. By applying an AC voltage to the AFM tip we are able to catalyze an electrochemical reaction which converts water and graphite into amorphous carbon and gaseous byproducts enabling nanoscale subtractive lithography [25, 26, 27, 28]. Then using a low-strain variant of the standard dry-transfer technique for assembling van der Waals heterostructures, we can directly integrate patterned microstructures into a stack. This simple concept has enabled a whole new class of experiments that were not

previously thought possible in graphene; these include demonstration of universal chiral Luttinger liquid physics, Andreev-like scattering of fractional quasiparticles, interference of fractional edge modes, and measurements of the statistical phase of anyons.

This is only the beginning. This small insight, which allowed us to fabricate mesoscopic devices without introducing any additional disorder into the heterostructure, although simple in construction, has changed the game for us. Often times the most pedestrian of ideas, such as putting graphene on hBN, using graphite as a gate, or prepatterning a graphite gate with no polymer steps, can have the biggest impacts on the types of devices we can make and the physics we can observe. My advisor, Andrea Young, wrote in his thesis over a decade ago that he learned "*experiments are only hard until they are easy*." We expect this result to generalize and will open up the pathway to a cornucopia of interesting experiments taking advantage of the many interesting states found in graphene based van der Waals heterostructures, such as superconducting junctions in rhombohedral graphite multilayers, quantum anomalous Hall superconductor interfaces, and non-abelian fractional quantum Hall interferometry.

2

AFM Based Local Anodic Oxidation Lithography of Graphite Gates

2.1 Overview

Mesoscopic devices operating in the fractional quantum Hall regime are generally more sensitive to disorder than devices operated within the integer quantum Hall effect. For example, at a quantum point contact, due to the chiral Luttinger liquid instability, an incoming FQH edge mode, at sufficiently low energies is guaranteed to scatter, even

for an arbitrarily small impurity potential [29, 30, 31, 32, 33]. While this type of effect has no consequence on bulk topological properties, such as the quantized conductance value of σ_{xy}, in situations where the electronic transport depends on the coherence of the edge wave function, such as inside of an edge state Fabry-Pérot cavity, it becomes highly important. Even fairly weak impurity potentials distributed along the boundary of an interferometer will act as which-path detectors and dephase the edge wave function, reducing the overall measurement signal. Equivalently, interaction with localized states induced by disorder at the edge amounts to a renormalization of the edge velocity, making it harder to maintain coherence over large distances leading to shorter coherence lengths in the fractional quantum Hall regime [34]. Besides the general fact that the ultimate technological goal is to operate the mesoscopic devices discussed in this thesis in the even-denominator fractional quantum Hall states, with potential applications towards error protected quantum information processing, even operation (or inability to operate) in the simplest Laughlin FQH states (for example at $\nu = 1/3$) will provide a good litmus test to judge the amount of disorder present in a particular device.

Taking a survey of the field in 2020, by the time this work started in earnest, there were a number of seminal results in graphene quantum Hall mesoscopics of particluar note. Before hBN became widely adopted as a clean substrate for graphene, S. Nakaharai et. al used electron-beam lithography – a standard tool in semiconductor processsing – to evaporate metal split gates, separated by 150nm, onto an exfoliated graphene flake with an ALD grown Al_2O_3 oxide on top [35]. While some dependence of the cross device conductance on the QPC split gates was observed, the bulk of the observed behavior was attributed to uncontrolled mixing of the edge modes in each region of the device due to disorder scattering. This limited any further investigations of quantum Hall edge modes in a graphene quantum point contact, for example via tunneling spectroscopy at the QPC, at least for this device architecture.

A substantial improvement on this device was made by K. Zimmermann, et al., in 2017. While using a similar paradigm to Nakaharai, instead of using an amorphously grown oxide as the dielectric, Zimmermann evaporated the metal split gates, which formed their QPC, directly on top of a fully hBN encapsulated graphene stack [22]; a schematic diagram and SEM image of Zimmermann's device is shown in Fig. 2.1[1]. Zimmermann was able to demonstrate clear partitioning of integer quantum Hall edge modes at sufficiently high magnetic fields, as well as elucidate a number of complex edge mode equillibration processes at the QPC which affect the net transmission across the device. Zimmermann's work represented an important step forward in graphene mesoscopics, however, while the data were beautiful, clean operation in the fractional quantum Hall regime remained elusive. In particular, work in Zimmermann's PhD thesis [36] shows attempted tunneling measurements at the QPC (aimed at extracting the Luttinger parameter, a key measurement which classifies the topological character of FQH edge modes), while the graphene bulk is set to fractional filling of the first Landau level. Their results, while showing suggestive non-linearity in the bias dependence of the tunneling current, did not agree with the predictions from the chiral Luttinger liquid theory and were complicated by the presence of disorder inside of the QPC, putting their work in line with previous results from GaAs quatum wells obtained nearly two decades prior [37, 38, 32, 39].

In a follow up work from the same group using an identical technique in 2021, C. Depréz was able to string two quantum point contacts together to form a quantum Hall Fabry-Pérot interferometer (FPI) [23]. A quantum Hall FPI is a device which uses two QPCs to form a resonant cavity through which quantum Hall edge states can traverse. The transmission through the cavity is tuned by the net Aharanov-Bohm phase picked up as the edge states travel around the cavity (See Chapter 4 for a more

[1]Images licensed under creative commons attribution 4.0

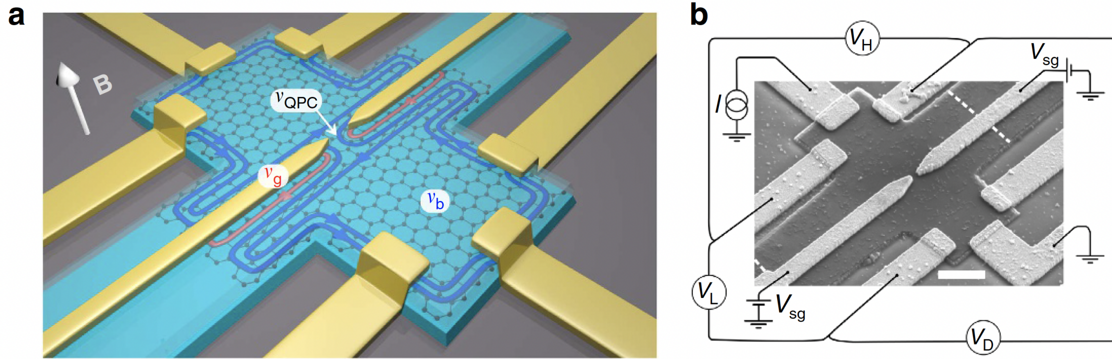

Figure 2.1: (a) Schematic cartoon of Zimmermann's graphene QPC architecture taken from *Tunable transmission of quantum Hall edge channels with full degeneracy lifting in split-gated graphene devices, Zimmermann et. al, Nature Communications* [22]. A number of $N_b \equiv \nu_b$ quantum Hall edge modes are brought into close proximity to each other by tuning ν_{qpc} with a voltage applied to V_g, the voltage on the metal split gates. (b) A scanning electron microsocpe (SEM) image of Zimmerman's device, also taken from [22] which shows the metal evaporated split gates fabricated on top of the van der Waals heterostructure.

detailed description of how quantum Hall Fabry-Pérot interferometers work). Moreover, in the fractional quantum Hall regime the Aharanov-bohm dominated interference fringes should be subject to sudden phase-slips as a result of the non-trivial braiding phase of quantum Hall anyons which are populated in the bulk of the interferometer, making this measurement highly desirable. However, despite fairly robust interference observed in Depréz' work in the integer quantum Hall regime, no such interference was observed while operating within the fractional quantum Hall effect.

After A. Zibrov et. al introduced the all van der Waals heterostructure in 2017 [10], replacing all gate layers with graphite, there became an obvious direction of improvement for how to make cleaner graphene mesoscopics that could improve upon Déprez' and Zimmermann's work. The first successful attempt at this came in 2021 by Y. Ronen et. al [24]. Ronen made a fully dual graphite gated, hBN encapsulated, monolayer graphene Fabry-Pérot interferometer (FPI); see Fig. 2.2 for an SEM image of their device. Ronen

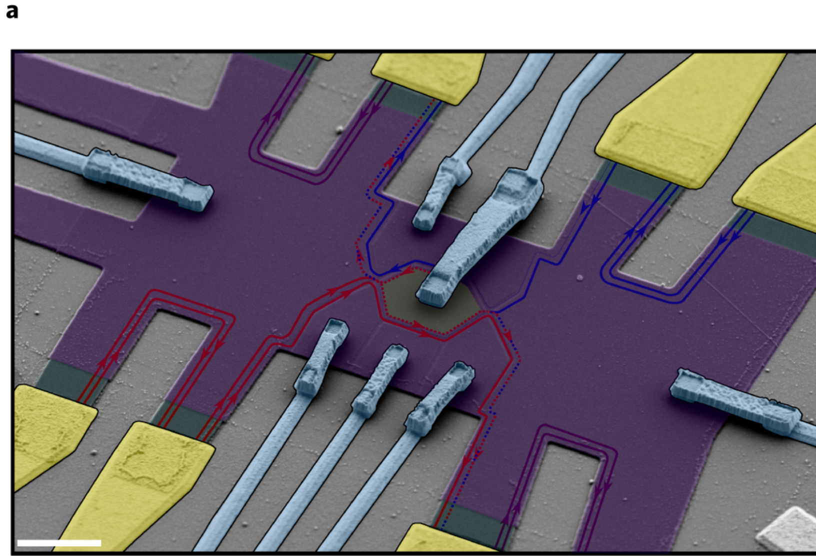

Figure 2.2: (a) False color SEM image of Ronen et. al's device architecture. The quantum Hall edge state paths are drawn in red and blue respectively. Additionally, the different gate regions are highlighted where metallic air bridges can be seen making contact to the exposed graphite layer. The small trenches etched out between neighboring gate regions can also be seen.

used electron beam lithography with a PMMA mask and incremental amounts of reactive ion etching to create 50nm trenches which separated the top-graphite layer of his van der Waals heterostructure into seven separate gates used to form the interferometer. To minimize the damage done to the hBN dielectric in the critical region between adjacent gates, Ronen pre-fabricated electrical contacts to the desired gate regions (using edge contacts following the recipe in [40]), and performed the etching step in thirty second increments until neighboring gates, which originally were one contiguous piece of graphite, were no longer in electrical contact.

With this improvement, Ronen managed to demonstrate robust quantum interference in the integer quantum Hall regime at a substantially lower field of 8T in comparison to Déprez' work which was performed at 14T. However, despite the remarkable amount of care which went into minimizing the etch induced damage accumulated by the critical

junctions between neighboring gates (ultimately where the edge state path runs along), no interference in the fractional quantum Hall regime was observed. This is also despite having well formed fractional quantum Hall states in the bulk of the device, as detected by edge state transport, in contrast to Zimmerman and Déprez' work where the bulk fractions were not fully developed even at 14T due to the lack of graphite bottom gates in their devices. Despite substantial effort to minimize charge impurities along the edge channels (resulting from dielectric damage from the graphite etching process) in Ronen et. al's interferometers, the lack of any interference signature in the fractional quantum Hall regime suggests an entirely new fabrication paradigm is required [2].

Given that FQH edge interference is sensitive even to minute amounts of disorder introduced during a weak etching step, it stands to reason that a good remedy to this would be to pre-pattern the required graphite flake before incorporating it into a van der Waals heterostructure, thus preventing any damage to the dielectric directly above the active layer of the heterostructure. This captures the spirit of the technique described in this section in principle, however, if one uses standard EBL and RIE techniques to pre-define the patterns in graphite, this results in a significantly reduced bulk device quality. Fig. 2.3 highlights the fabrication process used to construct a dual graphite gated, hBN encapsulated, monolayer graphene corbino geometry transport device using EBL and RIE to pre-pattern the top graphite layer. This type of device is used to probe transport across the bulk in the monolayer; in the quantum Hall regime, when the device is electrostatically doped to an integer or fractional quantum Hall state, if the bulk is sufficiently insulating, the conductance between neighboring contacts should drop to zero. Devices of this type, fabricated without any pre-patterning of the top graphite

[2]At the time of writing this thesis, new work from Ronen's group, now at the Weitzmann institute, used a similar technique as discussed in [24] to fabricate a bilayer graphene Fabry-Pérot interferometer. With some improvement in their fabrication techniques, they were able to observe Aharanov-Bohm oscillations in a limited regime at $\nu = 1/3$ at 12T [41]

layer, have been used in several studies attempting to interrogate delicate gapped states at high magnetic field, and have consistently demonstrated the high quality bulk of dual graphite gated, hBN encapsulated, graphene devices [17, 18].

Remarkably, when the top layer is pre-patterned - done in principle to eliminate an extra stack-flipping step required for the corbino-style contact - the resulting device does not show any well developed insulating states at fractional fillings at high magnetic fields. This is shown in Fig. 2.3c. The absence of insulating states at fractional filling is held in stark contrast to other devices made without pre-patterning of the top-graphite layer, see Fig. 2.3d, which shows many well developed fractional quantum Hall states at similar magnetic field strengths. In the highest quality devices, deep insulating regions at the most robust fractional fillings $\nu = 1/3$ and $\nu = 2/3$ can be observed at as low of a field as 3T [18]. It is somewhat unexpected that this methodology would so severely increase the disorder in the bulk; in principle only the top part of the graphite was processed, so any remaining residue should remain on top and be screened by the graphite, protecting the monolayer. Unfortunately, it is hard to pin down an exact mechanism for what causes the bulk degradation. However, it is likely that after removing a polymer based resist, such as PMMA, used during an EBL step, the solvent saturated with polymer creeps under the flake and either damages the under layer, or so severely contaminates it that the disorder cannot be removed by further device processing.

Ultimately, the technique that we came up with that helps circumvent these issues is to use AFM based local anodic oxidation to perform nanoscale subtractive lithography on graphite flakes. This can be done in an entirely solvent-free and resist-free process, on as-exfoliated graphite, with minimal setup. The microstructured flakes can then be directly integrated into a van der Waals heterostructure, where additional carbon based contaminants resulting from the initial anodic oxidation process are removed post-transfer. This process results in ultra-pristine pre-patterned gate structures which

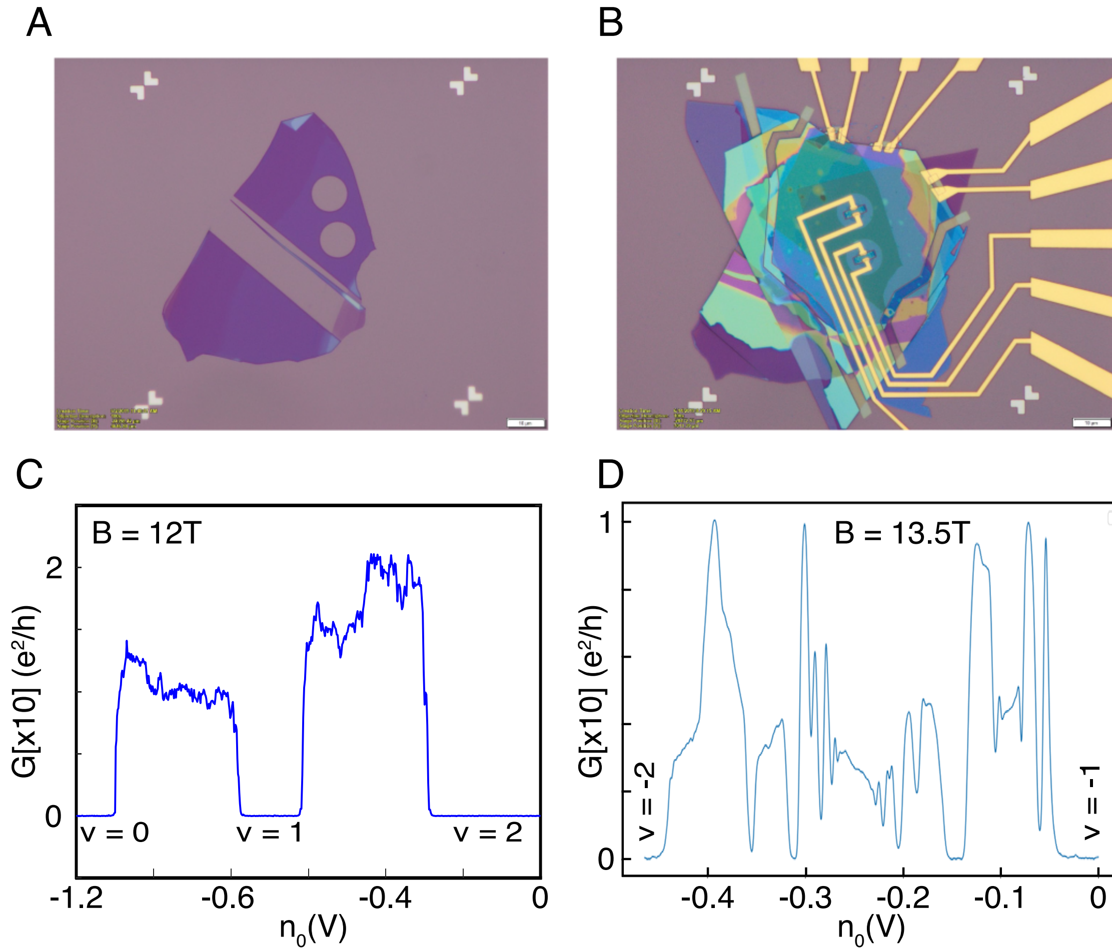

Figure 2.3: **Comparison of bulk transport in corbino-style quantum Hall devices with pre-patterned graphite gates using EBL/RIE versus standard processing.** **(a)** Optical micrograph of a pre-patterned graphite flake used to form the top gate of a corbino-style dual-graphite gated, hBN encapsulated, monolayer graphene quantum Hall transport device. **(b)** Optical micrograph of completed device with the pre-patterned gate in panel (a) transferred into the stack using van der Waals dry-transfer. Notably, the region between the two islands appears optically clean and bubble-free. **(c)** Two terminal, inter-island, conductance versus electronic density in the monolayer for the device in panel (b). Clear insulating states with zero conductance are observed for the bulk integer fillings between $\nu = 0$ and $\nu = 2$ at B = 12T, and T = 20mK, however, no developed fractional quantum Hall states are observed. **(d)** Two-terminal, inter-island, conductance versus electronic density in the monolayer for a separate device fabricated without pre-patterning the graphite-top gate. Here, clear insulating states are developed for many fractional filling factors between $\nu = -1$ and $\nu = -2$ at B = 13.5T and T = 20mK. This is in stark contrast to the number of insulating states observed between two Landau levels in panel (c).

can be used to form a variety of mesoscopic devices ranging from quantum point contacts to Fabry-Pérot interferometers, quantum dots, and others. While this chapter will not focus on the results acquired by utilizing this fabrication technique (our results on QPCs and FPIs in the FQH regime will be discussed at length in chapters 3 and 4), the remainder of this chapter will detail the capabilities of local AFM based anodic oxidation gate lithography (LAFM-AOGL) as well as describe the physical mechanism behind the technique. Additionally, some outlook towards improving the reliability and critical features size of the technique will be discussed.

2.2 Atomic Force Microscope Actuated Local Anodic Oxidation Lithography of Graphite (LAFM-AOGL)

The operating principle behind LAFM-AOGL is straightforward. A conducting AFM tip is brought into proximity of an as-exfoliated graphite flake. Due to capillary action, in a humid environment, a water meniscus naturally forms between the graphite flake and the AFM tip, see Fig. 2.4a. A voltage is then applied to the AFM tip relative to the sample which makes an electrochemical reaction energetically favorable that converts the graphite into carbon di(mon)oxide and amorphous byproducts [25]. The reaction can occur as follows:

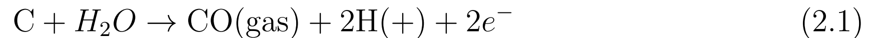

$$\mathrm{C} + H_2O \rightarrow \mathrm{CO(gas)} + \mathrm{2H(+)} + 2e^- \tag{2.1}$$

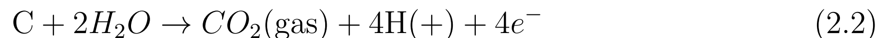

$$\mathrm{C} + 2H_2O \rightarrow CO_2\mathrm{(gas)} + \mathrm{4H(+)} + 4e^- \tag{2.2}$$

By then controlling the speed and direction of the AFM tip while the voltage is being applied, one can perform nanoscale subtractive lithography on graphite. A schematic illustration of this process is highlighted, again, in Fig. 2.4a.

AFM based local anodic oxidation itself, not strictly on graphite, actually has a fairly long history. AFM based local anodic oxidation of some form has been used since the mid 1990s to fabricate metal-oxide junctions, aluminum quantum dot arrays, and metallic nanowires [42, 43, 44, 45]. Even as far back as 1991, Dagata et al. managed to oxidize the surface of a III-V semiconductor using an STM tip in a humid atmosphere [46]. After 2004 when graphene was first isolated, these techniques were extended to exfoliated graphite fairly quickly [47, 48, 49, 50, 51, 52]. However, the common thread between all of these previous results is that they all required attaching an electrode to the target surface. Depositing an electrode typically involves some type of EBL process, which naturally requires a polymer resist and dissolution step that leaves a substantial amount of residue. Consequently, at first pass, this technique would not be able to solve the issues put forth in the beginning of this chapter where the application of a polymer resist and its subsequent removal on a single graphite layer embedded into a van der Waals heterostructure adds unscreened charge disorder. Additionally, early devices fabricated in this manner, such as QPCs formed by etching the active graphene layer itself into a narrow trench at a point [53], never displayed particularly clean electronic transport. So it took another six years before this technique found a more useful application in graphene mesoscopics.

In 2018 Li et. al worked out that few-layer graphene can be anodically oxidized using an AC voltage applied to the AFM tip, as opposed to a DC voltage [25]. The advantage of this technique is that because the graphite is exfoliated onto a conducting Si wafer, which has a 285nm thermally grown oxide on its surface, the capacitive coupling between the graphite and the conducting Si lets a displacement current flow from the AFM tip

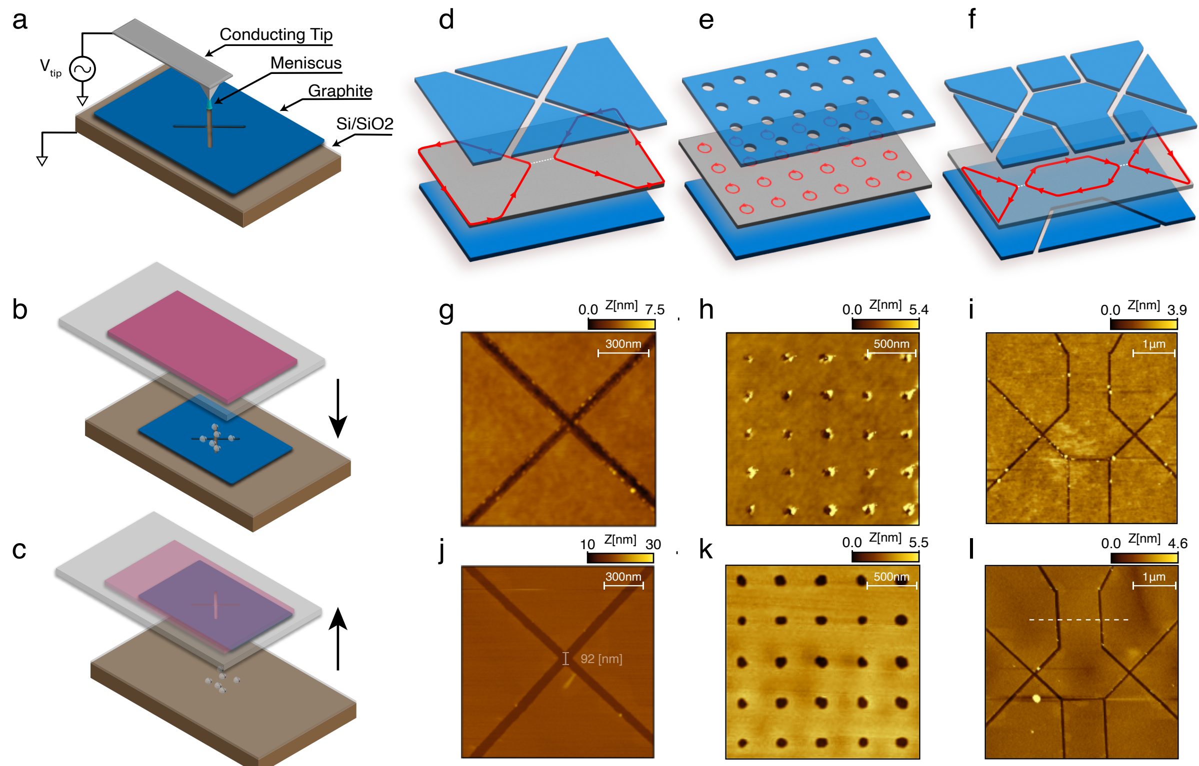

Figure 2.4: **Local anodic oxidation and integration of graphite gates into van der Waals heterostructures.** **(a)** A schematic example of an exfoliated graphite flake etched using atomic force microscope-actuated local anodic oxidation (AFM-LAO). Here we show the x-shaped geometry used to form the quantum point contact gates which constitute the device studied in this work. **(b)** A transfer stamp with an already picked-up hBN flake is engaged with the etched graphite flake which has some residual oxide residue from the AFM-LAO process. **(c)** Once the etched graphite is laminated onto to the hBN flake the structure can be disengaged, leaving behind the oxidized residue and resulting in a pristine microstructure. **(d)** Example edge state configuration of a quantum point contact resulting from the electrostatic potential created by an x-shaped graphite gate. **(e)** Same as panel (d) but with an array of holes in the top graphite gate used to create a superlattice of quantum dots. **(f)** Same as panels (d-e) but with an edge-state interferometer structure. Here the isolated Fabry-Pérot cavity can be realized by careful alignment of etched graphite gates in both the top and bottom layers of the heterostructure. **(g-i)** AFM topography images of patterns etched into graphite flakes using AFM-LAO corresponding to the top gate structures in panels (d-f). **(j-l)** AFM topography images of etched graphite on hBN post van der Waals pick-up of the flakes in panels (g-i) demonstrating that most of the oxidized residue (white dots) seen in panel (g-i) is not transferred.

to ground at sufficiently high frequencies ($\approx>$ 10kHz). Moving away from DC anodic oxidation obviated the need for pre-patterned electrodes and made it possible to perform nanoscale subtractive lithography without any resist removal steps, making it an ideal candidate to solve the issues liming Zimmermann's, Déprez', and Ronen's results.

During the beginning of my PhD, we spent some effort trying to improve the overall resolution and reliability of AFM based local anodic oxidation of graphite. By moving to PtIr coated AFM tips with a relatively large spring constant, 42N/m, we were able to produce sub-60nm feature sizes repeatably. Additionally, controlling the humidity inside of the AFM to above 50%RH was also critical for improving reliability (see Appendix D for a detailed fab recipe for AFM based local anodic oxidation lithography). However, what we noticed, is that even under optimal conditions, the graphite always showed some amount of residue in the trenches along the cut direction. This residue, likely amorphous carbon or carbon oxide, will result in charge disorder however it ends up integrated into the heterostructure (either as the active layer itself, or as a gate electrode). However, by somewhat of a miracle of science, when a nano-textured graphite flake with some anodic oxidation induced residue is picked up by an hBN using a variation of the standard dry-transfer process [54, 55, 3, 7], the residue selectively adheres more strongly to the SiO2 than the graphite. This results in a transferred pre-patterned graphite flake on hBN free from nearly all oxide residue [26]. This process is highlighted schematically in Fig. 2.4a-c.

Additionally, we have found that AFM cut graphite is extremely robust to the van der Waals transfer process; this is somewhat surprising as the dry-transfer process is fairly aggressive and the heterostructure undergoes a large amount of strain during transfer (see Appendix D for details). The only real requirement to ensure a successful transfer is that the cuts must be patterned into the graphite such that the flake remains simply connected. Doing this we have found that even sub-100nm nano-ribbons can be transferred inside the heterostructure with no damage.

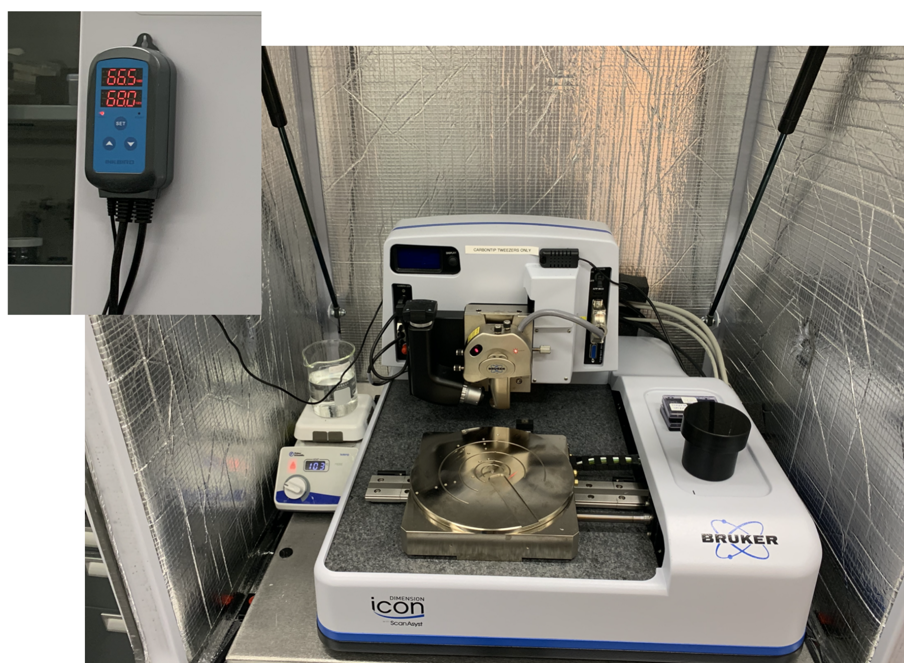

Figure 2.5: **Anodic oxidation lithography setup:** Our bruker dimension Icon AFM is equipped with a hot-plate set to 100C and a beaker filled with 300mL of DI water. The hot plate power is controlled by a humidity sensor which acts as a bang-bang controller that shuts off the power to the hot plate when a certain humidity threshold is exceeded. The humidity controller is showed in the figure inset.

This technique is highly versatile and can be used to form the gate layers for a number of different mesoscopic strucutres, each of which serves a unique device functionality. Three examples, all designed to operate in the quantum Hall regime, that we have fabricated are given in Fig. 2.4d-l. Fig. 2.4d shows an x-shaped cut-graphite which can be used to form four distinct gates that make a quantum point contact. This geometry will be discussed at length in Chapter 3. Fig. 2.4e shows an array of holes patterned into the top gate which can be used to form a quantum dot array. Finally, Fig 2.4f shows a quantum Hall edge state Fabry-Pérot interferometer. Interestingly, in this geometry by aligning AFM cut gates in two separate layers of the heterostructure, even isolated regions of local density may be individually controlled. Although this specific geometry will not be discussed in chapter 4 when I talk about Fabry-Pérot interferometry, we did fabricate a device of this type and it interfered successfully in the integer quantum Hall regime. For each of the device geometries shown in Fig. 2.4d-f, we have the corresponding AFM topographs immediately after AFM cutting (pre-transfer), see Fig. 2.4g-i, and after pick-up with an hBN crystal (imaged on the transfer slide), see Fig. 2.4j-l. A substantial amount of graphite-oxide or amorphous carbon residue can be seen in the AFM topographs of Fig. 2.4g-i, indicated by the white dots in the images. However, after the van der Waals transfer process, this residue is mostly eliminated demonstrating the pristine topographical quality of the transferred nano-structured gates (the most stark example of this is the comparison for the hole array in Fig. 2.4h and k).

Not only is this method of patterning sub 100nm nanostructures into graphite gates and integrating them into a van der Waals heterostructure versatile, but it is also very accessible to any researcher in this field. Along the spirit of van der Waals device fab in general, doing such fine, ultra-clean, lithography does not require any specialized tools but can be made to work in nearly any AFM (as local anodic oxidation itself is fairly well established platform for nanoscale lithography, most relatively modern AFMs are

equipped with some way to controllably move the AFM tip around). Fig. 2.5 shows the setup we have in our own lab, where our Bruker Dimension Icon AFM (which sits inside of a vibration isolation hood) is fashioned with a humidity sensor which simply turns off the hot-plate (using bang-bang control) with the beaker filled with 300mL of water on top of it once the humidity exceeds a certain threshold. With being so easy to implement, we expect that this technique will be widely adopted in the future for a myriad of possible experiments both in the quantum Hall regime and at zero magnetic field.

2.3 Multi-layer Alignment via "Slip-n'-Slide" of AFM Cut Gates

It was briefly mentioned in the previous section, but an important limitation of LAFM-AOGL is that in order for patterned graphite flakes to remain structurally integral during the van der Waals transfer process, the cuts must be made such that the patterned graphite is still one contiguous piece. Once the cut-graphite is put into the heterostructure, neighboring gate regions can be separated in the non-critical part of the device using standard a standard RIE process (this is discussed further in chapters 3, 4 and Appendix C). The primary reason for this that the friction between hBN and graphite is nearly zero, and as a result of the macroscopic strain a heterostructure undergoes during assembly, free standing layers of graphite easily move and rotate and typically wind up shorting to another adjacent gate layer [56]. While this is not exceptionally limiting, however, it does prevent for example an isolated graphite island from being transferred. This makes it challenging to replicate the exact experiments performed Ronen et. al or more recently Werkmeister et. al, as they are able to create an isolated center gate to control the density within their interferometer bulk [24, 57].

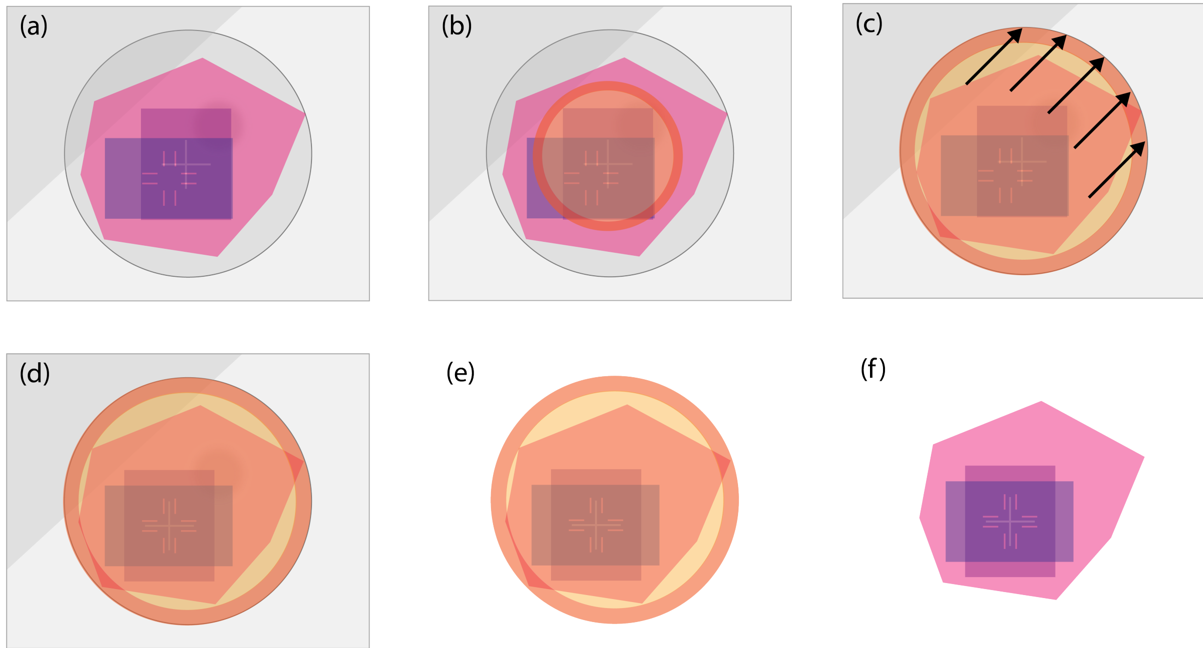

Figure 2.6: **Illustration of slip-n-slide technique** (a) An assembled heterostructure on a transfer slide with a sacrificial PC film (see appendix) containing two patterned graphite layers that are misaligned, separated by an hBN crystal between them. The cross in the bottom layer is designed to be aligned to the anti-cross in the first layer. (b) The stack on the PC film is engaged onto the substrate. (c) Once the stack and the film are fully engaged onto the substrate at 160C micro-manipulators can be used to push the heterostructure along the direction the top layer needs to move to re-align the two graphite layers. (d) Once alignment is achieved the micro-manipulators stop pushing the stack. (e) The sacrificial PC film is heated to above 180C (the glass transition temperature) and the stack can be deposited onto the target substrate. (f) The sacrificial PC film can be dissolved in chloroform, leaving an aligned heterostructure. This process can actually be repeated in the event of a failed attempt simply by re-engaging the transfer slide with a new PC film onto the deposited stack and then starting from panel b.

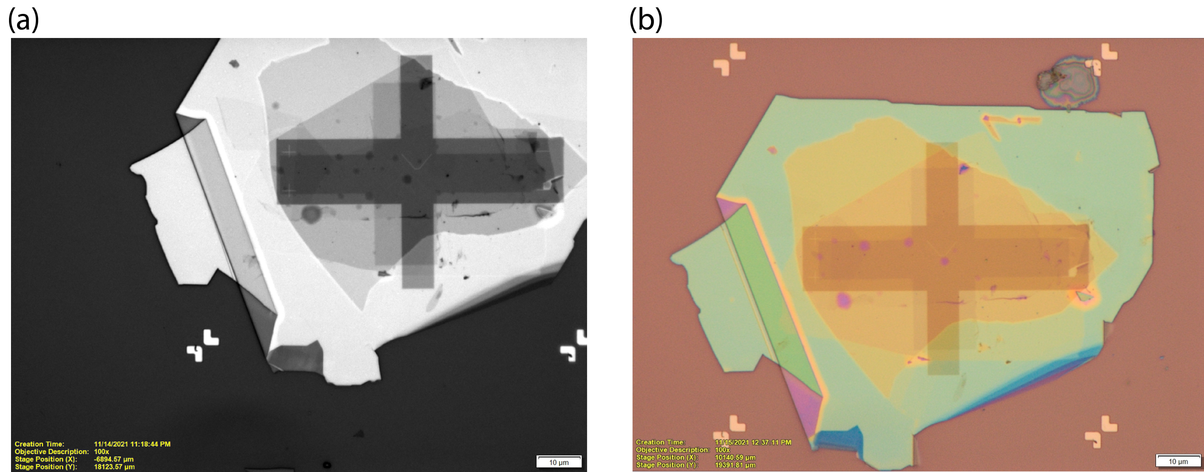

Figure 2.7: **Example of stack aligned using slip-n-slide** (a) A van der Waals heterostruture with two AFM cut gates that are misaligned. The corners of the bottom later should meet the centers of the crosses AFM patterned into the top layer. (b) Device after re-aligning the two grapite layers. The corners of the bottom graphite gate are nearly aligned with the center of the crosses patterned into the top graphite layer.

We were able to get around this limitation by using a technique that we've dubbed "slip-n-slide." By turning the super-lubricity of graphite on hBN from a disadvantage to an advantage, we realized that because the bottom graphite layer has a higher degree of friction between itself and the SiO2 than to the hBN layer directly above it, we are able to re-align the rest of the stack to the bottom layer after it has already been deposited onto the SiO2 substrate. A schematic illustration of this is given in Fig. 2.6a-f. This capability opened up the possibility of aligning AFM cut gates in two separate layers. This made the geometry proposed in Fig. 2.4f feasible from a fabrication perspective, and allows us to make devices where we may control an isolated island of density in the active device region. An example of this technique used to align two graphite layers with AFM cuts embedded in a heterostructure within less than 1um is shown in Fig. 2.7a-b.

2.4 Outlook and Pathways to Improvement in Consistency

While local anodic oxidation lithography of graphite gates has proved to be a versatile tool enabling the fabrication of a variety of different mesoscopic devices, it certainly comes with its own set of limitations that we have not yet overcome. The first challenge is one of feature size; the current state of the art for us is that with some effort we can semi-reliably pattern 50nm trenches into a few-layer graphite flake. Achieving smaller lithographic features is desirable as it directly translates into devices that can be made with sharper electrostatics, leading to more strongly confined quantum dots and higher edge velocities in edge-state Fabry-Pérot interferometers.

The primary mechanism which controls the minimum feature width AFM-cutting can achieve is the size of the water meniscus which forms beneath the AFM tip and the substrate. This effect has been studied extensively, and is captured by a phenomenological equation called the Kelvin equation [58]:

$$r_k = \frac{\gamma_L V}{RT\log(p/p_0)} \tag{2.3}$$

Here, r_k is called the Kelvin radius - the harmonic mean of the principle radii of the mensicus (see [58]) - γ_L is surface tension of the liquid forming the mensicus, V is the molar volume of the liquid (measured in m^3/mole in SI units), R is the ideal gas constant, T is the temperature, and p/p_0 is the relative vapor pressure of the liquid. A smaller r_k will directly translate into smaller meniscus sizes, and consequently smaller feature sizes during LAFM-AOGL. Naturally, it would be logical to perform the anodic oxidation lithography in a controlled environment cell, such as is available on many of the more modern Asylum instruments AFMs, such as the Cypher ES. This would enable precise

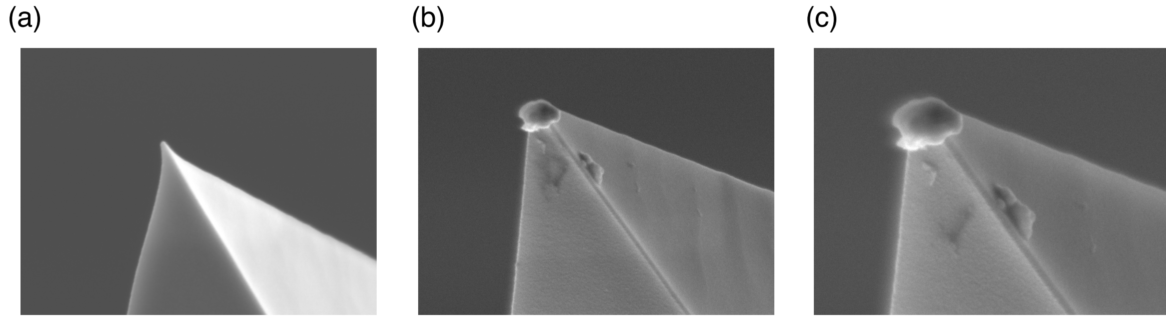

Figure 2.8: **Arrow NcPt tips after cutting** (a) SEM image of an unused AFM tip showing no degradation. (b) SEM image of a used Arrow NcPt AFM tip after the tip was no longer able to cut graphite. (c) SEM image of the same tip in panel b, but after 60 seconds of 100W O2 plasma ashing at 300mTorr.

control of γ_L, V, T, and p/p_0 more easily. The most accessible variable will be temperature, as increasing the temperature will directly decrease r_k. Additionally, increasing the temperature will lower the surface tension and increase the partial pressure, also serving to indirectly lower r_k as well. One may also imagine, in a sealed AFM environment cell, using a mixture of solvent and DI water to help decrease γ_L; for example mixing DI water with IPA in small concentrations can significantly lower the surface tension of the mixture.

Other features which may serve to improve the minimum feature size achievable with LAFM-AOGL are the tip geometry as well as the coating material. The current tips that we use, the NcPt Arrow PtIr coated tips, already have a fairly small radius of < 25nm shown in Fig. 2.8a, however it is possible that moving to a smaller tip radius will result in a smaller cut width. The coating material may also matter both because of how hydrophilic the surface is, as well as how conductive the coating is. A highly conductive surface is important for not dropping any voltage across the AFM tip itself, so all of the voltage goes into enabling the oxidation reaction. Furthermore, if the surface

is hydrophobic the tip will tend to not form a meniscus. We have made several attempts to pattern graphite flakes with doped-diamond probes, but have had no success in getting complete ablation of the graphite to occur; it is likely that the doped diamond probes do not work as well as the metal coated probes for the two reasons stated above.

Beyond getting smaller feature sizes reliability is also an issue. LAFM-AOGL is fundamentally a contact mode technique, i.e, the AFM tip is in contact with the surface as the lithography is performed. For soft-metal coated tips this results in fairly rapid degradation of the probe. In Fig. 2.8a which shows a fresh PtIr coated AFM tip before LAFM-AOGL a sharp sub 25nm tip radius may be observed. However, after the lithography step, Fig. 2.8b shows a smashed tip radius well over 100nm in diameter. Fig. 2.8c shows the same tip after exposure to O2 plasma showing that the tip itself has been damaged and it is not amorphous carbon or carbon oxide residue that has attached itself to the tip. Possibly using PtSi tips, which boast much higher conductivities than doped-diamond tips, but are considerably more robust to contact mode degradation than the PtIr tips may improve the tip wear issue.

While it is true that this technology is not at the point where large scale patterns may be etched in a controlled manner, similar to the extremely well developed techniques of photolithography or electron-beam lithography, LAFM-AOGL is extremely nascent. It is hard to say what the ultimate resolution or reliability limit of this technique is; there does not appear to be any fundamental limitations that would inherently inhibit the scalability of this technique. I believe that with sufficient development, over time this technology could produce ultra-clean van der Waals devices with the same level of complexity as modern-day monolithic integrated circuits.

2.5 Permissions and Attributions

1. Some of the content of this chapter also appears in Ref.[26]
2. SEM images from Fig. 2.8 were taken by Noah Samuelson, reproduced here with his permsission.
3. Image in Fig. 2.1 is used under Creative Commons License 4.0 and is reproduced here purely for academic purposes from Ref. [22].
4. Image in Fig. 2.2 taken from Ref. [24] is used under license number 5731050269832.

3

Quantum Point Contacts in Graphene van der Waals Heterostructures

3.1 Overview

In an all-van der Waals heterostructure, the active layer, gate dielectrics, and gate electrodes are all assembled from two-dimensional crystals that have very few defects. This design allows two-dimensional electron systems with very low disorder to be created, particularly in heterostructures where the active layer also intrinsically has low disorder,

such as crystalline graphene layers or metal dichalcogenide heterobilayers. A key missing ingredient has been nanoscale electrostatic control, with existing methods for fabricated local gates typically introducing unwanted contamination. In the previous chapter, we discussed a resist-free local anodic oxidation process for patterning sub-100 nm features in graphite gates, and their subsequent integration into an all-van der Waals heterostructure. To benchmark this technique electronically we first defined a quantum point contact in the fractional quantum Hall regime and observed signatures of chiral Luttinger liquid behavior, indicating an absence of extrinsic scattering centers in the vicinity of the point contact. In the integer quantum Hall regime we demonstrate *in situ* control of the edge confinement potential, a key requirement for precision control of chiral edge states.

Utilizing this *in-situ* control of the potential sharpness, we then go on to demonstrate an ultra-clean heterojunction between $\nu = 1/3$ and $\nu = 1$ quantum Hall states. In the low-energy limit we will show the universal scaling laws predicted for a quantized chiral Luttinger liquid at $\nu = 1/3$ in the sharp-edge limit. In the high energy limit we will also demonstrate the existence of a hidden quantum number conservation rule which leads to Andreev-like scattering of fractionalized e/3 quasiparticles. Moreover, we can actually compare the entire cross-over between the weak-coupling and strong coupling limits of the heterojunction and see that it very nearly matches an exactly solveable quantum impurity model.

3.2 Introduction

Van der Waals heterostructures have recently emerged as a rich platform to study the physics of delicate correlated electronic states, including (but not limited to) fractional quantum Hall phases[10, 59, 17], exciton condensates[17, 60, 61], quantized anomalous Hall insulators[16, 62], fractional Chern insulators[63, 64], and superconductors[6, 65, 20,

66, 67]. A key driver of continued improvement in sample quality has been the removal of charged impurities, first with the use of high purity two-dimensional crystals of hexagonal boron nitride (hBN) as a substrate[1] and gate dielectric[8, 68, 40], and more recently with the use of graphite, rather than amorphous metal, for the gate layers[10]. These 'all-van der Waals heterostructures' take advantage of the fact that none of the components in the stack host dangling bonds in their two-dimensional bulk. In addition, numerous van der Waals interfaces appear to be self-cleaning[69], irreversibly expelling hydrocarbon residues during processing and leaving an atomically uniform interface.

A central feature of these platforms is electrostatic tunability, enabling a variety of correlation-driven ground states to be accessed by field effect gating in a single device. Electrostatic control on the nanoscale, then, allows one- and zero-dimensional structures to be created within a correlated two-dimensional state, opening the door to experiments that probe the structure of interfaces between distinct phases as well as adiabatic manipulation of individual quasi-particles and edge modes. A wide class of these experiments require electrostatic confinement on length scales comparable to the correlation length of superconductors or fractional quantum Hall states, which is typically below 100 nm. The confining potentials are also required to be energetically uniform, in the sense that they should not introduce uncontrolled local electrical potentials larger than the $\approx 1\,\text{meV}$ energy gaps of the correlated states to be studied. There are two options empowered by traditional electron beam lithography, which is capable of patterning at the length scales required for constructing such nano-scale potentials. First, the all-van der Waals geometry may be abandoned, patterning at least some gates from evaporated metal. Second, heterostructures may be assembled and then graphite gates patterned by subtractive processes. However, both techniques lead to disorder in critical regions of the device. For example, edge state interferometers manufactured using either technique remain limited to the integer quantum Hall regime despite the presence of well formed

fractional quantum Hall phases in the two-dimensional sample bulk [24, 22, 23, ?].

3.3 Fabrication

Here we show how high-quality mesoscopic devices may be created by abandoning traditional lithographic techniques in favor of patterning graphite gates at sub-100 nm length scales using a resist-free process which takes advantage of atomic force microscope-actuated local anodic oxidation (AFM-LAO) of graphite [25]. [1] These gates are then integrated directly into a van der Waals heterostructure using a low-strain variation of the standard dry-transfer process [40, 55, 48]. Fig. 2.4a-c portray a schematic description of this processs. Fabrication begins with the use of an atomic force microscope (AFM) to locally oxidize[48, 25] a region of the graphite flake. In this process, a conductive AFM tip is brought close to the graphite surface in a humid environment. Capillary forces form a nano-scale water meniscus[70] connecting the tip and graphite surface. When a high frequency excitation is applied to the tip, the voltage drop across the water meniscus catalyzes oxidation of the graphite into gaseous and amorphous byproducts. Scanning the tip across the graphite surface while this reaction occurs allows nano-scale subtractive lithography[25] without introducing contaminants to the two dimensional graphite bulk, as would occur in solvent-based resist removal processes (see Fig. 2.3). The patterned graphite gate can then be integrated into a van der Waals heterostructure through pick-up by an unpatterned van der Waals flake (see Fig. 2.4b-c) to produce a wide array of geometries, several examples of which are depicted in Figs. 2.4d-f.

In the anodic oxidation process, amorphous residue–likely carbon and carbon oxides–typically remains, manifesting as features localized at critical interfaces in the AFM topographs of Figs. 2.4(g-i). However, these byproducts adhere more strongly to the orig-

[1]This technique is discussed at length in Chapter 2, however I will briefly recap here for the sake of making this chapter reasonably self-contained.

inal SiO2 substrate than to the hBN flake used for pick-up. This results in a self-cleaning process that enables the transfer of pristine microstructures into the middle layers of the heterostructure. Figs. 2.4(j-l) show AFM topographs of the patterned graphite after pick-up by a hexagonal boron nitride flake–*i.e.*, imaged with the graphite in the configuration shown in Fig. 2.4c. Etch byproducts visible in the as-cut graphite (Fig. 2.4g-i) are not transferred, leaving pristine nano-scale subtractive patterns. Notably, in this process the areas closest to the critical regions are not exposed to additional fabrication residues, in contrast to graphite gates patterned by plasma-etching [24].

Remarkably, our process permits transfer of high-density patterns without degradation or tearing. Three examples are shown in Figs. 2.4d-f, depicting a quantum point contact, quantum dot array, and Fabry-Pérot interferometer, all meant to be operated in the quantum Hall regime. We note that to preserve the alignment of fine lithographic features during pattern transfer, the patterned graphite flakes must remain contiguous: free-floating graphite pieces will typically slide during transfer leading to electrical shorts between nominally disconnected areas. In most cases, additional conventional subtractive processing is used to electrically disconnect different gate regions and make electrical contact to sample and gate layers, this is typically done with a standard RIE plasma etch. However, certain desirable electrostatic geometries can be realized using complementary patterns in both the graphite top- and bottom- gates and aligning the two during transfer. An example of this strategy, used to construct a quantum Hall edge state Fabry-Pérot interferometer, is shown in Figs. 2.4f, i, and l, in which a patterned bottom gate is used to create an isolated, independently density-tunable region in a graphene device without requiring a free-floating gate.

While the process described above produces *topographically* pristine gate geometries, topography alone is not a guarantee of electronic quality. In particular, without electrical characterization, we cannot exclude that the anodic oxidation itself produces unaccept-

ably large local potentials on the graphite edge. To qualify our technique, then, we use a monolayer graphene quantum point contact (QPC) device operating in the quantum Hall regime. A QPC is formed when a narrow constriction in a two-dimensional device restricts the number of quantized channels through which electrons can flow[71]. In the quantum Hall regime, when the constriction is on the order of the magnetic length ℓ_B, the transmission of chiral edge modes through the QPC varies sensitively with the width. To form a QPC using our fabrication method, we start from the cross gate geometry of Fig. 2.4d, and perform additional lithographic processing (see Appendix A) to isolate the four quadrants of the graphite top gate producing four isolated gates we denote North (N), South (S), East (E) and West (W). Voltages applied to these gates and a global graphite bottom gate can be used to deplete the monolayer into the $\nu = 0$ gap in the N and S regions, forming a narrow constriction, with the filling factor in the E and W regions held constant. An optical micrograph of the completed device is shown in Fig. 3.2a.

3.4 Partitioning of Integer Quantum Hall Edge Modes

To characterize the operation of our QPC we measure the four-terminal 'diagonal conductance,' G_{D} (this is essentially a Hall conductance across the device, see Appendix B for details of the measurement setup), which in the integer quantum Hall (IQH) regime gives a direct measure of the number of edge modes N_{qpc} transmitted across the device such that $G_{\mathrm{D}} = N_{\mathrm{qpc}}\frac{e^2}{h}$[72, 22]. Fig. 3.2b shows G_{D} measured at $B = 6$ T and T=300 mK as the gate voltages are adjusted to tune N_{qpc} from 0 to 2. In this measurement, we fix the value of $V_{\mathrm{EW}} + \alpha V_{\mathrm{B}}$ (where $\alpha = c_b/c_t$ is the ratio of the bottom- and top-gate capacitances to the monolayer, and V_{EW} denotes a single voltage applied to the E and W gates – see Fig. 3.1a-c). This fixes the bulk filling factor in the E and W regions within the $\nu = -4$ plateau. We also fix $V_{\mathrm{NS}} + \alpha V_{\mathrm{B}}$ to keep the N and S regions within the $\nu = 0$

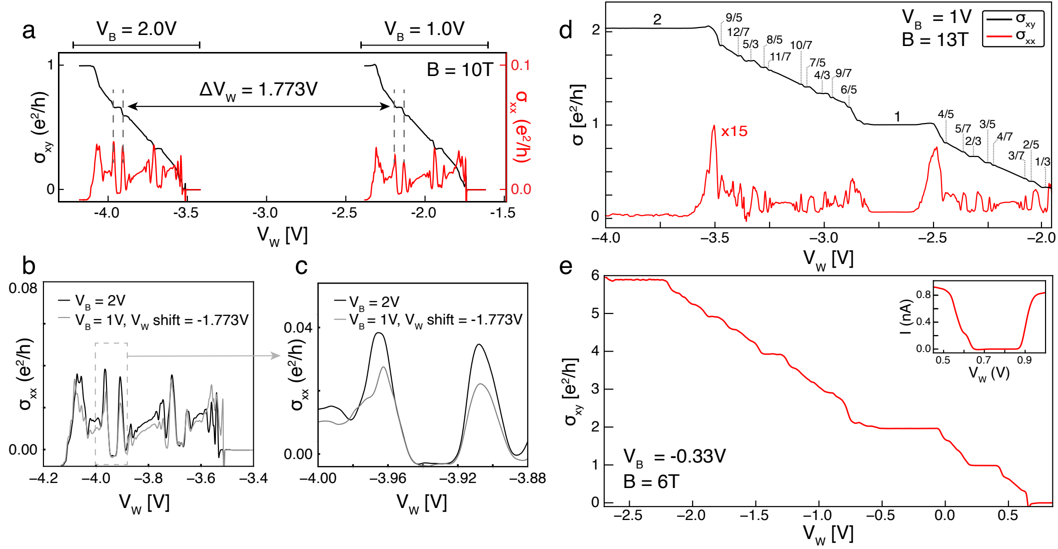

Figure 3.1: **(a)** Longitudinal and Hall conductance in the W region of the device for two values of the bottom gate, $V_B = 1.0V$ and $V_B = 2.0V$, at B = 10T. All other regions are set to $\nu = 0$. **(b)** Calculated shift ΔV_W applied to the $V_B = 1.0V$ trace shows overlap of identical features between the two traces. **(c)** The region of vanishing longitudinal conductance in ν = -2/3 was used to numerically determine the shift ΔV_W by minimizing the sum of the norm-squared differences between the two traces over a region around ν = -2/3. **(d)** σ_{xx} and σ_{xy} versus V_W at B = 13T and $V_B = 1V$. **(e)** $1/R_{xy}$ measured on the west side of the device versus V_W while $\nu_N = \nu_S = \nu_E = 0$ is kept fixed, and $V_B = -0.33V$. Inset: current measured during $1/R_{xy}$ sweep showing $\nu = 0$ gap.

plateau. Tuning $V_{\rm EW} - V_{\rm B}$ then controls the QPC width independent of the bulk filling factors in the four quadrants. As is evident in Fig. 3.2b, we observe integer-quantized conductance plateaus separated by monotonic transitions; in particular, we do not observe non-monotonic conductance features characteristic of disorder-mediated or resonant tunneling effects, typical of quantum point contacts in both III-V semiconductors and graphene [32, 22, 24, 38, 73].

Fig. 3.3a shows a map of the $G_{\rm D}$ at B=6 T and T=300 mK as we vary the $V_{\rm NS} \equiv V_N = V_S$ and $V_{\rm EW} \equiv V_E = V_W$. As expected for IQH transport, the conductance maps in Fig. 3.3a-c are dominated by regions of fixed conductance at integer multiples of $\frac{e^2}{h}$, corresponding to transmission of an integer number of chiral edge states across the device.

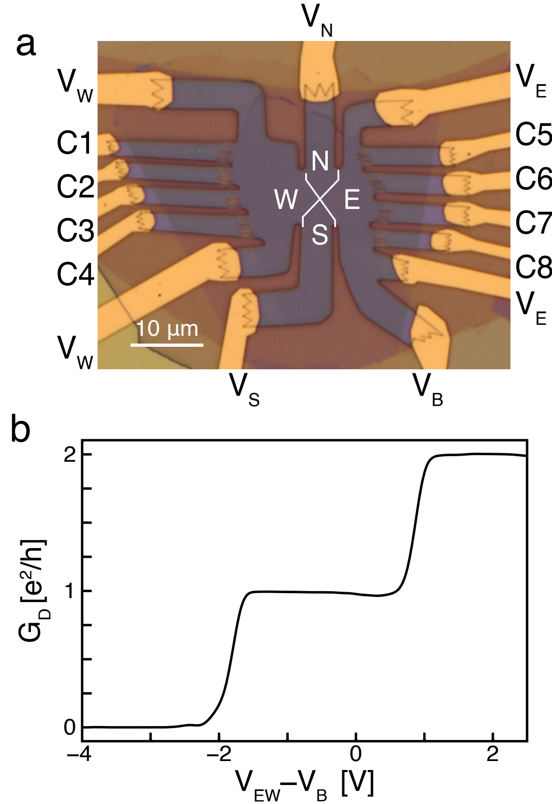

Figure 3.2: **Quantum point contact operation in the integer quantum Hall regime. (a)** Optical micrograph of measured device. Transport contacts are denoted by C1-C8. Gate contacts are labeled by V_i with an appropriate subscript to denote which region the gate controls. **b)** Diagonal conductance, G_{D}, versus $V_{\mathrm{EW}} - V_{\mathrm{B}}$ demonstrating integer QH edge mode partitioning at the QPC. Here the east/west gates are swept simultaneously with the back gate such that the bulk filling factor, $\nu_{EW} \propto V_{\mathrm{EW}} + \alpha V_{\mathrm{B}}$, remains constant. Additionally, $\nu_{NS} \propto V_{\mathrm{NS}} + \alpha V_{\mathrm{B}} = 0$ is held constant.

For each conductance map in Fig. 3.3a-c, the graphite bottom gate, V_{B}, is fixed to a different voltage. Using the capacitive lever arm $\alpha \equiv C_B/C_T = 1.773$ (see Fig. 3.1a-c), the ranges of V_{EW} and V_{NS} are chosen such that the electronic density in each region of the monolayer is kept in the same range in all three panels. The precise mapping of gate voltages to ν is determined by measuring the Hall effect in the W quadrant (see Fig. 3.1d-e).

Tracing the behavior of the transitions between conductance plateaus reveals two

distinct regimes. In the first, plateau transitions are controlled by only $V_{\rm EW}$ *or* $V_{\rm NS}$, producing steps in $G_{\rm D}$ along either horizontal or vertical lines in the $(V_{\rm NS}, V_{\rm EW})$ plane. In this regime, the diagonal conductance is primarily determined by the number of edge states transmitted along the physical edge of the device, far from the QPC. For example at point I in Fig. 3.3a, the filling factor of the north and south regions, $\nu_{NS} = \nu_N = \nu_S$, is fixed to $\nu_{NS} = 0$, while the E/W regions are fixed to $\nu_{EW} = \nu_E = \nu_W = -4$. Point I sits to the right of a *vertical* transition, solely controlled by $V_{\rm NS}$, where $G_{\rm D}$ goes from 0 to 1. Decreasing $V_{\rm NS}$ starting at point I changes the filling ν_{NS} from 0 to -1, adding an edge mode in the N/S regions at the physical device boundary and increasing $G_{\rm D}$.

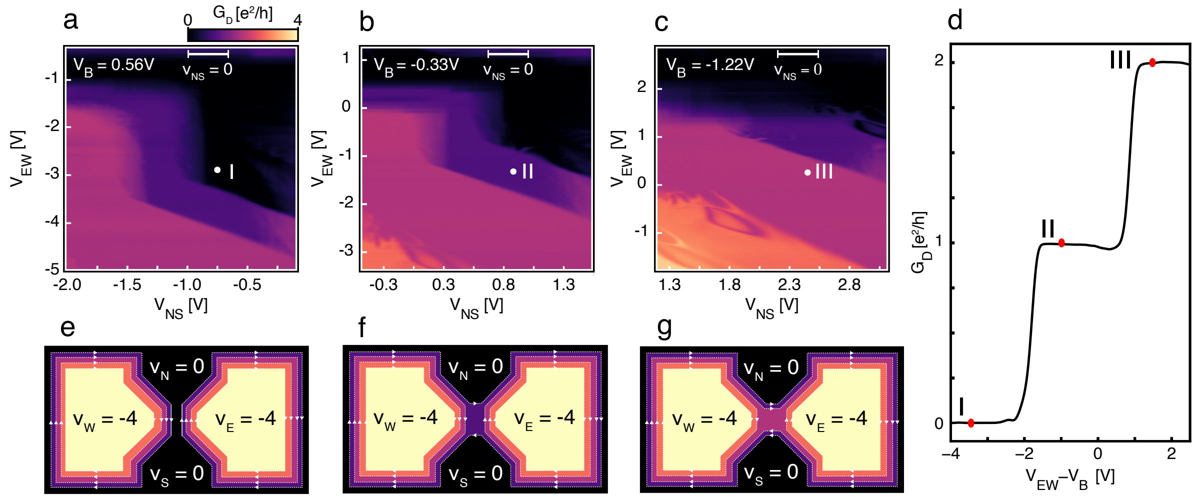

Figure 3.3: **Quantum point contact operation in the integer quantum Hall regime.** **(a)** Diagonal conductance $G_{\rm D}$ plotted as a function of $V_{\rm NS}$ and $V_{\rm EW}$ at B=6 T and T=300 mK for $V_{\rm B} = 0.56$, **(b)** $V_{\rm B} = -0.33$, and **(c)** $V_{\rm B} = -1.22$. In panels a-c, $V_{\rm NS}$ and $V_{\rm EW}$ denote the voltages applied to north and south or east and west gates, respectively. The ranges of $V_{\rm NS}$ and $V_{\rm EW}$ are chosen such that the filling factor $\nu_{EW} = \nu_E = \nu_W \in [-6, 0]$ and $\nu_{NS} = \nu_S = \nu_N \in [-2, 1]$ for each conductance map in a-c. The range over which $\nu_{NS} = 0$ is marked in each plot by the white bar. **(d)** The same trace as in the main text Fig. 2b. The trace in the multidimensional parameter space intersects the $G_{\rm D}$ maps of panels a-c at the position marked I, II, and III **(e)** Schematic depiction of the filling factors within the QPC at point I in panel a, **(f)** point II in panel b, and **(g)** point III in panel c. For points I-III, the filling factor in the N/S/E/W regions is constant but the fringe fields vary with $V_{\rm B}$, fully modulating transmission of the two outermost edge modes through the QPC.

In the second regime, the plateau transitions are influenced by *both* V_{EW} and V_{NS}, producing a step in G_{D} along lines of slope ≈ -1 in the $(V_{\mathrm{NS}}, V_{\mathrm{EW}})$ plane. This behavior is expected when edge modes are transmitted through the center of the QPC, where they are equally sensitive to the fringe electric fields of each of the N/S/E/W gates. Consider again point I which sits just above a *diagonal* transition, where G_{D} goes from 0 to 1. Near the transition, $\nu_{NS} = 0$ and no conduction across the device can occur along the etched boundary – all current must be carried via edge modes through the QPC. However, at the transition, G_{D} may change sharply by *either* an equal perturbation in V_{NS} or V_{EW} while maintaining $\nu_{NS} = 0$. The existence of such transitions in G_{D} implies the filling factor in the QPC center can be held fixed via equal and opposite modulations of V_{NS} and V_{EW}: lines separating differing values of G_{D} which are parallel to $V_{\mathrm{NS}} + V_{\mathrm{EW}} = 0$ demarcate sharp boundaries between regions of different filling factor in the center of the QPC itself.

The location in density of the *diagonal* steps in G_{D} shift as a function of V_{B} (Figs. 3.3b-c), in contrast to the horizontal and vertical transitions whose locations in density are unaffected. This behavior follows from the device electrostatics: Near the device boundary, transport is determined directly by the bulk filling factor in the N/S/E/W regions. Since the graphite bottom gate uniformly modulates the density of the whole monolayer, the role of V_{B} is merely to induce a chemical potential shift in the whole device which is compensated by offsetting the applied gate voltages. This is not true in the central region, however, which is doped by the fringe fields of N/S/E/W gates.

It follows that tuning the bottom gate while keeping the densities in the N, S, E, and W regions constant changes the electrostatics of the QPC. Points I-III in Figs. 3.3a-c correspond to identical carrier densities away from the QPC, with $\nu_{EW} = -4$ and $\nu_{NS} = 0$. At point I, all the edge modes are pinched off and $G_{\mathrm{D}} = 0$. As V_{B} is decreased, the filling factor in the QPC changes, leading to the transmission of one additional

Index	$G_{\mathrm{D}}[\frac{e^2}{h}]$	ν_{EW}	ν_{NS}	ν_{qpc}
I	1	-4	0	-1
II	1	-2	-1	-1
III	1	-1	-2	0
IV	1	-1	-2	-1
V	2	-2	-2	-2
VI	0.7	-1	-4	-2

Figure 3.4: Key Table for Fig. 3.5

edge modes at point II and and two additional modes at point III. Fig. 3.3d shows the continuous evolution between points I, II, and III as a function of $V_{\mathrm{EW}}-V_{\mathrm{B}}$, corresponding to tuning the QPC electrostatics. A schematic depiction of the corresponding filling factor maps in real space are shown in Figs. 3.3e-g.

The full parameter space that determines the value of G_{D} when tuned with V_{NS} and V_{EW} has features which depend on either V_{NS} or V_{EW} individually or features perpendicular to $V_{\mathrm{NS}}+V_{\mathrm{EW}}=0$ (indicated as dashed white lines in Fig. 3.5a). The former are dominated by physics at the etched edge of the device where the edge modes of a $pp'p$ junction are fully equilibrated [22]. The latter are interpreted as boundaries between operating points that have differing values of ν_{qpc} – the filling factor in the center of the device, determined by the fringe fields of the four quadrant top gates (for a fixed V_{B}). Fig. 3.5a has several points denoted by roman numerals which correspond either to QPC operation or conductance through the edge of the device. Fig. 3.5b shows an illustration of the inferred filling factor in each region of the device for each point marked in Fig. 3.5a. This information, along with the associated G_{D} for each point is repeated in the table in Fig. 3.4.

Point VI is of particular note since it falls to the left of a boundary in G_{D}, where G_{D} is a fractional value below 1, that is intersected by a dashed line. This indicates the transition is sensitive to the potential at the QPC, but is in a region where at least one

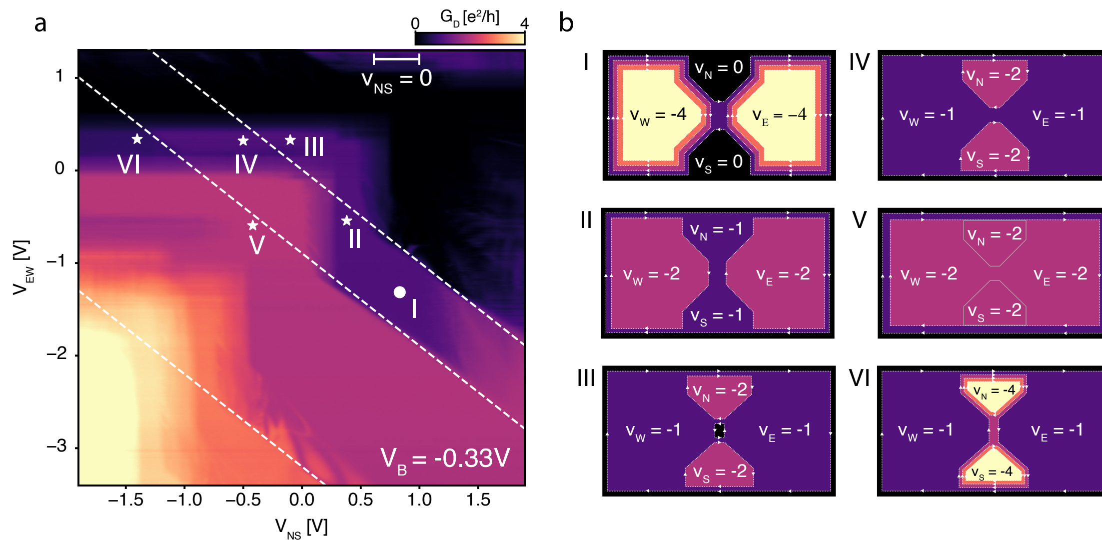

Figure 3.5: **Extended Integer QPC Operation:** **(a)** G_D plotted versus V_NS and V_EW with $V_\mathrm{B} = -0.33V$. Lines parallel to $V_\mathrm{NS} + V_\mathrm{EW} = 0$ demarcate transitions between integer G_D values indicating a rapid change in the density at the QPC. Roman numerals I-VI correspond to various unique combinations of ν_{NS}, ν_{EW}, and ν_{qpc}, where ν_{qpc} is the filling factor at center of the QPC. **(b)** Illustrations of the inferred filling factor in each region of the device corresponding to the operating points in panel a.

edge mode is transmitted along the edge of the device since $\nu_{NS} < -1$. The corresponding filling factors at VI are $\nu_{NS} = -4$, $\nu_{EW} = -1$, and $\nu_{qpc} = -2$. Starting from point IV, where $\nu_{qpc} = -1$, as V_{NS} becomes more negative, the filling factor in the QPC is more strongly doped towards ν_{NS}. Eventually, at point VI, the filling factor in the QPC increases to $\nu_{qpc} = -2$, and an edge mode bridges the north and south regions through the $\nu_{EW} = -1$ bulk. This creates a scattering channel across the device that reduces the conductance to the expected value of $G_{\mathrm{D}} \sim 2/3$ for a $pp'p$ junction of the given filling factors (-1, -2, -1) [22, 23]. This shows it is possible to see QPC behavior even with a background conductance through the etched edge of the device, however the value of G_{D} requires some interpretation. Consequently, for most experiments presented in the this thesis we focus exclusively on regimes where there is no conduction along the edge of the device, simplifying possible interpretations of fractional values of G_{D}.

3.5 Partitioning of Fractional Quantum Hall Edge Modes

While we are able to transmit multiple edge modes through the QPC in the absence of defect mediated resonant states, an even more stringent characterization of disorder at the QPC can be obtained in the fractional quantum Hall (FQH) regime. Fig. 3.7a shows G_{D} plotted as a function of V_{B} and $V_{\mathrm{NS}} + \alpha V_{\mathrm{B}}$ at B=13T and T=300mK. Throughout this range, the filling factor of the E and W region is fixed at $\nu = -5/3$, and that of the N and S regions is fixed within the $\nu = 0$ plateau. Data taken along the white dashed line in Fig. 3.7a is plotted in Fig. 3.7b, and shows two distinct quantized plateaus at $G_{\mathrm{D}} = 4/3$ and $5/3$, in addition to the integer plateau at $G_{\mathrm{D}} = 1$. This observation suggests the $\nu = -5/3$ state hosts two edge modes each with conductance $-\frac{e^2}{3h}$. Notably,

this is not consistent with theoretical expectations for a sharp confining potential[74, 75]. In that limit, a pair of counter propagating edge modes is expected where one carries a conductance of $-\frac{e^2}{h}$ and the other carries a conductance of $\frac{e^2}{3h}$ (see Fig.3.8a); evidence for this structure was observed recently in carefully designed III-V heterostructures[76]. Our observation is instead consistent with a picture of the 5/3 edge which includes the effects of edge state reconstruction resulting from a soft confinement potential defining the boundary of the topological bulk[77]. Theoretically, softly confined edges of hole-conjugate fractional quantum Hall states are expected[78, 79] to host neutral modes along with the observed fractionally quantized charged modes (see Fig. 3.8b). While these neutral modes do not directly couple to an applied electric field, they may affect thermal transport or renormalize the tunneling spectra of nearby charged modes [80].

The edge modes at the boundary of a fractional quantum Hall state are expected to behave like chiral Luttinger liquids[30, 80]. In this state of matter, the quasi-particle wave functions are orthogonal to the electrons from which they are microscopically constructed. This 'orthogonality catastrophe' results in a soft gap in the electron tunneling density of states which vanishes like $\rho \propto (E - E_F)^{1/g-1}$, where the constant g is known as the Luttinger parameter [81], this will be discussed in further detail in the following sections, and was overviewed in Chapter 1. A remarkable consequence of this fact is that even arbitrarily weak barriers between edge modes will suppress tunneling at sufficiently low temperature and bias voltage.

Fig. 3.7c shows G_{D} as a function of source-drain voltage V_{bias} and V_{NS}, corresponding to the dashed blue trajectory in Fig. 3.7a. The data shows a single sharp zero-bias conductance dip throughout the transmission plateau at $G_{\mathrm{D}} \approx \frac{4}{3}\frac{e^2}{h}$–in contrast with the weak bias dependence observed for an integer edges (see Fig. 3.6). In Fig. 3.7c, V_{NS} tunes the electrostatic confinement at the QPC and thus the height of the tunnel barrier separating the two outermost edge modes incident upon the junction. As expected, a

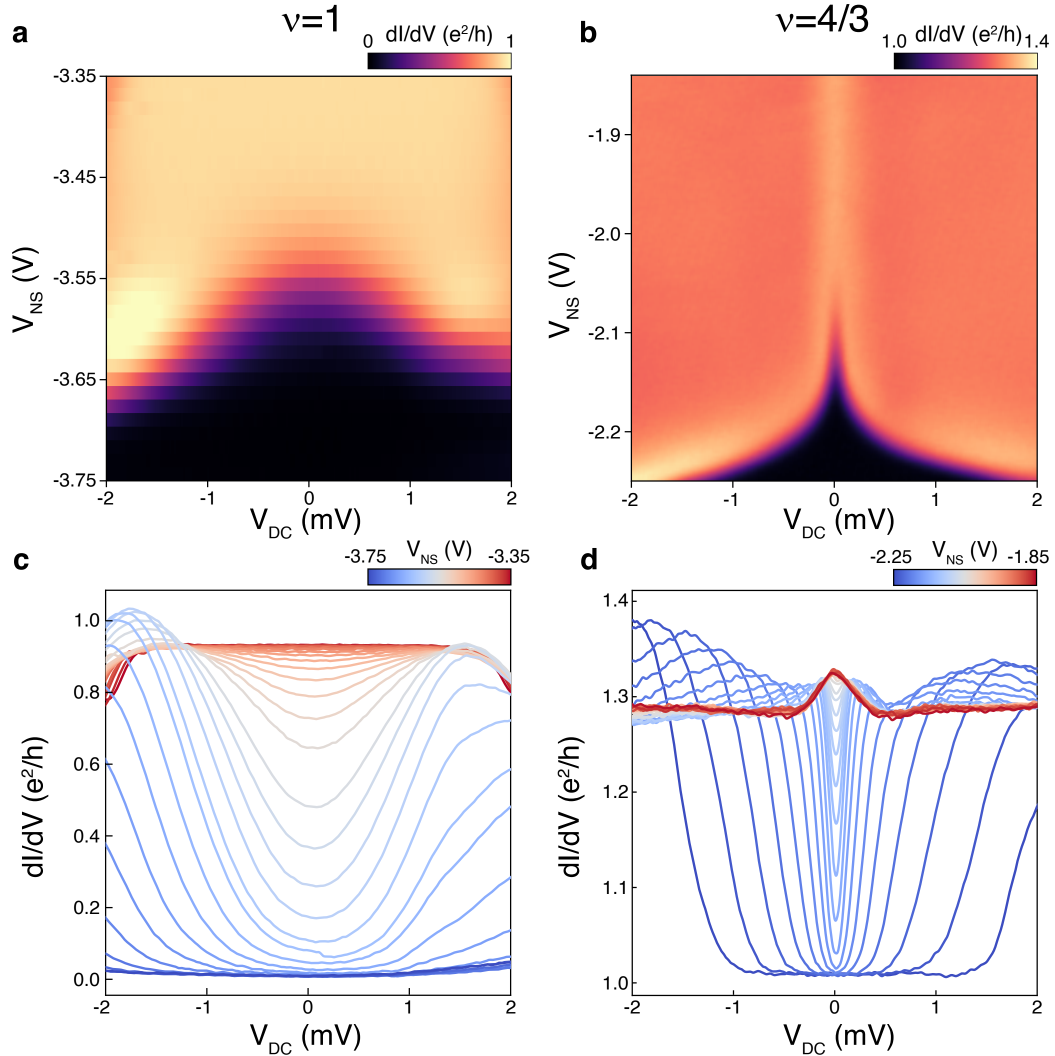

Figure 3.6: **(a)** Plot of the tunneling conductance across an integer conductance step, in the $\nu = 1$ state. In the fully reflecting and fully transmitting limits, the conductance is constant for V_{DC} less than about ≈ 1 mV, and smoothly varies as the edge is transmitted. **(b)** For a fractional edge state, the conductance remains highly suppressed even when the edge state is partially transmitted, with a sharply nonlinear dI/dV near $V_{DC} = 0$. Even when the edge state is fully transmitted, and dI/dV $(V_{DC} = 0) = 4/3$, the tunneling conductance remains nonlinear. **(c)** and **(d)** present linecuts of the data in (a) and (b) respectively for comparison.

decrease in V_{NS} lowers the potential barrier at the QPC and enhances transmission. The lack of resonant structure in Fig. 3.7c, features observed in previous experiments[32, 38, 73, 22], even at high transmission suggests that scattering between edge modes occurs at a single, gate-controlled saddle point.

To compare our data with expectations from the chiral Luttinger liquid theory [30, 80], Fig. 3.7d shows the reflection coefficient, R, which measures the probability of backscattering the outermost fractional edge mode (see also Appendix C for a detailed analysis, which follows Refs. [82, 38, 83]). For two fractional quantum Hall edges which are weakly tunnel coupled via the exchange of quasi-particles, the reflection coefficient R, as a function of V_{bias}, may be computed perturbatively [30, 84]. Evidently, even for high transmission, voltage bias alone can tune R from over 75% to nearly zero, demonstrating that the incident edge modes become decoupled a low energies – a manifestation of the 'orthogonality catastrophe' – a hallmark of chiral Luttinger liquid physics.

At zero bias, when quasi-particle backscattering is weak (corresponding to small R), R is expected to follow a simple power law with respect to temperature, $R \propto T^{2g-2}$. We plot the zero-bias R in Fig. 3.7e. For T between 300-550mK—corresponding to $R \lesssim 0.4$—the reflection coefficient is well fit by a power law with $g = 0.47$. In this weak-backscattering regime, the dependence of R on V_{bias} and T is theoretically expected[84] to follow a scaling form,

$$\frac{R(x)}{T^{2g-2}} = A\beta(g + i\frac{e^*x}{2\pi}, g - i\frac{e^*x}{2\pi}) \times \left[\pi \cosh(\frac{e^*x}{2}) + 2\sinh(\frac{e^*x}{2})\text{Im}[\Psi(g + i\frac{e^*x}{2\pi})]\right] \quad (3.1)$$

where $x = \frac{eV_{\text{bias}}}{k_bT}$ is the scaled voltage bias, β and Ψ denote the corresponding Euler integrals, e^* is the effective quasi-particle charge in units of the electron charge, and A is a constant related to the height of the tunnel barrier.

It follows from this equation that if $R(x)$ is scaled appropriately by the temperature,

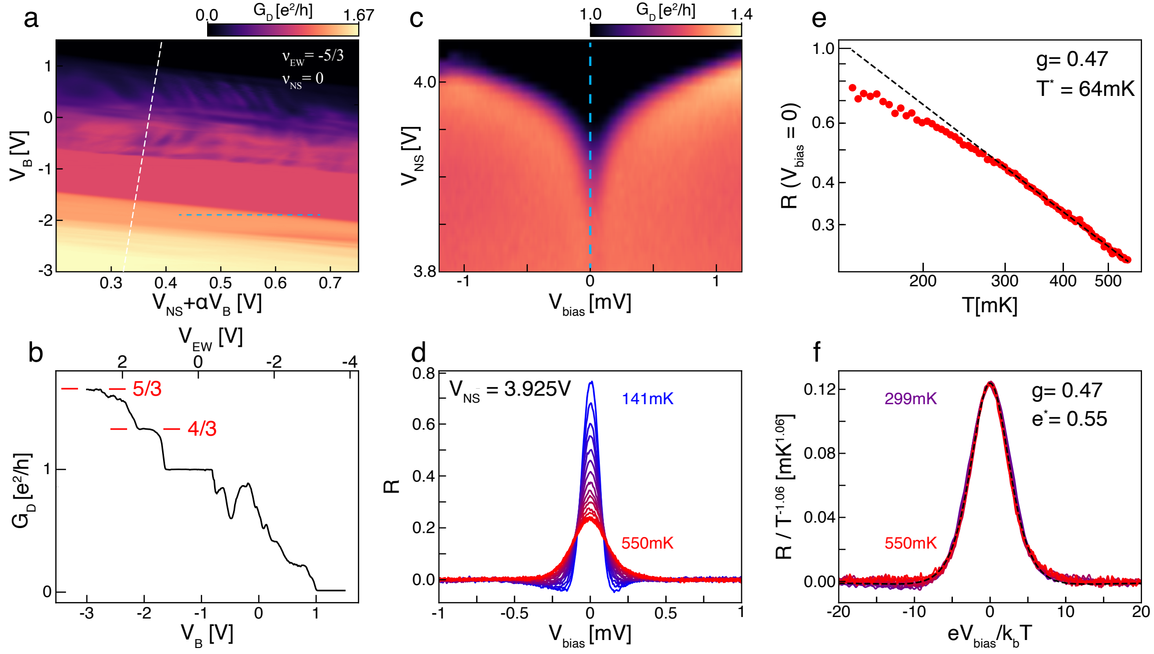

Figure 3.7: **Partitioning of fractional quantum Hall edges and quasi-particle tunneling. (a)** $G_{\rm D}$ map at fixed $\nu_{EW} = -\frac{5}{3}$. As $V_{\rm B}$ is adjusted along the y-axis, $V_{\rm EW}$ is swept in tandem to keep $V_{\rm EW} + \alpha V_{\rm B} \propto \nu_{EW}$ constant while allowing $V_{\rm B} - V_{\rm EW}$ to vary, adjusting the saddle point electrostatics. On the x-axis, the range of $V_{\rm NS}$ is varied as $V_{\rm B}$ changes in order to keep the range $V_{\rm NS} + \alpha V_{\rm B}$ within the $\nu = 0$ plateau. **(b)** $G_{\rm D}$ along the dashed white contour in panel a. Two fractional plateaus are highlighted at 4/3 and 5/3 resepctively. **(c)** Bias dependence of the $G_{\rm D} = \frac{4}{3}$ plateau, along the dashed blue line shown in panel a. The tunneling conductance is suppressed at zero bias well into the plateau, a distinct signature of chiral Luttinger liquid behavior. **(d)** Extracted back-scattered conductance, R, versus scaled DC bias, $V_{\rm bias}$, at a fixed $V_{\rm NS} = 3.925V$ for the temperatures $T = 141\,$mK, 169 mK, 199 mK, 229 mK, 259 mK, 289 mK, 320 mK, 350 mK, 379 mK, 410 mK, 440 mK, 470 mK, 499 mK, 530 mK, 534 mK, 540 mK, 544 mK, 550 mK. **(e)** Back-scattered conductance, R, at zero DC bias versus temperature. Power-law behavior onsets above 300 mK; we find $R \propto T^{-1.057\pm0.008}$, yielding a Luttinger parameter of $g = 0.47 \pm 0.004$. The cross-over energy scale between weak electron tunneling and weak quasi-particle back-scattering is estimated to be $T^* = 64 \pm 3\,$mK (notably power-law behavior with negligible contributions from electron tunneling for quasi-particle back scattering is not expected unless $T >> T^*$). **(f)** Scaling collapse of DC bias dependent tunneling curves for different temperatures above power-law onset. Here $R/T^{-1.06}$ is plotted against $eV_{\rm bias}/k_bT$ for the temperatures T = 299 mK, 320 mK, 340 mK, 360 mK, 379 mK, 399 mK, 420 mK, 440 mK, 460 mK, 480 mK, 499 mK, 520 mK, 540 mK. The black-dashed is a fit to the expected bias dependence for a chiral Luttinger liquid with g = 0.47 (see Eq. (3.1)) yielding an effective quasi-particle charge of $e^* = (0.55 \pm 0.001)|e|$.

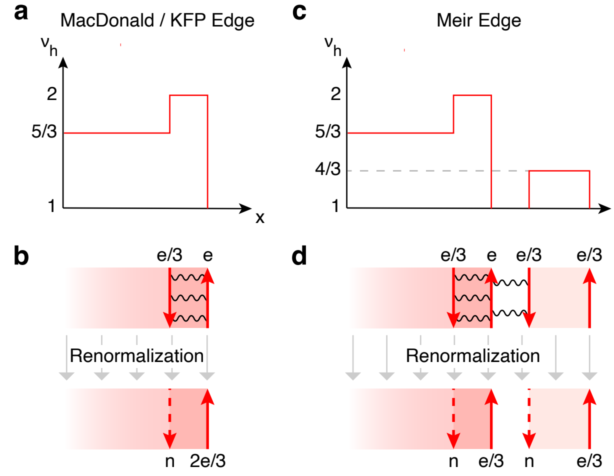

Figure 3.8: **(a)** Hole-conjugate FQH states such as the $\nu = 2/3, 5/3$ states can be modeled by a Laughlin- like FQH state of holes within a bulk integer quantum Hall state, leading to a small strip of increased filling factor around the edge of the sample. This is shown schematically in panels a and c by plotting the filling factor of holes $\nu_h \equiv -\nu$ at the boundary between a $\nu = -5/3$ and $\nu = -1$ state, where the relevant fractional edges measured in the experiment occur. The MacDonald model [74] of the resulting edge structure posits a downstream integer mode at the outermost edge of the sample, as well as an upstream (counter-propagating) fractional mode. (b) In real experiments, the two counter-propagating charged modes are rarely observed, but rather mix through the presence of inter-edge interactions, yielding a single effective charge-2e/3 mode propagating downstream, as well as an upstream charge-neutral mode, as explained by the Kane-Fisher-Polchinski model [75]. (c) A sufficiently soft confining potential may make it energetically favorable to redistribute the charge in the system and create an additional strip of density $\nu_h = 4/3$, introducing a set of two additional counter-propagating fractional edge modes: the Meir model [79]. (d) In a real system, where these modes can also mix, the resulting mode structure may contain two downstream fractional-conductance modes as well as two upstream neutral modes. This scenario is consistent with the observation of multiple fractional conductance steps within the $\nu = -5/3$ state.

tunneling spectra taken in the temperature range where the zero-bias power law applies should follow a universal curve, with e^* providing a single additional adjustable parameter. Fig. 3.7f shows $R/T^{-1.06}$ versus eV_{bias}/k_bT for several temperatures in the range of 300 mK to 550 mK. The curves are observed to collapse onto each other fixing $g = 0.47$. The collapsed curves are then averaged and fit to Eq. (3.1) extracting the quasi-particle charge as $e^* = 0.55 \pm 0.001$.

The observed scaling collapse provides evidence of tunneling between chiral Luttinger liquids at a single point within the QPC. However, the measured values of $g = 0.47$ and $e^* = 0.55$ are at odds with predictions that that the boundary of a fractional quantum Hall phase should host a chiral Luttinger liquid with a quantized Luttinger parameter and quasi-particle charge, namely $g = 1/3$ and $e^* = 1/3$[30]. We attribute this discrepancy to the presence of neutral modes at the $\nu = -5/3$ boundary, consistent with an electrostatically shallow edge permitting significant Coulomb-induced reconstruction effects[80, 79] (See Fig. 3.8 2b). While a universal regime is always expected to exist, for the electrostatic configuration explored here, this regime most likely occurs significantly below 300 mK, outside of the weak quasi-particle backscattering limit. Notably, past experiments on a variety of fractional Hall states in III-V semiconductor systems[85, 86, 32, 38, 85, 86] have also shown significant deviations from the expected universal behavior. The deviation from universality in all of these experiments, including the one presented here, is likely traceable to the complex edge structure arising from the shallow edge confinement typical of gate-defined tunnel barriers.

3.6 Tuning Edge Sharpness *in situ*

This deficiency may be addressed in our geometry using *in situ* control of the confinement potential. The softness of the confinement potential is quantified by the ratio

of $E_V \equiv e\frac{\partial \phi_{ext}}{\partial x}\ell_B$ (here x is the coordinate perpendicular to the confined edge, and ℓ_B is the magnetic length) and the Coulomb energy $E_C \equiv \frac{e^2}{4\pi\epsilon\ell_B}$. In our geometry, independent control of the voltages applied to the N/S, E/W, and bottom gates is equivalent to independent control of the filling factor in the E/W regions, the number of transmitted modes N_{qpc}, and E_V, allowing us to explore the effects of the confinement energy within the QPC independently of the barrier height.

To illustrate this, Figure 3.9a shows a map of G_{D} measured at $B = 2$ T with fixed $\nu = -6$ in the E/W regions. In this plot, moving along a diagonal from lower left to upper right reduces N_{qpc}, while moving along a diagonal from upper left to lower right increases E_V. We observe a qualitative change in the nature of the transition between $G_{\mathrm{D}} = 2\frac{e^2}{h}$ to $G_{\mathrm{D}} = 6\frac{e^2}{h}$ as a function of E_V. For small E_V—*i.e.* soft confinement—we observe distinct conductance plateaus corresponding to each integer quantum Hall state between $\nu = -2$ and $\nu = -6$, indicating that the four distinct edge modes corresponding to the $\nu = 3$ through $\nu = 6$ states can be individually partitioned. For large E_V, in contrast, the steps merge into one continuous jump from $G_{\mathrm{D}} = 2\frac{e^2}{h}$ to $G_{\mathrm{D}} = 6\frac{e^2}{h}$, with no discernible intermediate plateaus at partial transmission (see Fig. 3.9b).

This behavior can be understood in the context of the competition between E_V and E_C at the QPC. In the regime of Fig. 3.9, in the bulk, the four-fold spin and valley degeneracy of the Landau levels is lifted due to quantum Hall ferromagnetism[17]. In the presence of a soft confining potential, the electron system can lower its energy by forming islands of incompressible fluid at integer filling factor within the QPC saddle point, due to the emergence of E_C-scale integer quantum Hall ferromagnetic gaps. However, as E_V is increased it is no longer energetically favorable to form such incompressible islands within the QPC, and instead a smooth change in electron density at the QPC as function of transmission is preferred. Finite element electrostatics calculations show E_V/E_C is approximately 1.5 and 2.8 for the trajectories marked AB and CD in Fig. 3.9a,

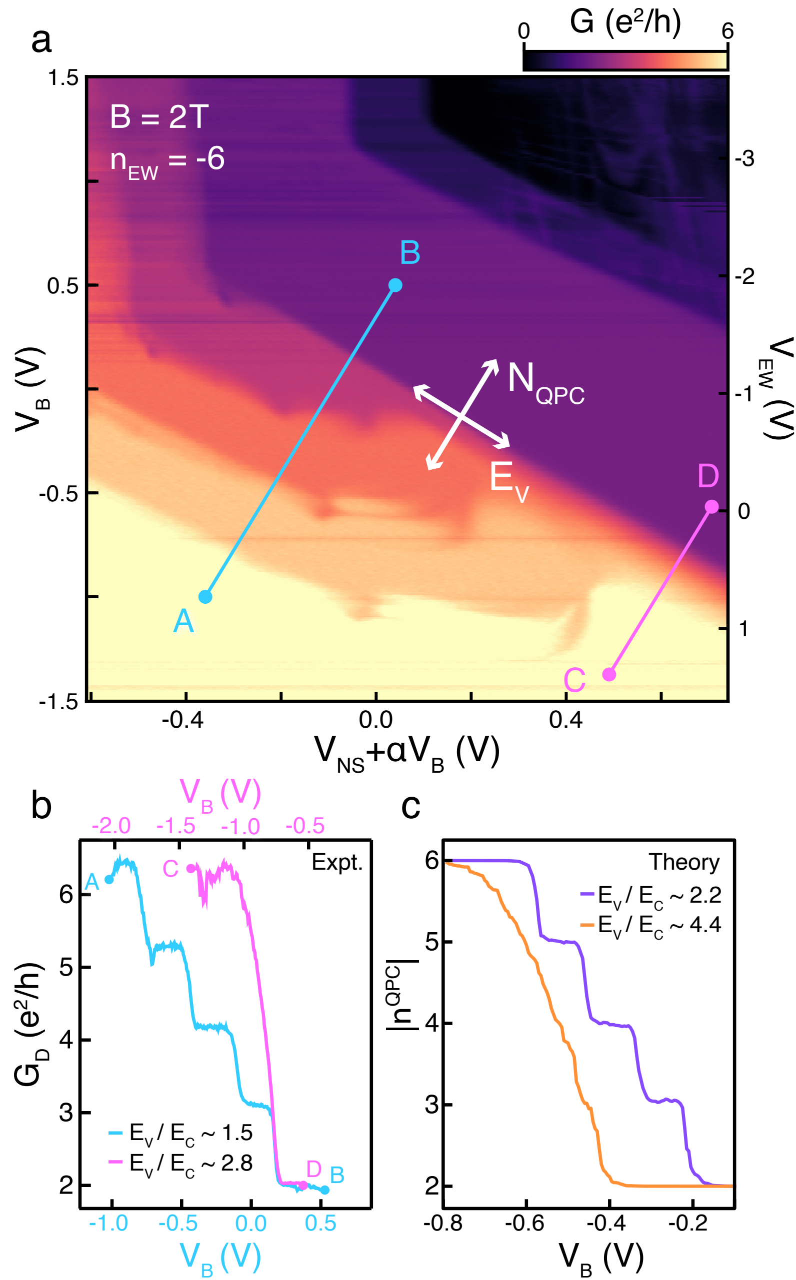

Figure 3.9: **Tuning edge sharpness via electrostatic gating. (a)**. G_D map at fixed $\nu_{EW} = -2$ at B = 2T. As in Fig. 3.7a, the gates are swept to maintain constant filling in the E, W regions while varying N_{QPC} and the sharpness of the confining potential. **(b)** Data of panel a along the marked trajectories, showing a qualitative change from individual $1\frac{e^2}{h}$ steps to a single continuous transition from $G_\mathrm{D} = 2\frac{e^2}{h}$ to $G_\mathrm{D} = 6\frac{e^2}{h}$ **(c)** Thomas-Fermi simulation of the filling factor at the center of the QPC.

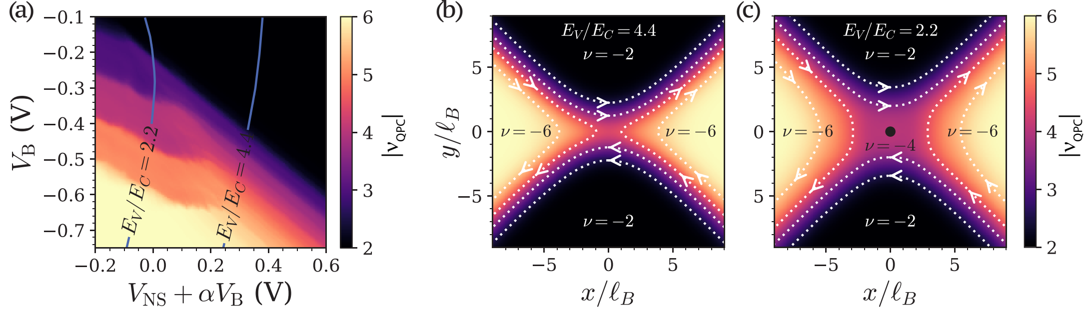

Figure 3.10: **(a)** The filling at the center of the QPC, ν_{QPC} as a function of V_B and $V_{NS} + \alpha V_B$, with the bulk filling of the east/west regions fixed at $\nu_{EW} = -6$. The result qualitatively mimics the measured G_D shown in Fig. 4a since ν_{QPC} determines the number of transmitted modes and therefore the diagonal conductance. Two line cuts which correspond to E_V/E_C =2.2 and 4.4 are shown in Fig. 4c. (b-c) Calculated filling factor ν for a realistic device geometry at B = 2 T for (b) $E_V/E_C = 4.4$ and (c) $E_V/E_C = 2.2$. When $E_V/E_C = 2.2$, there exists an incompressible island with $\nu_{QPC} = -4$ at the center of the QPC. Contours of $\nu = n + 1/2$ are shown as white dotted lines, indicating the location of chiral edge modes, two-pairs of which are transmitted through the QPC. This illustrates the rule $N_{QPC} = \nu_{QPC} + 2$.

respectively, where we take E_V from the maximum value of the potential slope at the boundary between the N and W regions.

To assess the plausibility of this explanation, we perform simulations of the electron density in our device within the Thomas-Fermi approximation (Thomas-Fermi calculations were preformed by Taige Wang and Kai Klocke, Michael P. Zaletel's students; plots are reproduced here with their permission. Details of the calculations may be found in [26, 28]). These simulations take as inputs the device electrostatics as well as a phenomenological model for the graphene chemical potential, which influences the quantum capacitance. For $E_V/E_C = 2.2$, the simulated density in the vicinity of the QPC exhibits a "wedding cake" profile, with well defined strips of integer filling, while for larger $E_V/E_C = 4.4$ the density drops sharply in a single step across the quantum point contact (see Fig. 3.10). As a heuristic proxy for G_D, we plot the simulated filling factor at the center of the QPC, $|\nu^{\mathrm{QPC}}|$, in Fig. 3.9c. The soft confinement regime shows a series of integer steps, while sharp confinement does not. This indicates that only in the case of

soft confinement do the edge-states remain well separated at the QPC, allowing their transmission to be partioned individually as observed in Fig. 3.9a.

As discussed previously, rearrangement of the electron density also causes significant effects on the edge in the fractional quantum Hall regime. These effects, referred to generally as "edge-reconstruction," can nucleate additional edge modes at soft potential boundaries with quantitative effects on tunneling behavior. We estimate $E_V/E_C \sim 1.3$ for the fractional quantum Hall tunneling experiment of Fig. 3.7, squarely in the regime where edge reconstruction effects are expected. Adjusting E_V such that the effects of E_C at the edge are negligible should allow exploration of universal edge mode physics in both tunneling and interferometry experiments. One thing to note, is that while E_V can be tuned in-situ, E_C is controlled primarily by the magnetic field, and in fact the ratio of E_V/E_C scales linearly with B. Generically one expects the effects of reconstruction to become more important at high magnetic fields where we wish to operate for FQH physics. The following section describes the effects of reconstruction at high field, and how despite their ubiquity E_V retains sufficient tunability that they can still be avoided.

3.7 Additional Effects of Edge State Reconstruction: Spontaneously formed Quantum Dots at an Electrostatic Saddle Point

Quantum point contacts (QPCs) operated in the quantum Hall regime ubiquitously show resonant tunneling features as edge modes are successively pinched off. These features are generally assumed to arise from uncontrolled disorder potentials introduced, for example, during the fabrication of local split gates[73, 32, 23, 22, 24]. Here we present evidence that repeatable resonant tunneling features can also arise independently of local

disorder via the same Coulomb-interaction driven mechanism that leads to edge-state reconstruction[78]. Theoretically, electrostatic confinement in the quantum Hall regime is characterized by the confinement energy, $E_V = e\frac{d\phi_{ext}}{dx}\ell_B$, where ϕ_{ext} is the applied electric potential. The spatial structure of the electron density in the presence of an external potential is controlled by the dimensionless ratio between E_V and the Coulomb energy, $E_C = \frac{e^2}{4\pi\epsilon\ell_B}$. In the sharp-edge regime, $E_V/E_C >> 1$, the electron density is expected to decrease sharply and monotonically at the edge of the quantum Hall bulk, leading to the simplest possible (unreconstructed) edge structure. At lower sharpness, corresponding to $E_V/E_C \sim 1$, a delicate balance between the Coulomb interaction and confining electric potential leads to a more complicated spatial structure in the electron density, which may include a nonmonotonic dependence of the density on position.

Edge-state reconstruction is often invoked as a complicating factor in experiments seeking to probe universal properties of fractional quantum Hall states. For example, the emergence of charge-neutral modes related to edge reconstruction is tied to the suppression of visibility in edge-state interference experiments[87] or the unexpected observation of upstream heat-transport in certain experiments[77, 88]. Universal, reconstruction-free edges[89] have been observed using scanning tunneling microscopy at the physical edge of graphene systems[90, 91], where the confining potential is atomically sharp. However direct measurements of the edge profile have been elusive at the softer, gate-defined edges that constitute the essential ingredient for mesoscopic devices, such as edge state interferometers, that allow for *in situ* edge state control. Such a device was discussed at length in the previous section, and while the demonstration of Luttinger liquid-like tunneling near the QPC suggests an absence of scattering centers in vicinity of the point contact, the resulting power laws were not quantized to the expected value for a 1/3 edge mode.

Here, we study a monolayer graphene device fitted with an electrostatically tunable

quantum point contact (same device studied in the previous section). Our geometry allows the sharpness of the confinement potential at the QPC to be controlled *in situ* (see Fig. 3.9), allowing us to directly probe the nature of the edge through its effects on the transmission of charge through the point contact. Our main result is an unexpected manifestation of Coulomb-induced reconstruction: the spontaneous formation of a quantum dot localized at an electrostatic saddle point. Our observations imply a local discrepancy between the *applied* electrostatic potential set by the voltages applied to each gate electrode and the *total* electronic potential, which takes into account electron-electron interactions and the finite compressibility of the 2DEG at high magnetic fields.

We study a dual-graphite gated hBN-encapsulated graphene van der Waals heterostructure described previously. To recap, local anodic oxidation lithography [25] is used to pattern an "X" shape in a graphite flake, which is then integrated into the van der Waals heterostructure[26]. A subsequent reactive ion etch defines the overall device outline, electrically separating the graphite into four separate gates which we label north (N), south (S), east (E) and west (W). Together, these tune the electron density in each of four quadrants separately. The E and W gates are used to tune the electron density on either side of the device while the N and S gates deplete the electron density to form the QPC constriction. The graphite bottom gate, controlled by a voltage V_B, can be used in conjunction with the top gates to control the fringe-fields at the boundaries between all four regions while maintaining a fixed electron density within the bulk of each quadrant, directly tuning E_V/E_C along the edge and at the potential saddle point. This fabrication method, by avoiding subtractive processing in the critical regions of the completed device, results in significantly lower disorder within the quantum point contact[26, 29].

To characterize the operation of our QPC we excite an AC voltage on one side of the device and measure the current I into a contact on the opposite side of the QPC and the diagonal voltage drop V_D to calculate the four terminal "diagonal conductance",

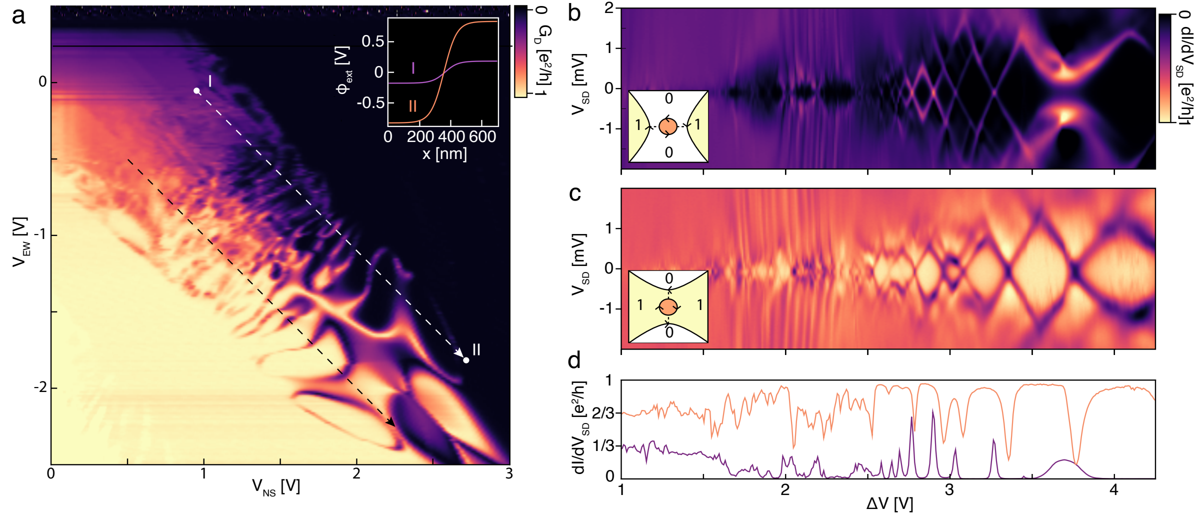

Figure 3.11: **Coulomb blockade at a gate-induced saddle point.** **(a)** G_D at $V_B = -0.25$ V and B=13 T spanning zero to full transmission of a single IQH edge mode. Inset: applied potential ϕ_{ext}, as determined by electrostatic simulations, across the N-W boundary at the points marked I and II in the main panel. $E_V/E_C \approx 0.4, 1.8$ for I and II respectively. **(b)** Two-terminal differential conductance dI/dV_{SD} measured across the QPC. Data are plotted as a function of V_{SD} along the white contour in panel a, parameterized by $\Delta V = V_{NS} - V_{EW}$. Diamond-shaped conductance peaks are indicative of Coulomb blockade, consistent with resonant transmission of edge modes through a localized state at the center of the QPC, as depicted in the inset. **(c)** dI/dV_{SD} along the black contour in panel a. Resonant reflection is observed, consistent with backscattering of edge state through the localized state, depicted in the inset. **(d)** Zero-bias traces of (b) and (c) illustrate that the resonant transmission and resonant reflection regimes evolve from fractional plateaus at 1/3 and 2/3 respectively as $\Delta V = V_{NS} - V_{EW}$ is increased.

$G_D \equiv I/V_D$ (see Appendix B). In the integer quantum Hall (IQH) regime this quantity gives a direct measure of the number of edge modes N_{qpc} transmitted across the device such that $G_D = N_{qpc}e^2/h$[72, 22].

Fig. 3.11a shows G_D measured over a large range of $V_N = V_S = V_{NS}$ and $V_E = V_W = V_{EW}$ at B=13T and $T = 300\,\mathrm{mK}$ with $\nu_{EW} \leq 0$. The plot is centered around the transition between $G_D = 0$ and $G_D = e^2/h$. The lower left of the plot corresponds to full transmission of the outermost integer quantum Hall edge mode, while lower right corresponds to full pinch-off. The bulk filling factor varies from $\nu_{EW} = 0$ at $V_{EW} = 0.5$ to $\nu_{EW} = -2$ at $V_{EW} = -2.5V$. Despite the range of bulk filling factors spanned in Fig. 3.11a, G_D varies only from 0 to e^2/h indicating that only the outermost integer quantum Hall edge mode is transmitted across the device.

Tuning the gate voltages from upper left to lower right in Fig. 3.11a, corresponding to lines of constant $V_{NS} + V_{EW}$, leaves the applied potential in the middle of the QPC constant. Naively, we expect G_D to also remain constant; however, we observe intricate structure to the measured conductance characterized by the emergence of sharp conductance peaks and dips at the plateau transition. These features are tuned both by the sum and difference of V_{NS} and V_{EW}.

We attribute this structure to the reconstruction of the saddle point potential due to electron-electron interactions. The inset to Fig. 3.11a shows finite-element simulations of the applied electrostatic potential across the boundary between N and W regions, with the gate voltages set to the values given at the points labelled I and II in Fig. 1a. Within our simulations, E_V/E_C can be tuned by more than a factor of four between points I and II, significantly changing the sharpness of the confinement. It is natural to attribute the resonant structure to the effect of this variable; evidently, transmission across the device is highly sensitive to the sharpness of the potential at the the saddle point.

A notable feature of the data in Fig. 3.11a is the approximate reflection symme-

try across the expected line of $G_D = \frac{1}{2}e^2/h$ that relates the two marked trajectories. Figs. 3.11b and c show the differential conductance across the quantum point contact, dI/dV_{SD}, plotted as a function of the source-drain voltage V_{SD} as well as the coordinate $\Delta V = V_{NS} - V_{EW}$ parameterizing the contours shown in Fig. 3.11a. Along the white contour the junction is nearly pinched off, with conductance dropping to zero between high conductance peaks. Nonlinear conductance in this regime shows diamond structure typical of transport across a Coulomb blockaded quantum dot, with charging energies as large as 1 meV. This is consistent with a scenario where resonant transmission through a dot, located at the QPC center, allows charge transport between two otherwise fully-reflected edge states in the E and W regions. This scenario is illustrated schematically in the inset to Fig. 3.11b.

Along the dashed black arrow in Fig. 3.11a, nonlinear conductance shows an almost identical diamond structure, except this time with the on-resonance condition corresponding to a decrease in conductance (Fig. 3.11c). This is again consistent with a Coulomb blockaded quantum dot in the QPC, but one whose effect on transport is to allow backscattering between two otherwise fully-transmitted edge states (see Fig. 3.11c, inset).

In both scenarios, as ΔV is increased, or equivalently, as the potential sharpness is increased, the level spacing of the quantum dot increases. This is consistent with the size of the quantum dot decreasing with increasing ΔV, either making the quantum mechanical level spacing smaller, or simply decreasing the island capacitance leading to an increase in the charging energy. Additionally, in Figs. 3.11b and c, the stability of the Coulomb diamonds decreases with ΔV, eventually giving rise to fractional plateaus at $G_D = \frac{1}{3}e^2/h$ and $G_D = \frac{2}{3}e^2/h$. This is highlighted in Fig. 3.11d which plots zero-bias data extracted from Figs. 3.11b and c.

The existence of a quantum dot is not naïvely expected in a quantum point con-

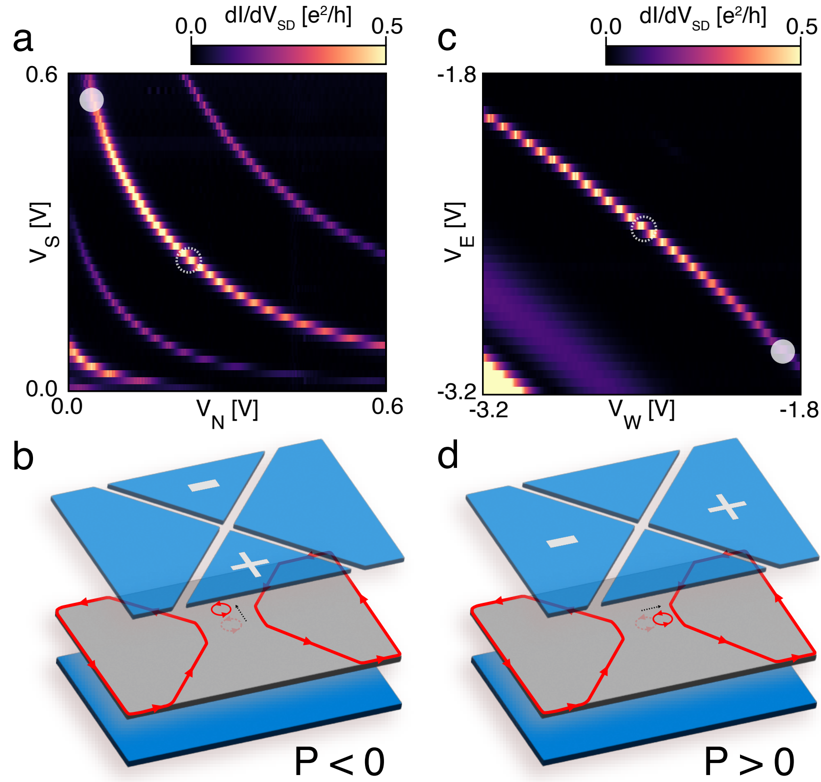

Figure 3.12: **Quantum dot position and polarizability.** **(a)** dI/dV_{SD} at $V_{SD} = 0$ across several Coulomb blockade peaks, plotted as a function of V_N and V_S with other voltages held constant. Near $V_N = V_S$, $dV_S/dV_N \approx -1$ indicating that the dot is equidistant from the N and S gates. The peak follows a contour of positive curvature, indicating the dot is repelled by positive V_N or V_S. **(b)** Cartoon schematic demonstrating a negative quantum dot polarizability as measured in panel a. Here the trapped charge moves in the opposite direction as the applied electric dipole moment. **(c)** The same, but plotted in the (V_W, V_E) plane. Again, $dV_E/dV_W \approx -1$ indicates that the dot is equidistant from the E and W gates at zero detuning. The curvature is negative, opposite to that in the (V_N, V_S) plane. **(d)** Cartoon schematic demonstrating a positive quantum dot polarizability as measured in panel c. Here the trapped charge moves along the applied electric dipole moment. The opposite sign of polarizability along orthogonal directions for the same Coulomb blockade peak indicates the localized charge tracks the equipotentials of the gate-defined saddle point.

tact where the unscreened electrostatic potential realizes a saddle point. The question thus arises as to whether such behavior can arise intrinsically, or if electron confinement might arise from the presence of uncontrolled impurity potentials near the quantum point contact. To address this question, we use the four-quadrant gate geometry [26] to determine both the position of the localized charge and its polarizability within the 2D plane. Fig. 3.12a shows several representative Coulomb blockade peaks as function of V_N and V_S with all other gate voltages constant. The Coulomb peaks follow the condition $C_N\mathrm{d}V_N + C_S\mathrm{d}V_S = 0$, where C_N and C_S are the capacitances to the N and S gates, respectively. The ratio of these capacitances may be inferred from the slope of the Coulomb peak trajectory in the (V_N, V_S) plane, $\frac{\mathrm{d}V_S}{\mathrm{d}V_N} = -\frac{C_N}{C_S}$. When $V_N = V_S$, we find that $C_N/C_S \approx 1$, implying that the dot is equidistant from the two gates. The curvature of the peak trajectory, meanwhile, reveals how the capacitances are changed by the motion of the dot. Taking $C_N = C_S$, the curvature is defined by the expression $\frac{\mathrm{d}^2V_S}{\mathrm{d}V_N^2} = -\frac{1}{C_S}(\frac{dC_N}{dV_N} - \frac{dC_S}{dV_N})$. In Fig. 2a, the curvature is observed to be positive, implying $\frac{dC_N}{dV_N} < \frac{dC_S}{dV_N}$. Since $C_{N/S}$ is inversely proportional to the distance between the gate and dot, this implies that a positive bias on V_N repels the dot from the N gate, as schematically illustrated in Fig. 3.12b. This behavior is consistent with a charge trapped at an electrostatic *minimum* in the N/S direction.

Analogous measurements as a function of V_E and V_W are shown in Fig. 3.12c. Again, for $V_E = V_W$, $C_E/C_W \approx 1$, indicating the dot is equidistant from the E and W gates. However, the curvature of the peak trajectories in Fig. 3.12c are opposite in sign from those in Fig. 3.12a. This behavior is consistent with a particle trapped in an electrostatic *maximum* along the E/W direction, as illustrated in Fig. 3.12d. Taken together, these measurements show that the quantum dot is centered at an electrostatic saddle point.

The Coulomb blockaded resonant structure is fairly ubiquitous in this device. Fig. 3.13 presents a series of several resonances which exhibit Coulomb blockade on the electron

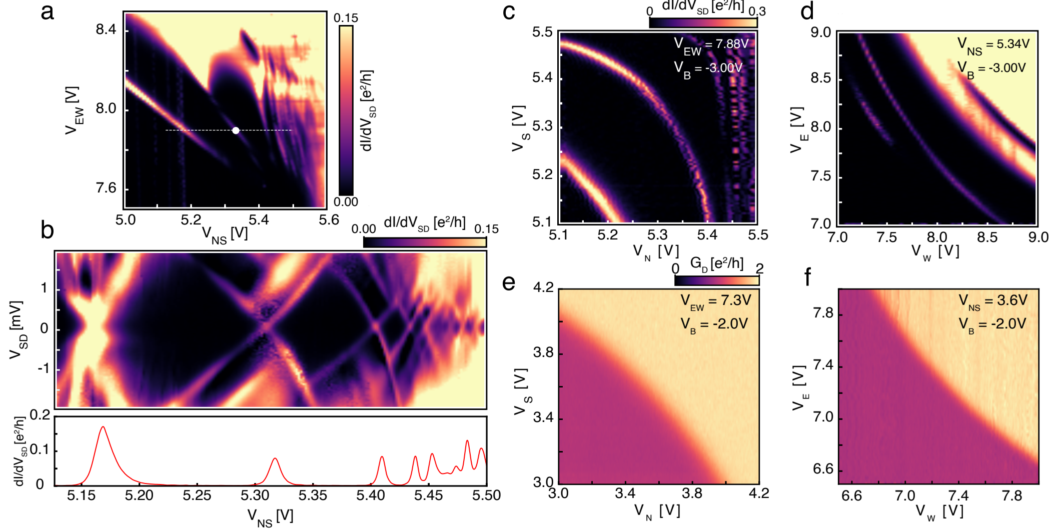

Figure 3.13: **Coulomb blockaded resonances on the electron side.** All data in this figure was taken at B = 9T and T = 20mK. **(a)** Two terminal conductance across the device plotted against V_{NS} and V_{EW}. **(b)** Differential conductance versus source-drain bias plotted along the white dashed line in (a) as well as the corresponding zero-bias line cut. Along the white dashed line $\nu_{EW} = 3$ and $\nu_{NS} = 0$. **(c-d)** Two terminal conductance plotted against $V_{N(W)}$ and $V_{S(E)}$ for the Coulomb blockaded resonances marked by the white dashed line in (a). The primary resonance shown in (d) is demarcated by the white dot in (a). **(e-f)** Diagonal conductance across the device plotted against $V_{N(W)}$ and $V_{S(E)}$ for the transmission step between $G_D = 1$, and $G_D = 2$.

side of the device at 9T and 20mK. Fig. 3.13a shows the resonances in the (V_{NS}, V_{EW}) plane, where $\nu_{EW} \sim 3$ and $\nu_{NS} \sim 0$. The chemical potential of the quantum dot is modulated directly with the N/S gates as V_{NS} is swept along the dashed white line in Fig. 3.13a. Fig. 3.13b shows the differential conductance as a function of V_{NS} and V_{SD} along this V_{NS} trajectory along with the zero-bias cut.

The sharp peaks in Fig. 3.13b have some finite curvature in the (V_{SD}, V_{NS}) plane. Since the slope here is a direct measure of $-C_{NS}/C_{\Sigma}$, where C_{Σ} is the total capacitance of the dot, this indicates that as V_{NS} is increased, the capacitance of the N/S gates to the dot is decreasing relative to C_{Σ}. This is consistent with the dot being squeezed in the N/S direction as V_{NS} is increased. This can be further corroborated by the observation that

as V_{NS} is increased in Fig. 3.13a, the slope of successive resonances decreases, indicating a decreased sensitivity to modulations in V_{NS} – i.e., $C_{EW} > C_{NS}$ as V_{NS} increases. Additionally, Fig. 3.13c-d shows a representative resonance as as function of V_N vs. V_S as well as V_E vs. V_W. Much like the analysis in the main text (Fig. 2), when $V_N = V_S$ or $V_E = V_W$, the slope in the V_N/V_S plane or the (V_E, V_W) plane is near -1, indicating the dot is roughly centered in the QPC.

The behavior of a monotonic transition in G_D as a function of V_N vs. V_S and V_E vs. V_W can be seen in Fig. 3.13e-f. It has been well established that monotonic steps in conductance at a quantum Hall QPC can be described by the scattering of electrons in a magnetic field at a saddle point potential [92]. Qualitatively, the behavior of the monotonic transmission step, and the Coulomb blockaded resonances in 3.13c-d are similar; the monotonic transmission step and the resonance both have the same curvature in the (V_N, V_S) or (V_E, V_W) plane. The similarity between the behavior of the quantum dot and the delocalized edge mode supports the idea that the charge in the dot localized precisely at the saddle point. This is a surprising result given that a saddle point potential does not support localized states even in a magnetic field [93, 92].

These obsevations can be understood by considering the effects of the Coulomb interaction. Generally, edge state reconstruction may lead to non-monotonic density profiles along a smooth potential step [78, 94]. Along the translation-invariant electrostatic edge between two quantum Hall phases, the resulting electronic density retains the spatial symmetry of the underlying potential, resulting in formation of a series of strips at the boundary between the two phases. In a more complex geometry such as the QPC potential studied here, the same mechanism can favor the formation of more complicated structures that still maintain the 180°-rotation symmetry of the underlying potential, such as an isolated dot of nonzero density at the center of the QPC.

To evaluate the plausibility of a reconstruction-induced quantum dot we use a self-

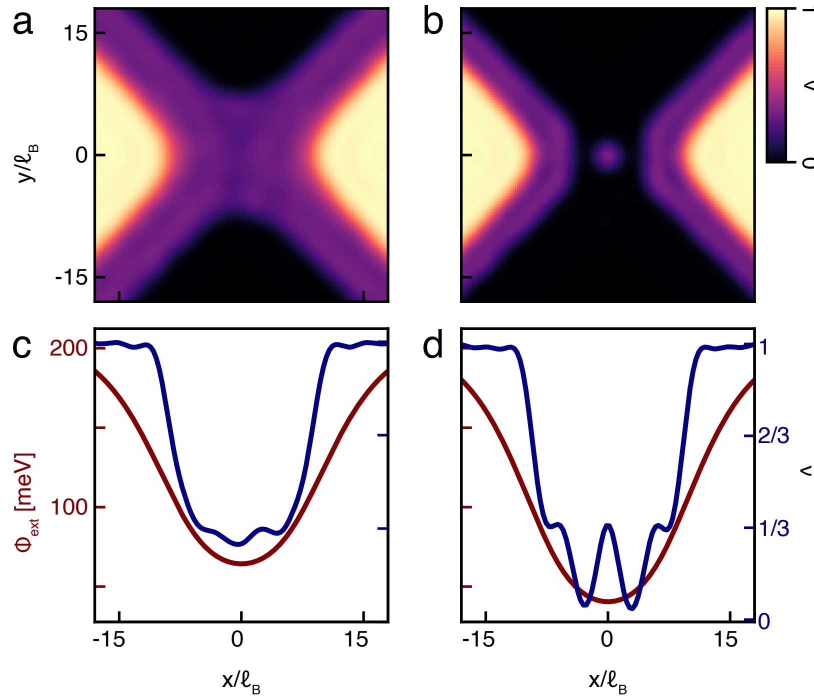

Figure 3.14: **Thomas-Fermi simulations.** **(a)** ν calculated for $B = 13T$ and $E_V/E_C = 0.44$. The continuous strip of $\nu = \frac{1}{3}$ corresponds to transmission of a single e/3 mode, as is observed at point I in Fig. 3.11a. **(b)** ν calculated for $E_V/E_C = 0.49$. For this range of parameters, a small island of $\nu = \frac{1}{3}$ forms at the center of the QPC, separated by depletion regions with $\nu = 0$ from the E and W regions consistent with the Coulomb blockade observed at point II in Fig. 3.11. **(c)** The unscreened potential Φ_{ext} induced externally by the applied gate voltages compared with the reconstructed carrier density ν as a function of x with $y = 0$ for $E_V/E_C = 0.44$ **(d)** Φ_{ext} and ν for $E_V/E_C = 0.49$.

consistent Thomas-Fermi model to calculate the reconstructed density within the QPC. Our calculations account for the density-dependent chemical potential within a partially-filled LL extracted from thermodynamic experiments[21], as well as a realistic device geometry (for details of the calculation see [26, 28]). Fig. 3.14a-b shows the calculated density for $\nu_{EW} = 1$ and $\nu_{NS} = 0$. For the softest potential, in panel a, an intermediate side-strip of fractional filling $\nu = 1/3$ is observed at each boundary between $\nu = 0$ and $\nu = 1$. As E_V/E_C increases, reconstruction becomes less favorable, and an isolated island of filling factor $\nu = 1/3$ spontaneously forms in the center of the junction. Crucially, this island is isolated from the surrounding regions of non-zero density by depletion regions with $\nu \approx 0$. In a transport experiment, these regions may form tunnel barriers between the dot and the reservoirs on either side.

Both regimes of reconstruction correspond directly to observations in Fig. 3.11. At point I along the dashed white line, where $\Delta V = V_{NS} - V_{EW} = 1V$ and the applied potential is thus the softest, we observe fractionally-quantized conductance, $G_D = 1/3$, corresponding to transmission of a single fractional edge mode, in agreement with Fig. 3.14a. Additional evidence for the existence of incompressible strips at fractional filling factors within the QPC, maintained over a wide array of electrostatic configurations where $E_V < E_C$, is given in Fig. 3.17, despite the bulk being set to $\nu = -1$. As ΔV is increased to $\Delta V \sim 2.5V$, Coulomb peaks appear corresponding to the existence of a quantum dot as in Fig. 3.14b. Simulations show that the size of the quantum dot shrinks with further increase of ΔV, while the reflected edge mode still maintains strips of $\nu = 1/3$ away from the QPC, leading to an increase in the level spacing as observed in Fig. 3.11b-d. At sufficiently large ΔV, reconstruction should no longer be favorable anywhere within the device, and one is expected to recover the sharp-edge limit with a single chiral edge mode for a bulk $\nu = 1$ quantum Hall state. This is observed in the Thomas-Fermi calculations, see Fig. 3.15. Data from a second, identical device shows resonant structure

for $E_V/E_C < 2.2$ but a single monotonic step in G_D for $E_V/E_C > 2.2$, see Fig. C.2. Evidently, for appropriate electrostatic conditions the non-reconstructed limit can be recovered in experiment even for gate defined edges. This becomes highly valuable experimentally, as having a distinct signature of the presence of reconstruction in simple DC transport and its removal as sufficiently high values of E_V make doing experiments in the unreconstructed limit more accessible.

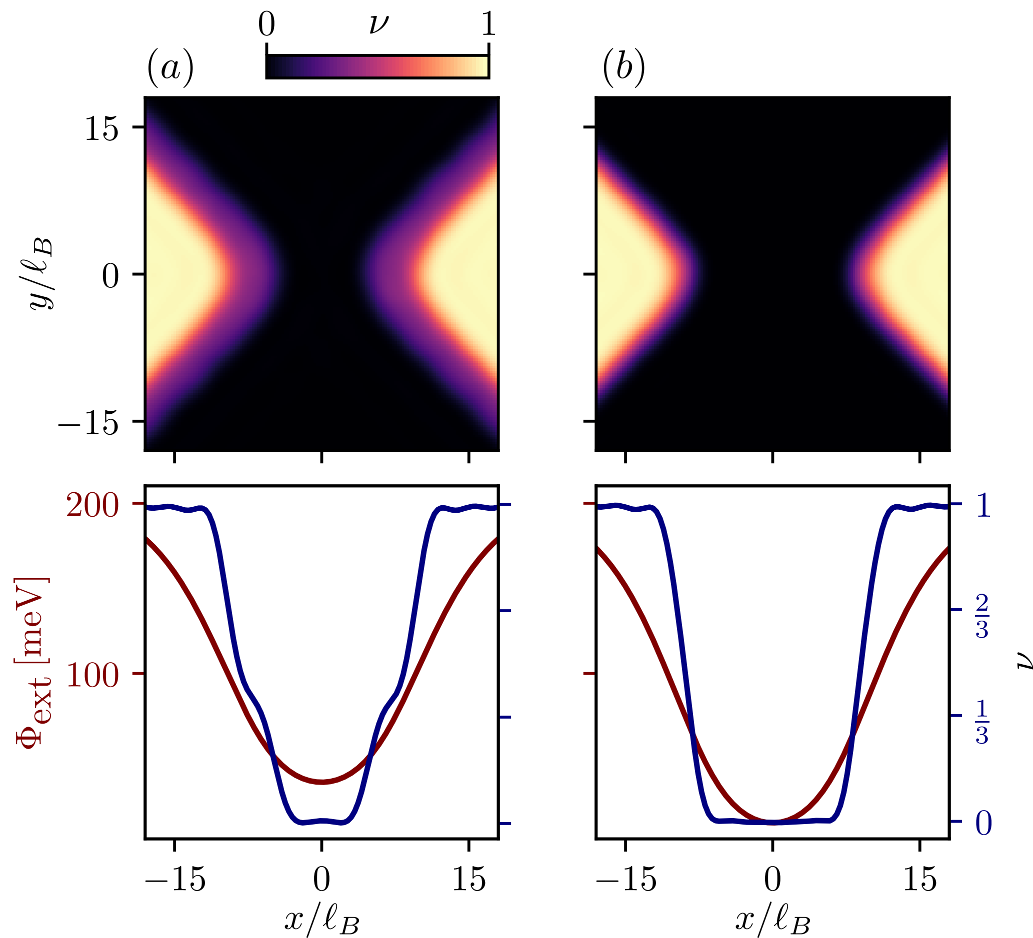

Figure 3.15: **Extended reconstructed electron density profiles in a QPC geometry in the fractional regime**. (a-b) Fractional reconstruction in an integer bulk filling ($\nu = 1$) with $E_C = 46.4$ meV in the regime where the confining potential is sharper than presented in main text Fig. 3a. **(a)** With $E_V/E_C = 0.50$, the $\nu = \frac{1}{3}$ island disappears and the $\nu = \frac{1}{3}$ strips become narrower. **(b)** With $E_V/E_C = 0.57$, the $\nu = \frac{1}{3}$ strips disappear completely.

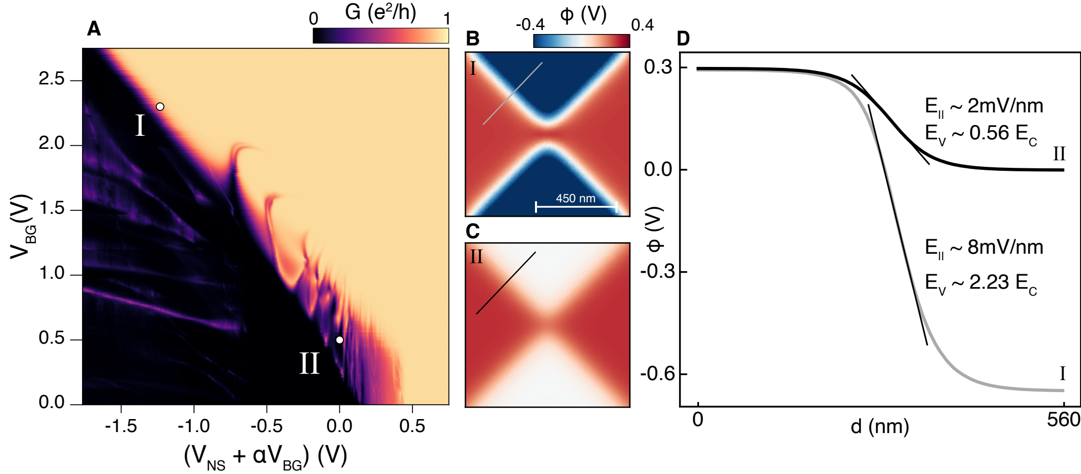

Figure 3.16: **Signatures of reconstruction in G between $\nu = 1$ edge modes.** **(a)** The conductance measured across the QPC with both the East and West regions in $\nu = 1$ at B = 8T. The East and West gate voltages are swept in the opposition direction of V_{BG} along the y axis, through the range $V_{\mathrm{EW}} \in (0.6V, -2.191V)$, to maintain a fixed filling factor while varying the voltage difference and thereby the potential sharpness. **(b)** The simulated electric potential at the monolayer, corresponding to the operating point I. **(c)** Same as (b) but at the operating point II, where the potential is much softer. **(d)** Simulated potential along the contours marked in grey and black in panels B and C, respectively. The softness is quantified by the maximum magnitude of the in-plane confining electric field, $E_{\|}$ (*i.e.* simply the gradient of the potential normal to the boundary between the N(/S) and E(/W) regions).

More interestingly, within our simulations the quantum dot is composed of an island at fractional filling. This suggests that single fractionally charged quasiparticles can be localized even in a geometry which forbids trapping single particles in the absence of Coulomb interactions. Additionally, in light of our simulations the highly symmetric nature of the resonant reflected features observed in Fig. 3.11a may likely be interpreted as the particle-hole conjugate to the scenario presented in Fig. 3.14b. Future experiments, for example measuring the shot noise across the QPC, may give direct evidence for the trapping of fractional quasiparticles in the saddle-point quanutm dot.

In conclusion, we have shown that QPCs in the quantum Hall regime can host Coulomb blockade physics even in the absence of an applied confining potential or dis-

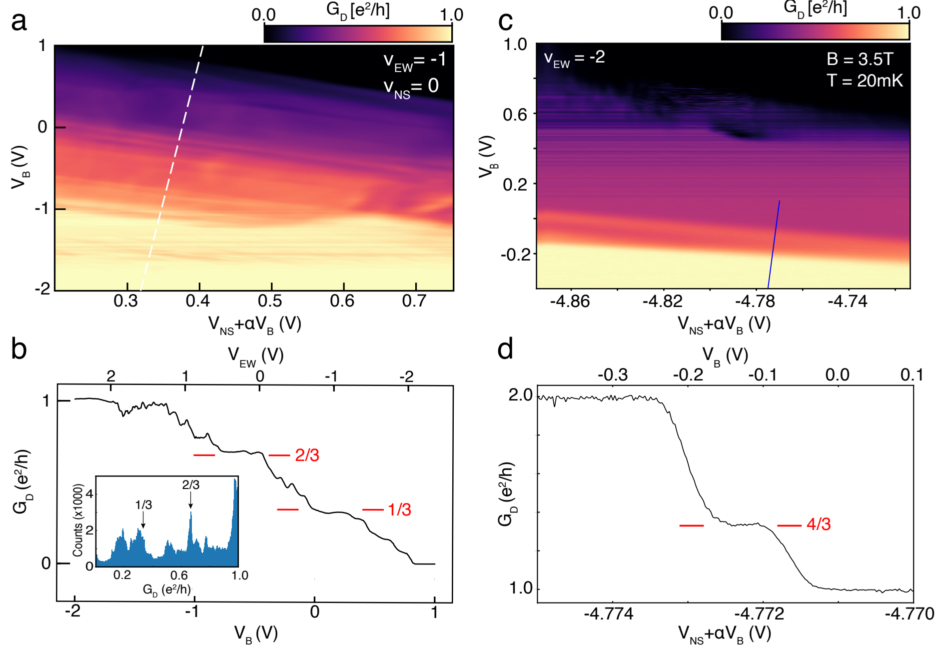

Figure 3.17: **Evidence for fractional edge modes at the boundary of a bulk integer state: (a)** G_D at a fixed $\nu_{EW} = -1$ versus $V_{NS} + \alpha V_B$ and V_B. Here V_{NS} is swept in a range dependent on V_B such that the range $V_{NS} + \alpha V_B$ is kept fixed. Additionally, as V_B is swept, V_{EW} is swept concomitantly to keep the bulk filling factor, set by $V_{EW} + \alpha V_B$, fixed at $\nu = -1$, but varying $V_{EW} - V_B$. The x-axis range corresponds to the full width of the $\nu = 0$ plateau. **(b)** The diagonal conductance map of the $\nu_{EW} = -1$ state at B=13T presented in panel (a) shows a number of features between $G_D = 1$ and $G_D = 0$. The statistical frequency of conductance values across the entire plot, reveals a number of sharp peaks corresponding to conductance plateaus between 0 and 1. The most prominent occurs at $G_D = 2/3$. A broader peak is observed near 1/3, though the quantization is less exact, and several further sharp peaks are seen centered near 0.2, 0.5, and 0.8. The origin of these peaks is unknown, and may be due to a more complicated reconstructed edge structure than is accounted for by any model discussed in this work. **(c)** Diagonal conductance map with the E/W regions in a fixed filling factor $\nu_{EW} = -2$ and N/S regions entirely within the $\nu_{NS} = 0$ plateau. On the y-axis, the bottom gate and E/W gates are swept in opposite directions to vary $(V_B - V_{EW})$ while keeping $\nu_{EW} = -2$ fixed. On the x-axis, the N/S gates are swept across the entire $\nu = 0$ plateau. **(d)** Line cut given in (c) showing two integer plateaus and an intermediate fractional plateau near $G_D = 1.33$ demarcated by the red lines. In both (a) and (b) a correcting scale factor of 0.95 is applied uniformly to G_D to correct for a parallel conduction channel created in our device due to fringe doping from the Si gate, leading to over-quantized plateaus. Here only one $e/3$ edge mode is observed, in contrast to the data at B = 13T where two $e/3$ modes are observed. This is similar to previous reports in GaAs [87], however, the reason why one plateau is favored at low field compared to $B = 13T$ remains unclear.

order effects, resulting from the spontaneous formation of a quantum dot due to the interplay between the applied gate potential and interparticle Coulomb interactions. The discrepancy between the applied electrostatic potential and the total potential at the QPC provides direct evidence for edge state reconstruction. By characterizing edge-state reconstruction in comparatively simple direct current transport measurements, moreover, we show that these effects may be identified and mitigated in experiments to probe fractional statistics in graphene based devices using QPCs[22, 26, 29] and Fabry-Perot interferometers[24, 23, 57, 95].

3.8 Demonstration of Universal Chiral Luttinger Liquid Behavior at $\nu = 1/3$ Edge in the Sharp Edge Limit

The Landau theory of Fermi liquids provides a near-ubiquitous description of interacting fermion systems. One exception is provided when electrons are confined to one dimension, where arbitrarily weak interactions favor a distinct phase known as the Tomonaga-Luttinger Liquid[81, 96, 37, 97]. In this phase, the low-energy collective excitations are orthogonal to the single-electron operators from which they are microscopically constructed. This 'orthogonality catastrophe' manifests experimentally as a power-law suppression of the electron tunneling density of states, $N(E) \propto (E - E_{\mathrm{F}})^{1/g-1}$, at the Fermi energy E_{F}, despite the fact that the system remains conductive. The power law is characterized by an exponent g known as the Luttinger parameter, which depends continuously on the nature and strength of the interparticle interactions[98]. Experimentally, Luttinger liquid behavior can manifest through a non-Ohmic current-voltage relation $I(V) \propto V^{1/g}$, as observed, for example, in ropes of single-walled carbon

nanotubes[99, 100].

An alternative means of creating a one-dimensional wire is at the boundary of a topologically ordered phase, as occurs in the fractional quantum Hall (FQH) effect[101]. Here, the right- and left- moving modes are physically separated to opposite edges of the two dimensional sample, resulting in a chiral Luttinger liquid in which backscattering is suppressed entirely and the Luttinger parameter g becomes quantized[30]. In this setting, g becomes a fingerprint of the topological order of the enclosed bulk; for example $g = \frac{1}{3}$ for the Laughlin state at Landau level filling $\nu = \frac{1}{3}$[30, 80]. In such a scenario, tunneling of whole electrons into the fractionalized edge of the $\nu = \frac{1}{3}$ state is predicted to exhibit a quadratic scaling $G \propto T^2, V^2$. The quadratic scaling is a direct result of the quantized value of $g = 1/3$, and a central prediction of the theory is that this behavior is universal and independent of microscopic details at sufficiently low temperatures and bias voltages[30].

Experimentally, one of the most successful tests of the chiral Luttinger liquid theory was obtained by studying tunneling between the edge of a two dimensional electron gas (2DEG) hosting a FQH state at $\nu = 1/3$ and a three dimensional electrode grown on the cleaved edge of the semiconductor wafer[85, 37]. While striking power-law behavior was observed over a wide range of bias voltages and temperatures[85], the exponent $1/g \sim 2.7$ was found to vary across samples and within the $\nu = 1/3$ plateau[102, 86]—in disagreement with the predicted quantized exponent $1/g = 3$. This sparked a thorough discussion about the nature of bulk-boundary correspondence and whether or not g is indeed a distinct imprint of the topological order of the bulk [103, 104, 105]. However, the possibility of edge reconstruction was soon identified as a confounding factor that could reconcile the range of observed exponents with the chiral Luttinger liquid theory [106, 89, 107].

In principle, a quantum point contact between integer and fractional quantum Hall

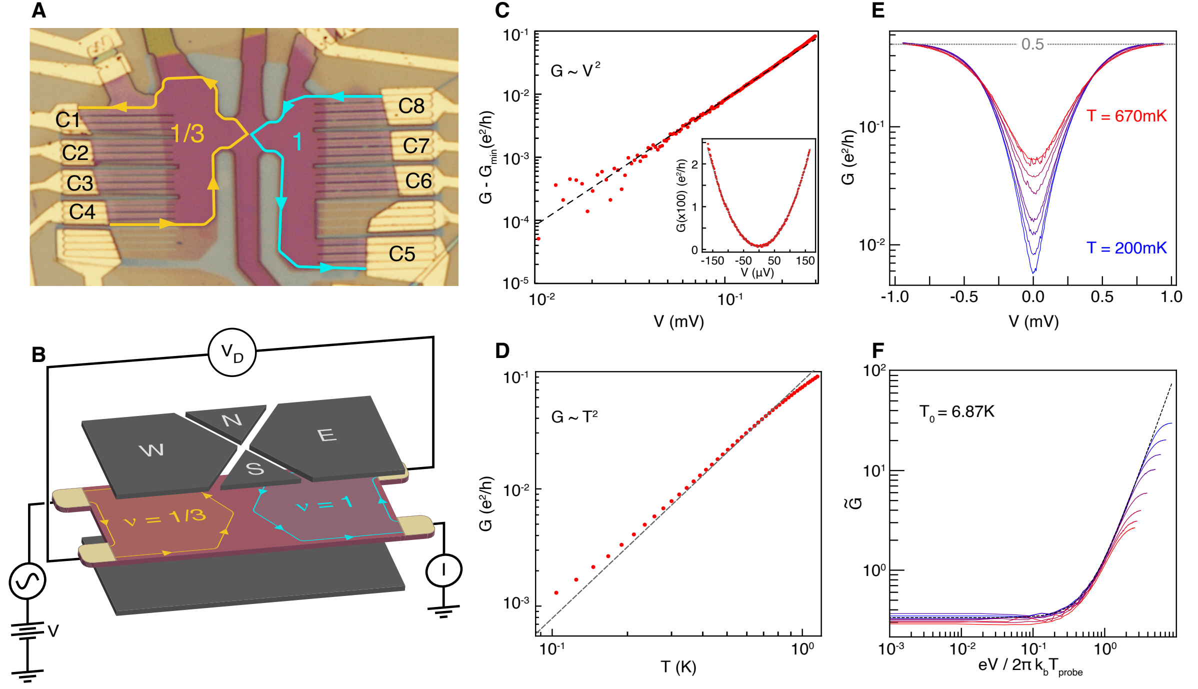

Figure 3.18: **Universal conductance scaling at weak coupling.** **(A)** Optical micrograph of the device with schematic depiction of chiral edge states. **(B)** Device schematic showing the patterned top graphite layer, graphene monolayer, and global bottom graphite gate[108]. The tunneling conductance across the junction is determined from the transmitted current I and diagonal voltage V_D as $G \equiv I/V_D$. **(C)** G measured as function of V at $T_{\text{probe}} = 56\,\text{mK}$, with $V_{\text{NS}} = -2.465V$ and $B = 10$ T. The inset shows a parabolic fit to the low-V regime, giving $T_0 = 9.02 \pm 0.007K$ as defined in Eq. (3.3). The main panel shows $G - G_{\text{min}}$, where $G_{\text{min}} = 7.5 \times 10^{-4} e^2/h$ is the minimum conductance. Fitting a power-law gives an exponent of 2.00 ± 0.06 (Appendix C), where the error represents the standard deviation in the fit parameter. **(D)** G measured at $V = 0$ as a function of temperature at the same gate voltages as panel (c). The dashed line is a plot of the conductance given by the first term of Eq. (3.3), using $T_0 = 9.02 \sim$K. **(E)** Nonlinear differential conductance for T_{probe} =202mK, 245mK, 290mK, 344mK, 450mK, 549mK, 618mK, 666mK at $V_{\text{NS}} = -2.456V$. **(F)** The same data as in panel (e) after scaling G and V as described in the main text. The black dashed line is $\widetilde{G}$ as predicted by Eq. (3.3).

edge states[30, 109, 98, 80, 110, 111, 112] provides a richer test-bed for chiral Luttinger liquid physics. In this geometry, the collective modes of the $\nu = \frac{1}{3}$ and $\nu = 1$ edges may be modeled as chiral bosonic fields ϕ_a and ϕ_b, respectively, coupled by a *single* point scatterer of strength Γ. The low energy physics is described by the Lagrangian

$$\mathcal{L} = \frac{1}{4\pi} \sum_{i=a,b} \partial_x \phi_i (\partial_t - \partial_x) \phi_i + \Gamma \delta(x) \left(\psi_a^\dagger \psi_b + \psi_b^\dagger \psi_a \right) \tag{3.2}$$

where the operators $\psi_a = e^{i\sqrt{3}\phi_a}$ and $\psi_b = e^{i\phi_b}$ remove an electron on the $\nu = 1/3$ and $\nu = 1$ edges, respectively. In Eq. (3.2), the first term describes the gapless bosonic edge modes on either side of the junction, while the second term describes inter-edge tunneling of electrons at the point contact. In the language of the renormalization group, the scaling dimensions of the electron operator $[\psi_b] = 1/2$ while $[\psi_a] = 3/2$ is three times larger, reflecting the topological order of the $\nu = 1/3$ fractional quantum Hall bulk. In order for the corresponding 2D Euclidean action to remain dimensionless, $[\Gamma] = 1 - [\psi_a] - [\psi_b] = -1$, meaning that edge-to-edge tunneling is irrelevant and becomes increasingly less important at low energies. This leads to the remarkable conclusion that no matter how "open" the junction is made—in other words, no matter how large the bare value of Γ is— the conductance will vanish at a sufficiently low temperature and voltage bias[31]. Near this decoupled fixed point, the conductance can be computed within perturbation theory [37], giving

$$G(V,T) = \frac{e^2}{2h} (\frac{2\pi T}{T_0})^2 \left[\frac{1}{3} + (\frac{eV}{2\pi k_b T})^2 + \cdots \right] \tag{3.3}$$

for small temperatures T and voltage bias V. Here the bare tunneling strength is represented by T_0, where for weakly coupled edges $T_0 \propto 1/\Gamma$. In this limit, the power law exponent $1/g - 1 = 2$ describing the T and V dependence provides a direct probe of the bulk topological order.

Quantum point contact experiments in semiconductor quantum wells have indicated power-law behavior near the decoupled fixed point (close to full pinch-off) over a limited temperature range[32, 33]; however, the presence of disorder at the tunnel junction often complicates the physical interpretation [32, 33, 82, 38, 113, 114, 73]. In a more recent experiment [83] focused on the weak quasiparticle backscattering limit, the conductance showed clear characteristics of a Luttinger liquid, but remained quantitatively inconsistent with the predictions of *chiral* Luttinger liquid theory: the measured value of the Luttinger parameter g did not align with predictions for any candidate incompressible ground states at the filling factors studied in Ref. [83]. Interestingly, in our first quantum point contact experiment, we also found non-quantized Luttinger liquid behavior resulting from a reconstructed fractional edge, this was described in the previous sections. It appears that for both quantum point contact and cleaved-edge overgrowth experiments, non-universal effects arising from the detailed structure of experimentally realized edges[78, 115, 111, 116] push the universal scaling regime to energy scales beyond experimental reach.

Prior studies of quantum point contacts have been limited to regimes dominated by resonant tunneling effects, due at least in part to disorder introduced during the fabrication of local split gates[22, 117, 23, 24]. Here, identically to the device described in the previous section, we use anodic oxidation lithography to pattern nanoscale features in graphite gates, which are then incorporated into a van der Waals heterostructure to produce a clean quantum point contact [108]. A micrograph and schematic of our device is shown in Fig. 3.18A-B. 44nm-thick hexagonal boron nitride (hBN) dielectric layers are used as spacers between the monolayer graphene layer and the top and bottom gates. The device architecture features a four-quadrant split gate geometry[108] where independent voltages may be applied to the North, South, East and West top gates (V_{N}, V_{S}, V_{E} and V_{W}, respectively) and a global bottom gate (V_{BG}). With V_{BG} held constant, V_{E} and

V_W fix the filling factors of the East and West regions to 1 and 1/3, respectively, while $V_\mathrm{NS} = V_\mathrm{N} = V_\mathrm{S}$ is used to create a constriction by tuning the filling of the North and South regions to $\nu \leq 0$.

The choice of V_BG controls the 'sharpness' of the potential profile at the constriction, parameterized by the energy scale $E_V \equiv e\frac{\partial V}{\partial x}\ell_b$. Here V, which is defined as the *applied* potential, is purely a function of the applied gate voltages and does not take into account the finite compressibility of the 2DEG at high magnetic field. E_V plays a key role in the physics of fractional quantum Hall edges: when the confinement energy E_V is smaller than the Coulomb energy, the edge may reconstruct [78, 118], introducing additional edge modes which may push the universal tunneling behavior to experimentally inaccessible energy scales. As described in Refs. [108, 119], as well as thoroughly in the previous sections covering our first QPC experiment, the control available in our geometry allows us to access the universal regime of $E_C < E_V$ while maintaining independent control of the bulk filling factor and quantum point contact transparency.

We begin by investigating the 'weak-coupling' regime where $G \ll e^2/h$. This corresponds to the limit of $eV \ll 2\pi k_b T_0$ and $T \ll T_0/2\pi$ represented by Eq. (3.3). We measure $G \equiv I/V_D$ (see Fig. 3.18B), which is a four-terminal measurement of the tunneling conductance [108, 119]. We tune T_0 via V_NS. Fig 3.18C shows G measured as a function of the DC voltage bias, V, at a fixed $T_\mathrm{probe} = 56$mK and $V_\mathrm{NS} = -2.465V$. As seen in the inset, the V-dependence is well fit by a parabola, with a curvature corresponding to $T_0 = 9.02K$ in Eq. (3.3). To assess the quality of the power law fit, we subtract the minimum conductance, G_min and plot $G - G_\mathrm{min}$ on a logarithmic scale (Fig. 3.18C). We find a simple V^2 power law over one order of magnitude in V, corresponding to two orders of magnitude in $G - G_\mathrm{min}$. Specifically, we find an exponent of $2.00 \pm .06$ (Appendix C). While we have not studied the filling factor dependence in detail, a second measurement taken at a different magnetic field and different value of the bulk filling factor within the

$\nu = 1/3$ plateau shows the same exponent(Appendix C).

We next compare experiment with the predicted zero-bias temperature dependence, $G(V = 0, T, T_0)$, of Eq. (3.3). The result for $T_0 = 9.02K$ is shown in Fig. 3.18D. In contrast to the voltage dependence, a T^2 power law is observed only for a limited range of T, between 200mK and 700mK. We attribute deviations at lower temperatures to a decoupling of the electronic temperature from T_{probe}. At high temperatures, deviations are expected as corrections to Eq. (3.3) become important, with significant deviations onsetting for $T > T_0/(4\pi) \approx 750\,\text{mK}$(Appendix C). While the range of the power law behavior in T occurs over a limited range, the observed power law in T is consistent with the more robust power law in V, which is a manifestation of a general scaling relation. Defining $\tilde{G} = 2G \cdot \left(\frac{T_0}{2\pi T}\right)^2 \cdot \frac{h}{e^2}$ and $x = eV/\left(2\pi k_B T\right)$, it follows that $\tilde{G} = 1/3 + x^2 + \cdots$ provides a universal low-energy collapse.

Fig. 3.18E shows G as a function of V for several different temperatures at $V_{\text{NS}} = -2.456V$. The same data, plotted as $\tilde{G}(x)$, is shown in Fig. 3.18F. In these data sets, $T_0 = 6.87K$ is determined by fitting the lowest temperature curve in Fig. 3.18E to Eq. (3.3). For low values of V where universality is expected (Appendix C), the curves collapse onto the universal parabolic curve expected from chiral Luttinger liquid theory.

3.9 Perfect Andreev Scattering of e/3 Quasi-particles at a $\nu = 1/3$ to $\nu = 1$ Point Heterojunction

As seen in Fig. 3.18E, G approaches $\frac{e^2}{2h}$ at high bias. Naively, this is surprising: one might expect that full transmission of the incoming fractional edge mode would cause the conductance to saturate at $G = \frac{e^2}{3h}$. In fact, the observed $G \approx \frac{e^2}{2h}$ can be understood from the peculiar properties of the point contact at strong coupling, defined

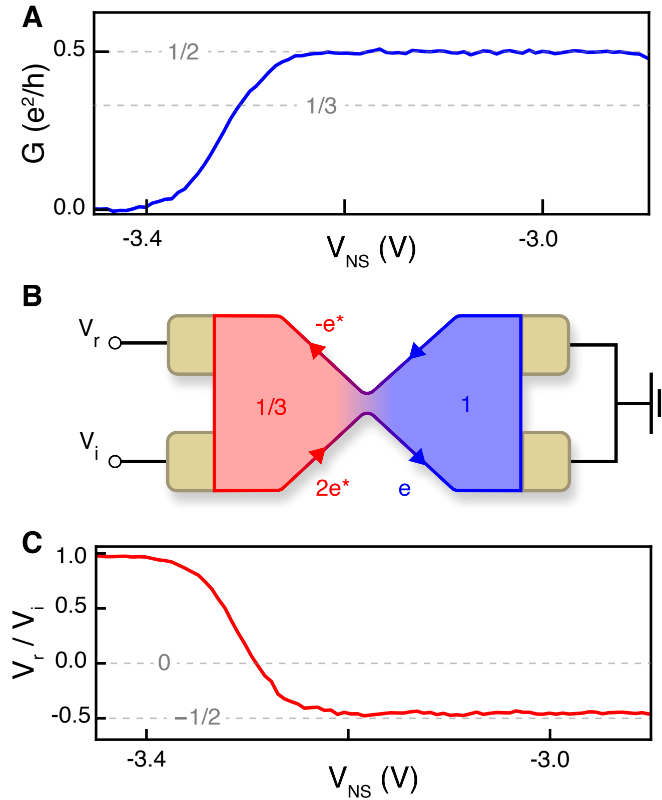

Figure 3.19: **Andreev-like quasiparticle scattering. (A)** G versus V_{NS} taken at $B = 9$T with a finite DC voltage bias of $145\mu V$. Here, V_{BG}=2.0V, V_{E}=-1.460V, and V_{W}=-1.775V to maintain $\nu = 1$ and $\nu = 1/3$ on the 'East' and 'West' sides of the junction respectively. **(B)** Schematic representation of the Andreev scattering process for fractionally charged quasiparticles in the strong coupling limit[112] of a $\nu = 1/3$ to $\nu = 1$ point heterojunction. **(C)** Ratio of the reflected voltage V_{r} to the source voltage V_{i} versus V_{NS}; all other gate voltages are the same as in panel (a).

as $eV \gg k_b T_0$ or $T \gg T_0$. The strong coupling regime is accessed most readily by lowering T_0 (i.e., increasing V_{NS}) at fixed V and T, leading to a plateau in the differential $G \approx \frac{e^2}{2h}$ (Fig. 3.19A).

Microscopically, the excess conductance can be understood by analogy to Andreev scattering at a metal-superconductor interface [112, 111, 120]. In this picture, conduction occurs when a pair of incident quasiparticles, each with charge $e^* = -e/3$, is transmuted into a single electron on the $\nu = 1$ side through the simultaneous retro-reflection of a

charge-$e/3$ quasi-*hole* into the downstream chiral edge state (see Fig. 3.19B). This process leads to the observed nearly-quantized increase in G. Moreover, when the Andreev process is the dominant form of charge transfer across the junction, the downstream $\nu = 1/3$ edge hosting the retro-reflected hole is expected to develop a negative chemical potential with magnitude that is one half of the voltage of the incoming edge[121, 112]. Fig. 3.19C shows the measured reflected voltage V_{r} under the same conditions as the G data in Fig.3.19A. The near-quantization of both G and V_r/V_i over the same broad range of junction transparency implies that the described Andreev process completely dominates charge transfer. This contrasts with previous experiments in semiconductor wells[114], where a much smaller effect was observed, likely mediated by resonant scattering.

3.10 Comparison of Tunneling Characteristics of a $\nu = 1/3$ to $\nu = 1$ Heterojunction to an Exactly Solveable Quantum Impurity Model

In our discussion, we have considered only single electron tunneling between edges, parameterized by Γ; however, additional processes such as electron co-tunneling may also contribute, which would be represented by additional operators not included in Eq. (3.2). Renormalization group analyses have shown[80] that as $\Gamma \to 0$ these terms are more irrelevant than Γ. This guarantees that regardless of microscopic details Eq. (3.2) becomes a good approximation to the physical system at sufficiently low energies. This is characteristic of a stable fixed point of the renormalization group, and accounts for the universal scaling behavior demonstrated in Fig. 3.18.

A different result is obtained at strong coupling—formally $\Gamma \to \infty$—which represents an unstable fixed point[112, 122]. At this fixed point the dominant process that transfers

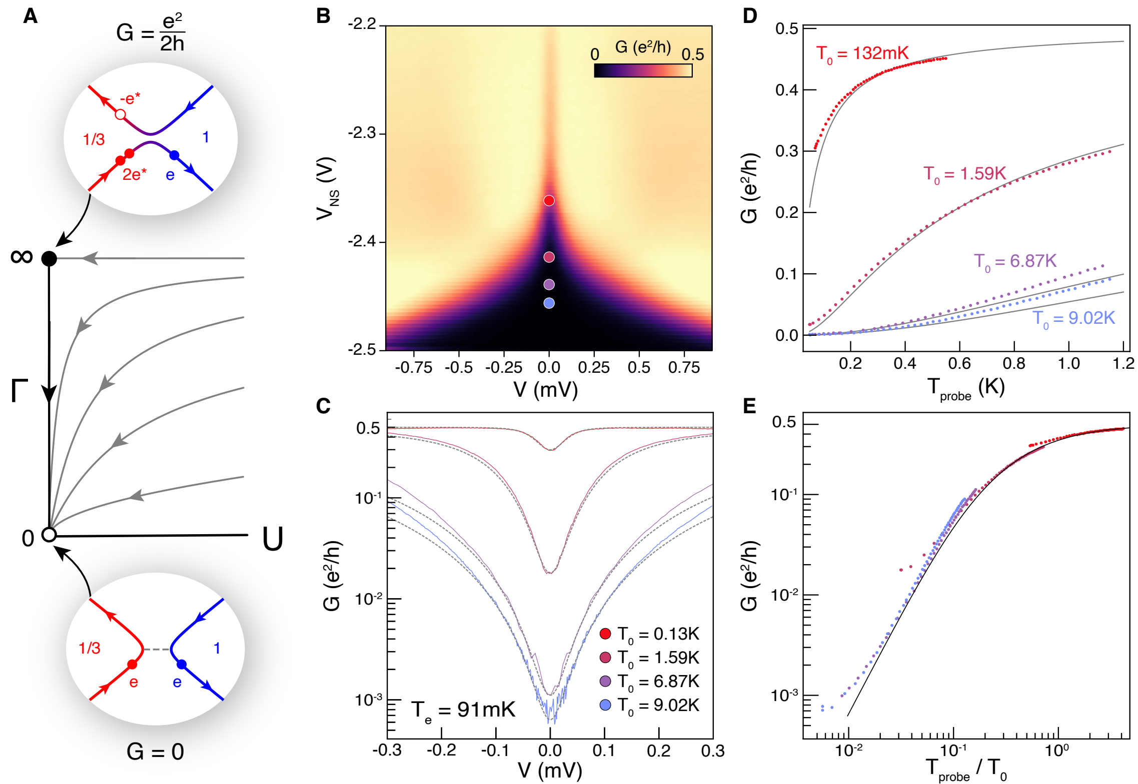

Figure 3.20: **Crossover from weak to strong coupling. (A)** Schematic of renormalization group flow in the Γ-U, where U represents additional perturbations to Eq. (3.2). **(B)** G as a function of the voltage on the North/South gates, V_{NS}, and the DC voltage bias V at $B = 10T$. **(C)** Line cuts of panel (b) at the values of V_{NS} indicated by the colored points. Black dashed lines are plotted using the value of G predicted by Eq. (3.4) where the parameter T_0 is extracted from the low-bias conductance. **(D)** The zero-bias conductance also scales with temperature in agreement with Eq. (3.4) for low energies. While the data deviates from the model at high energies, G nevertheless exceeds $G = \frac{e^2}{3h}$ for $T \gg T_0$, indicating strong coupling at high T. **(E)** The data from panel d, after scaling T by T_0. The curves collapse onto the universal scaling formula Eq. (3.4), shown in black.

charge across the junction is Andreev scattering. However, while other processes vanish when $\Gamma = \infty$—giving $G = \frac{e^2}{2h}$—for any finite value of Γ, G is expected to vanish at low energies as the system flows toward the stable $\Gamma = 0$ fixed point. This is shown schematically in Fig. 3.20A, which depicts a renormalization group flow diagram indicating the trajectory of the conductance as the energy is lowered. In this plot, the y-axis, Γ, represents the coefficient of the operator which transfers an electron between the two edge modes, while the x-axis represents the coefficient 'U' of any operator not explicitly captured in Eq. (3.2). As is seen in the diagram, finite U, expected for realistic heterojunctions would seem incompatible with approaching the strong coupling fixed point. For this reason, the strong coupling limit was previously thought to be practically inaccessible except through highly tuned resonant scattering [123, 121]. While fine-tuned, this limit would arise if the QPC forms an adiabatic constriction in which approximate momentum conservation along the QPC prevents backscattering between the N and S edge [124].

The fact we observe near-perfect Andreev reflection when the junction is highly transmissive suggests the microscopics of the system approach the strong-coupling fixed point with negligible contributions from the additional operators represented by U. When $U = 0$, Eq. (3.2) can be mapped to an integrable 'quantum impurity model' with an exact solution for all values of Γ[31, 122]. The solution provides an expression for G at arbitrary V, T, and T_0,

$$G(V,T) = \frac{e^2}{2h}\int_{-\infty}^{\infty} dE \frac{-(2E+eV)^2}{(2E+eV)^2+(k_bT_0)^2} f'(E) \tag{3.4}$$

where $f(E)$ is the Fermi-Dirac function[122]. Eq. (3.4) provides a universal crossover function which describes the transition between weak and strong coupling, depicted as a single line along the y-axis ($U = 0$) of Fig. 3.20A[111, 112, 122]. The integral reduces to

Eq. (3.3) for $T_0 \to \infty$, corresponding to the weak coupling fixed point, and gives $\frac{e^2}{2h}$ for $T_0 \to 0$ corresponding to strong coupling.

Fig 3.20B shows G as a function of V and V_{NS} at a probe temperature $T_{\mathrm{probe}} = 56\,\mathrm{mK}$. Throughout the plotted range, the high V conductance saturates to approximately $\frac{e^2}{2h}$ as expected for the strong coupling fixed point. Meanwhile a zero-bias dip remains visible for all V_{NS}, indicative of the instability of the point contact to edge decoupling at low energies. To quantify how closely the quantum impurity model describes our system, we compare Eq. (3.4) to our experimental data as a function of V and T, and T_0. In Fig. 3.20C, we plot four curves extracted for different values of V_{NS}. For each curve, T_0 is determined from a fit to the low bias behavior with an appropriate low-energy expansion of Eq. (3.4) (Appendix C). For the largest fit values of T_0, the residual value of G when $V = 0$ can then be used as a primary thermometer—in effect allowing us to correct for a possible lack of equilibration between the electron temperature and the probe thermometer. Using this method, we find $T_{\mathrm{electron}} = 91\,\mathrm{mK}$ for the $T_0 = 9.02K$ trace, in contrast to the measured probe temperature of 56mK. Taking 91 mK as the electron temperature for the remaining data sets in Fig. 3.20C, Eq. (3.4) may then be used to generate V-dependent curves interpolating between weak and strong coupling. These curves are overlaid in black on the experimental data in Fig. 3.20C(Appendix C).

Fig. 3.20D shows $G(V = 0, T)$ plotted as a function of the probe temperature for the same values of V_{NS} as in Fig. 3.20C, along with the results of Eq. (3.4) for the corresponding values of T_0. While Eq. (3.4) does not provide a simple scaling between temperature and voltage as is available at the weak coupling fixed point, for $V = 0$ the conductance can be written as a function of the scaled temperature, T/T_0. Fig. 3.20E shows the $V = 0$ conductance plotted as a function of T/T_0. The four data sets shown in unscaled form in Fig. 3.20E collapse onto different parts of the universal crossover function between weak and strong coupling. Note that for panels D-E, the temperature

is measured on the probe and no corrections are made for disequilibrium between T_{electron} and T_{probe}, leading to systematic deviations between experiment and theory at the lowest temperatures. The collapse of the experimental data onto a single universal curve over nearly two orders of magnitude in T_0 strongly supports the conclusion that our quantum point contact realizes the exactly-solvable Lagrangian of Eq. (3.2) to a high degree of accuracy, and in particular, that tunneling predominantly occurs *via* a single point at the QPC rather than via a number of disorder-induced scattering centers.

3.11 Nearly Adiabatic $\nu = 1/3$ to $\nu = 1$ Heterojunction - Making a Dissipationless, Passive, DC Step-up Transformer

At the strong coupling fixed point the quantum point contact acts as a nearly dissipationless splitter, partitioning current injected on the $\nu = 1$ edge equally between the downstream $\nu = 1/3$ and the upstream $\nu = 1$ edge states[112]. For $\Gamma = \infty$, the partitioning happens with unit probability. In this limit, no entropy is generated and dissipation does not occur, leading to unity power efficiency[121]. This contrasts with the more conventional case of partial transmission of edge modes at a quantum point contact, where fluctuations arising from partition noise lead to dissipation. The dissipationless current splitting property of the strong coupling fixed point allows us to operate our device as a voltage step-up transformer[121, 112]. Fig. 3.21 shows the differential gain, $\mathrm{d}V_o/\mathrm{d}V_i$, where V_i is the input voltage applied to the upstream $\nu = 1$ edge state and V_o is the output voltage measured on the downstream $\nu = 1/3$ edge state with all other contacts grounded. The differential gain is very close the theoretically expected value of 3/2 [121]. Remarkably, because it is built on a purely zero frequency effect, the transformer gain

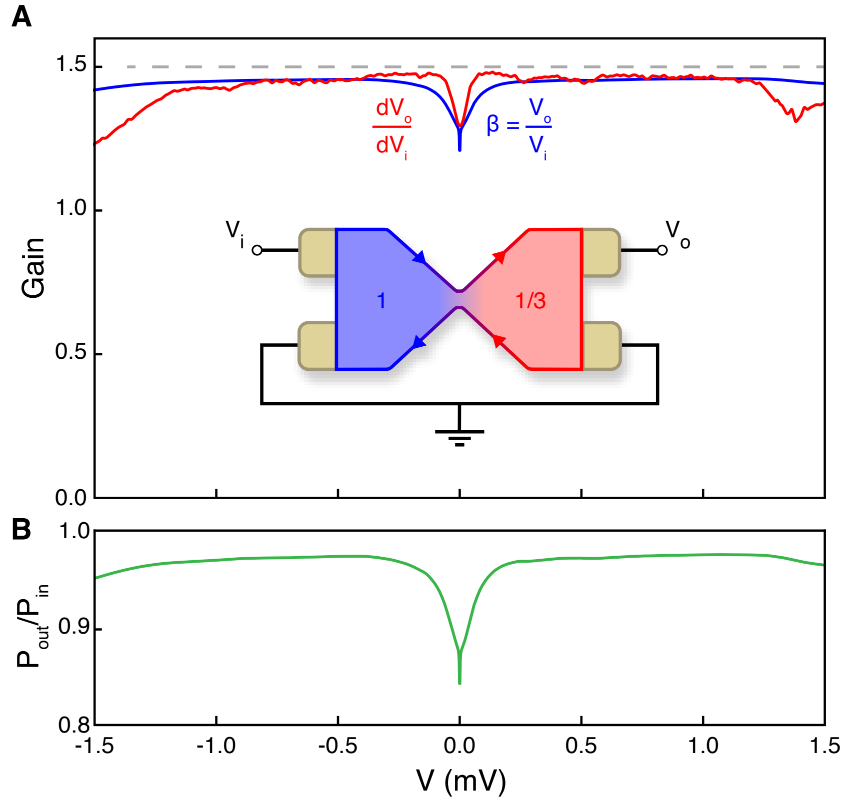

Figure 3.21: **Zero frequency voltage step-up transformer.** **(A)** The differential gain $dV_{\rm o}/dV_{\rm i}$ and resulting integrated DC gain $\beta = V_{\rm o}/V_{\rm i}$, measured in the configuration shown in the inset, with B=9T, $T_{\rm probe}$=48mK, $V_{\rm E}$=-1.460V, $V_{\rm W}$=-1.775V, $V_{\rm NS}$=-3.225V, $V_{\rm BG}$=2.0V. The FQH Andreev scattering process yields an enhancement of the output voltage on the FQH side [121], with the DC gain predicted to reach a value of 1.5 in the dissipationless limit. Experimentally, we find a gain $\beta = 1.46$, despite the nonlinearity at low bias arising from the suppression of the Andreev scattering at low energies. **(B)** The DC power dissipation ratio, calculated from β via $P_{\rm out}/P_{\rm in} = (2\beta/3)^2 - (2\beta/3) + 1$, is plotted versus V, and reaches a maximum value of 97.6% [124].

remains almost the same even in the 'direct current' (DC) limit, as can be seen in the behavior of the integrated gain, V_o/V_i, in comparison to its differential counterpart. The exceptionally high power efficiency, which peaks at 97.6%, is a testament to how closely the experiment realizes the strong-coupling fixed point, and contrasts favorably with zero frequency voltage amplification based on superconductors[125, 126] and bilayer quantum Hall systems[126, 124].

Our observation of universal chiral Luttinger liquid physics at both weak- and strong-coupling directly paves the way for experiments on two dimensional systems where mesoscopic electrostatic control plays a key role in addressing unanswered questions about strong correlations, topological order, and quantum statistics. Examples include even denominator fractional quantum Hall states observed in mono-[14, 127] and bilayer [128, 10, 59] graphene, where taming edge reconstruction in a quantum point contact may allow for unambiguous experimental constraints on the ground state topological order [129, 130, 131, 132, 120]. In addition, the flexibility inherent in anodic oxidation prepatterning will also allow independent tuning of quasiparticle number, edge sharpness, and quantum point contact transparency in interferometer geometries where direct access to quantum statistics are possible[133, 134]. Finally, gate-defined point contacts may allow for precision measurements of order parameters in the recently discovered crystalline graphene superconductors[20, 66, 67].

3.12 Permissions and Attributions

1. The content of this chapter also appears in Ref. [26, 27, 28].

4

Edge State Interferometers in Graphene van der Waals Heterostructures

4.1 Overview

Anyons are two dimensional particles with fractional exchange statistics which emerge as elementary excitations of fractional quantum Hall phases[135, 136, 137, 138]. Abelian anyonic statistics may be accessed in a Fabry-Pérot interferometer through the phase $N\theta_a$ accumulated by a delocalized edge state encircling N localized anyons [139, 140, 141, 142],

where θ_a is twice the exchange phase[143]. Previous experiments on Fabry-Pérot interferometers in semiconductor quantum wells have revealed phase slips indicating the reversible entry and exit of anyons into the interferometer loop at filling factors $\nu = 1/3$ and $\nu = 2/5$[144, 145]. Here, we describe measurements of the anyonic phase in a monolayer graphene based Fabry-Perot interferometer at $\nu = 1/3$. Operating in Aharonov-Bohm dominated regime, we find a preponderance of phase slips with $\theta_a \approx 2\pi/3$, as expected when a single Laughlin quasiparticle enters the interferometer loop. Strikingly, we find that the phase slips occur instantaneously and irreversibly on typical laboratory timescales. We show that this effect is a consequence of slow underlying charge dynamics in our devices, in which single anyons may remain trapped in the interferometer loop out of equilibrium for as long as 10 minutes. The quenching of charge dynamics on practically relevant timescales allows us to separate the dynamical tuning of the interferometer area from changes in the anyon number, denoted as N_{qp}, allowing us to measure the interferometric phase shift of individual single-anyon events as a function of a single gate at fixed magnetic fields. Besides providing a replication experiment giving $\theta_a = 2\pi/3$ at $\nu = 1/3$ in a different two dimensional electron system, our results show that the topological dephasing time represented by unwanted anyon motion can be made practically infinite. This is a necessary condition for the eventual implementation of robust topological quantum information processing at more fragile non-abelian filling factors in graphene heterostructures.

4.2 Introduction

When an abelian anyon is brought along a closed trajectory encircling N_{qp} localized anyons, its wave function accumulates a phase

$$\Phi = 2\pi \frac{e^*}{e} \frac{A_I(B, N_{qp})B}{\hbar} + N_{qp}\theta_a \tag{4.1}$$

where $A_I(B, N_{qp})$ is the area of the loop (which may vary with applied magnetic field and quasiparticle number in a non-trivial way), B is the applied magnetic field, N_{qp} is the number of anyonic quasiparticles localized inside the bulk of the interferometer, and θ_a is the anyonic braiding phase, or twice the exchange phase accrued when two identical anyons are swapped. Quantum Hall Fabry-Perot interferometers (FPIs) exploit the contrast between localized anyonic quasiparticles in the fractional quantum Hall bulk and propagating anyonic quasiparticles of the gapless chiral edge modes to directly observe this phase[139, 140, 141, 142]. In a FPI, delocalized anyonic quasiparticles enter the cavity via a quantum point contact and propagate along the edge to a second quantum point contact; they can then either exit the cavity immediately or complete an integer number of additional circuits before exiting. Trajectories undergoing different numbers of circuits of the sample bulk give an interference contribution to the conductance, $\delta G \propto \cos(\theta)$, which may be measured as a function of B, A_I, or N_{qp}. The clearest signature of anyonic statistics is expected if N_{qp} changes discretely while keeping A_I and B fixed; the resulting jump in θ then gives θ_a directly.

Initial investigations into the behavior of Fabry-Perot interferometers in the quantum Hall regime in GaAs 2DEG systems quickly revealed that the effects of the Coulomb interaction may have a deleterious effect on efforts to observe the anyon phase[146, 147, 142]. In particular, as charges enter the bulk of the interferometer, Coulomb repulsion

may lead to a change in A_I regardless of whether θ_a is finite. If this "bulk-edge coupling" is large, the resulting change in the Aharanov-Bohm (AB) phase obscures the phase-slip θ_a. Recently, a breakthrough in the design of GaAs heterostructures led to the observation of phase shifts that agree quantitatively with expectations for θ_a in the $\nu = 1/3$ state[134, 144, 148, 145]. In these experiments, screening layers are used to suppress the bulk-edge coupling to the point where it plays a quantitative role in the observed interference but does not obscure the contribution of the anyon phase.

Graphene heterostructures are a natural venue in which to extend these results owing to the large energy gaps observed for both Abelian and non-Abelian filling factors as well as the screening provided by nearby graphite gates in standard dual-gated geometries. Indeed, several recent experiments have observed Aharonov-Bohm dominated interference at both integer and fractional fillings[23, 24, 95, 149, 150]. However, measurements of θ_a in graphene have not been previously reported.

4.3 Fabrication and Device Geometry

In this chapter we study a monolayer graphene-based FPI, shown schematically in Fig. 4.1 and Fig. 4.2a. We use anodic-oxidation lithography of a graphite flake combined with van der Waals assembly and standard processing to fabricate a device with six separated regions that can function as independent top gates[26, 27]. The NE/SE and NW/SW gates function as depletion gates to define two quantum point contacts. A plunger gate (P) provides additional control of the interferometer area. The center gate (C) is used to set the filling factor, while a global bottom gate is used to adjust transmission through the quantum point contacts. The additional post heterostructure assembly fabrication steps follow an identical process to that laid out in Appendix B for our quantum point contact devices. The only difference is the structure of the AFM top

gate; an optical image of the device studied here is shown in Fig. 4.1a. This is shown along with the AFM topograph of the cut top gate forming the interferometer and the device heterostructure in Fig. 4.1b-c.

As described in Appendix B, during transfer of the pre-patterned graphite the flake remains contiguous to improve strutural integrity of the microstructure. After the heterostructure is assembled, standard RIE plasma etching is used to fully etch away unwanted regions of the stack and in the process separating the previously connected graphite gates in non-critical regions away from the interferometer. This results in the six individually tunable gate regions, controlled by voltages labeled V_{NE}, V_{SE}, V_{NW}, V_{SW}, V_{CG}, and V_P respectively.

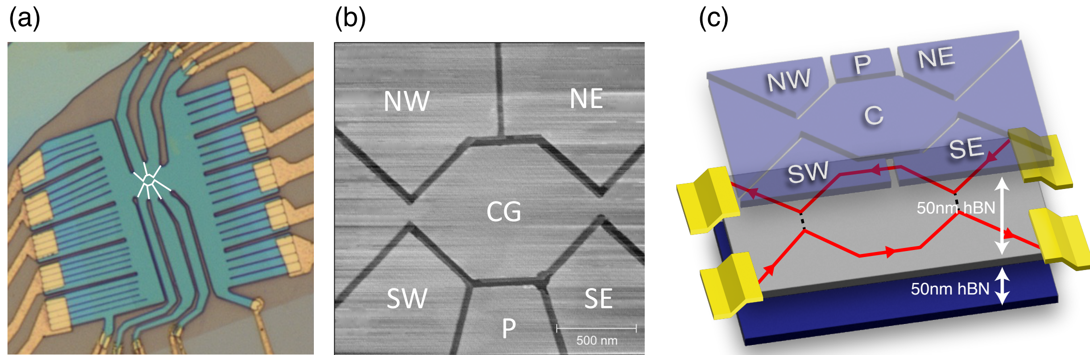

Figure 4.1: (a) Optical micrograph of device discussed in this section. (b) AFM topograph of anodically oxidized graphite gate layer after pick-up with an hBN flake with the various gate regions labeled respectively (NW, SW, NE, SE, and P). (c) Heterostructre layout: the device consists of an AFM cut top gate, which is later separated into six individually addressable gates, a monolayer graphene (middle layer), and a global graphite bottom gate. Each conducting layer is separated by an exfoliated 50nm hBN dielectric. Electrical contacts to the edge of the monolayer are shown in yellow. The edge-state trajectory which creates the Fabry-Pérot interferometer from the applied gate potentials is shown by the red-arrows.

4.4 Interference and Measurement of θ_a at $\nu = 1/3$

Here we report the observation of phase slips associated with the statistical phase of individual anyons within our interferometer loop. As compared to existing literature, the key distinguishing feature of our work is the exceptional stability of individual configurations with fixed N_{qp} localized anyons. In previous works, equilibrium charging dynamics are evident in the interference patterns; in both integer and fractional regimes, interference patterns are typically characterized by a smooth crossover between states of defined charge, where thermal fluctuations N_{qp} lead to dephasing [41, 144]. In contrast, we find that the quasiparticle charge of the interferometer equilibriates only over kilosecond timescales. Our results demonstrate that the topological charge of a graphene-based FPI can be held stable over timescales long enough for any near-term efforts to control single anyons.

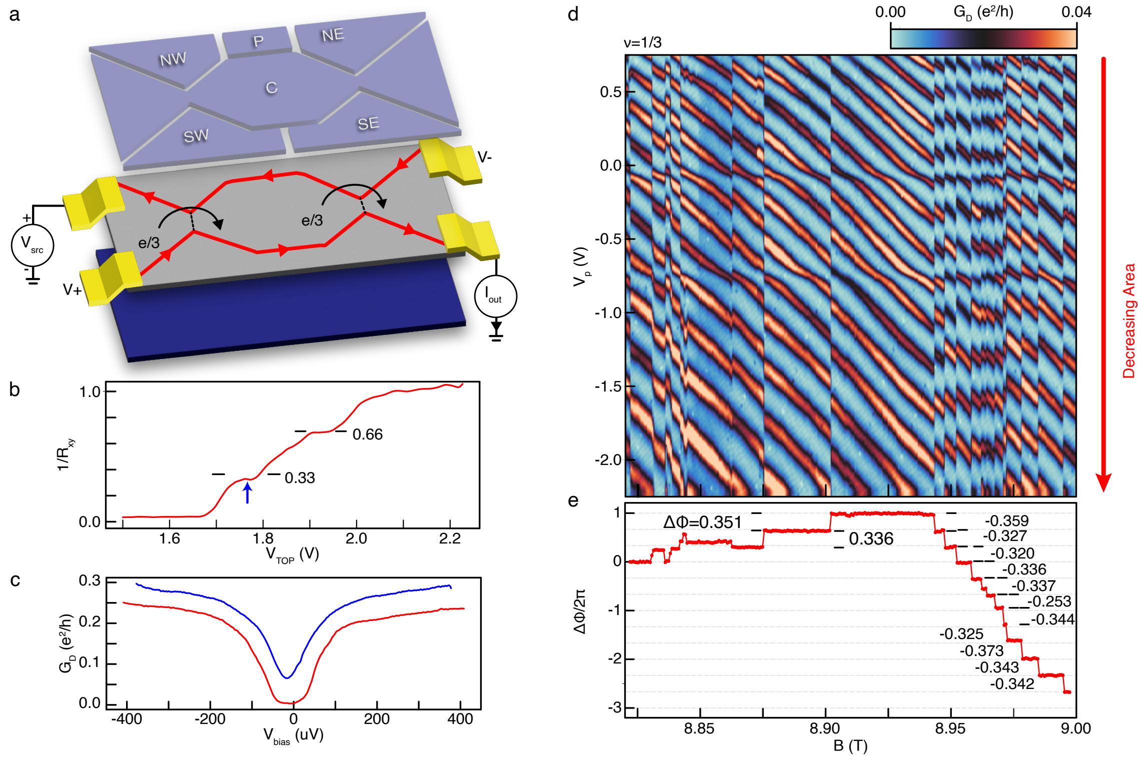

Figure 4.2: **Fabry-Pérot Interference in the $\nu = 1/3$ State (a)** Schematic of our dual-graphite gated monolayer graphene quantum Hall edge state Fabry-Pérot interferometer. The gates defining the interferometer are labeled C, NW, SW, NE, SE and P respectively. Edge states are formed under the center gate and enter the interferometer via two, independently tunable QPCs defined by the NW/SW and NE/SE gates respectively. There is also a global graphite back gate, which we label BG. **(b)** $1/R_{xy}$ measured across the devie as a function of V_{TOP}, all the top gates held at the same voltage. Here $V_{BG} = -1.5V$. **(c)** Conductance through each QPC vs. DC bias, $V_{BG} = -2V$. The blue trace is taken with $V_{NW/SW} = 2.232V$ and $V_{NE/SE} = -4.1V$. The red trace is taken with $V_{NW/SW} = 0.5V$ and $V_{NE/SE} = 2.232$. **(d)** $G_D(e^2/h)$ plotted against B(T) and $V_P(V)$ for $V_{CG} = 2.23V$ and corresponding to the filling indicated by the blue arrow in panel b ($\nu = 1/3$). Periodic oscillations in the conductance indicative of Aharanov-Bohm type interference are observed to be interrupted by sudden jumps in the phase as a result of the tunneling of a single anyon into the bulk of the interferometer. (e) Extracted magnitude of the phase slips observed in (d), $\Delta\Theta = \theta - \theta_{AB}$.

Transport data at B=9T (Fig. 4.2b) shows well developed plateaus corresponding to filling factor 1/3 and 2/3 as the charge density is varied by applying a single voltage to all six top gates. We operate our interferometer within the 1/3 plateau at the

point indicated. To probe the transmission through the interferometer, we measured the diagonal conductance, shown schematically in Fig. 4.2a. The diagonal conductance is defined as $G_D \equiv I_{\mathrm{out}}/(V_+ - V_-)$. To confirm that our experiment is probing chiral edge modes of the 1/3 state, we individually measure the bias dependence of the two quantum point contacts in their partial transmission regime (Fig. 4.2c). Both show strong suppression of the conductance at low bias, as expected for chiral Luttinger liquids where arbitrarily weak impurity potentials lead to strong backscattering at sufficiently low energies[30, 85, 37, 32, 38, 27]. Notably, this behavior is neither expected nor observed in the integer quantum Hall regime, giving us confidence that a single $\nu = 1/3$ edge state is transmitted through our quantum point contacts.

Tuning both QPCs to partial pinch off (see supplementary information), we observe high visibility oscillations in G_D as a function of all gate voltages and applied magnetic field B. A scan using V_P to tune the interferometer area over a range of B that spans the $\nu = 1/3$ plateau is shown in Fig. 4.2d. Lines of constant phase follow a negative slope on this plot, implying that increasing the depletion region, and thus decreasing the interferometer area, requires a concomitant increase in magnetic field to maintain a constant phase. This is a the signature of the Aharonov-Bohm regime[142]. The Aharanov-Bohm behavior can consequently be used to characterize the device parameters. From their periodicity in B of $\Delta B \approx 14 - 18$ mT, we obtain a loop area of $A_I = 0.69 - 0.89\mu\mathrm{m}^2$ from the relation $\frac{e}{3} A_I \Delta B/h = 1$. This is similar to the nominal device area of $0.74 - 0.83\mu\mathrm{m}^2$, whose range is defined by the area of the center gate including or excluding the surrounding gaps between the top gates. By analyzing the period ΔV_{CM} of the interference as the voltage of the 2DEG itself is varied (i.e., the common mode of the transport leads), we obtain the capacitance of the edge state $C_I = e/\Delta V_{CM} = e^2/235\,\mu\mathrm{eV}$. Within the chiral Luttinger liquid theory f the edge, we may then extract the edge velocity via the relation $\frac{hv}{\nu L} = 235\,\mu\mathrm{eV}$. Taking $L = 3300 \pm 110$nm, we obtain $v = 6.2 \times 10^4$ m/s.

The oscillatory conductance depicted in Fig. 4.2d is punctuated by sharp 'slips' in the interference phase. These are effectively instantaneous with respect to the 30-second measurement time of each individual line trace. To extract the value of the individual phase slips, we first Fourier transform G_D with respect to V_P for each value of B and extract the phase of the largest-magnitude peak, which determines $\Phi(B)$. $\Phi(B)$ is expected to contain a smoothly-varying AB part, plus the anyonic part: $\Phi(B) = e^* A_I(B)B/\hbar + N_{qp}\theta_a$. To isolate the latter, we extract the AB contribution Φ_{AB} using a trimmed mean of the phase evolution observed between phase slips. The residual phase, $\Phi_a = \Phi - \Phi_{AB}$, is shown Fig. 4.2d. Excepting three events, the phase exhibits nearly quantized jumps of $|\Delta\Phi|/2\pi = 0.334 \pm 0.027$, where the uncertainty reflects the standard deviation across the 13 phase slips shown in Fig. 4.2e.

We interpret these sharp slips as the sudden entrance of an $e/3$ anyon into the interferometer. The very small deviation of these phase slips from the predicted fractional statistics implies a remarkably low degree of bulk-edge coupling[142]. This may arise if the anyons predominantly enter into localized impurity states a distance $R > d$ from the edge, where $d = 45\,\text{nm}$ is the gate distance. When a charge $e/3$ fills such a state, the compressible edge will partially screen the resulting potential, effectively increasing A_I, an effect known as bulk-edge coupling. Accounting for the electrostatics of a double-gated device, this screening will induce a charge

$$\delta Q_I \approx -\frac{e}{3}\frac{C_I}{\pi\sqrt{\epsilon_{xy}\epsilon_z}L}\exp\left(-\frac{\pi R}{2d}\sqrt{\frac{\epsilon_z}{\epsilon_{xy}}}\right), \tag{4.2}$$

where C_I is the capacitance of the edge state, L is the perimeter, and $\epsilon_{xy} = 6.6$ and $\epsilon_z = 3$ are the dielectric constants of the hexagonal boron nitride dielectric. Taking the measured values of $C_I = e/(235\mu V)$ and L, the bulk-edge coupling contribution to the phase slip is $\delta\theta = 2\pi \times \delta Q_I/e \approx 2\pi \times 0.57\, e^{-R/45\text{nm}}$. For $R > 120\,\text{nm}$, corresponding

to approximately 50% of the area of our interferometer, this correction is less than our experimental uncertainty. Our uncertainty is not dominated by statistical uncertainty, taking the standard deviation of θ inside of each stable phase-class, we see that $\delta\theta \approx \pm 2\pi * 0.01$. Our error is primarily dominated by a systematic introduced during the Fourier transform analysis; different choices for how to extract the phase of the dominant Fourier component lead to slightly different results for each phase slip. This is a natural result as the interference pattern is not perfectly periodic in V_P. We estimate this uncertainty to be about $\delta\theta = \pm 2\pi * 0.04$. Assuming impurity sites to be randomly distributed, then, it is reasonable that the plurality of events will have undetectable bulk-edge coupling.

We also observe two "soft" horizontal features near $V_P \sim 0, -0.75\,\mathrm{V}$. These features occur reversibly in B and V_P, and exhibit a slip with $\Delta\Phi/2\pi \sim 0.2$. We interpret these soft slips as impurity states which are very close to the edge controlled by the plunger gate, which can therefor equilibriate with the edge on a time-scale faster than our measurement sweep. Such states would also have a larger degree of bulk-edge coupling, explaining the relatively smaller magnitude of the phase slips. Moreover, these "soft" slips have a nearly vertical trajectory in the B-V_P plane indicating extremely strong coupling to the plunger gate, implying this charge state is strongly localized to defect near the edge. In fact, in the integer quantum Hall regime we observe a number of these defects where we can deduce their location by studying the relative lever arm of the charge degeneracy point to each gate in our device vs. magnetic field (see Appendix D).

We note that the cascade of events which begins at $B > 8.95\,\mathrm{T}$ is consistent with the chemical potential exiting the nearly-incompressible region of a 'hard gap', though the system may remain within the transport plateau. In line with theoretical analysis of gated devices, for $B < 8.95\,\mathrm{T}$ we interpret the bulk to be nearly incompressible, so that anyon charging events are rare. In contrast, outside the gap one $e/3$ anyon enters with every flux quanta so as to keep the density constant. In this regime, the AB and statistical phases

cancel so that $\Phi(B)$ is (on average) constant, as we observe. Remarkably, however, this still occurs through a series of sharp phase slips. This analysis does leave a mystery as to why, within the gap, the rare charging events have an opposite sign from expected. We conjecture this is actually a non-equilibrium effect due to the preparation history before the trace, as will be explored in the following sections.

These striking features can be contrasted with the signals observed in previous fractional quantum Hall edge state interference measurements [134, 144]. In these works, repeatable, *reversible* phase slips in the interference phase were observed, whose location in the $B - V$ plane exhibited a clear dependence on both the magnetic field and gate voltage. Additionally, rather than a sharp jump as observed here, the phase slip occurs continuously over a narrow range of magnetic field and plunger gate. In this range the interference is also suppressed. This is interpreted as a consequence of thermal fluctuations between occupation of N_{qp} and $N_{qp} + 1$ anyons in the inteferometer at the degeneracy point, which contributes a strong 'topological dephasing'. Taken together, their observations suggest the bulk anyon occupation N_{qp} is in equilibrium with the edge on the time scale of the measurement.

4.5 Quasi-particle Dynamics in $\nu = 1/3$

Having established the existence of events consistent with a nearly-quantized value of the predicted anyonic braiding statistics, we now turn to the quasiparticle charging dynamics. Fig. 4.2a shows two interference plots taken over the course of 10 minutes each. The two QPC voltages are set to the same set points as in Fig. 4.2d. In these plots, the plunger gate is fixed while the C gate is swept rapidly around an average value of $\bar{V_C} = 2.23V$; interference fringes are plotted against the deviations δV_C about this average. As in Fig. 4.2d, a series of discrete slips are observed. However, in these

rapid measurements, phase slips do not occur until several minutes into the sweep. As a result, the initial minutes of the sweep show only continuous phase evolution arising from the Aharanov-Bohm effect as the flux through a loop of fixed anyon charge and approximately fixed size. This hysteretic behavior arises naturally in the presence of slow charge dynamics. In this scenario, slow charging leads to a lag between the system's chemical potential and its equilibrium value. This effect will be most pronounced within the where quasiparticle states are decoupled from the edge, as expected for localized states pinned to disorder potentials deep in the sample bulk, consistent with the seemingly random charging events within the plateau region in Fig. 4.2d.

To probe these dynamics directly, Fig. 4.3c, the magnetic field is ramped back and forth over a 40mT range, pausing for 10 minutes at each extreme, while V_C is continuously ramped over a ∼1.5 mV range. In this regime, no charge equilibration is observed over many sweeps, despite the fact that the number of flux quanta in the loop are modulated several flux quanta. This either implies a hard gap, devoid of available quasiparticle states, or equilibration times considerably in excess of ten minutes. Evidence for slow equilbration is visible in Fig. 4.3d, taken for a slightly different values of $\bar{V_C}$. Here the field is ramped and then held fixed for 35 minutes. Several phase jumps are visible after a time delay of 15 minutes. Notably, in two cases, different time domains show nearly identical interference curves, despite the presence of phase slips (summing to 2π) separating them. We identify these with a return to the same quasiparticle number state further implying that charge equilibrates into the interferometer through a small number of highly pinned charge states.

It's possible that the observed pattern of phase slips lends itself to a simple interpretation in terms of two or more defect states. One defect state is located near the edge, and charges and discharges randomly on a timescale of one minute or less. This defect contributes the phase slips observed at $t = 4.8$ 7, and 11 minutes, with a magnitude

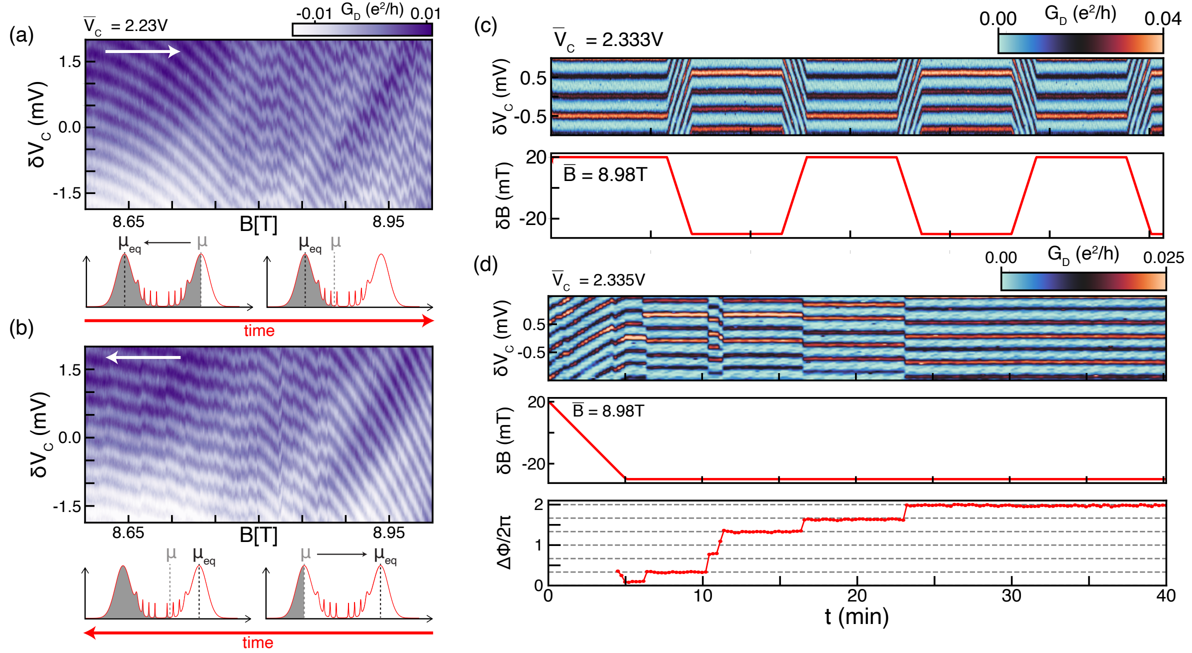

Figure 4.3: **Charging dynamics for quasi-particles at $\nu = 1/3$** **(a)** G_D vs. V_C as the magnetic field is swept from 8.6T to 9T. The latter half of the measurement shows a series of sudden phase jumps like in Fig. 4.2d, beginning after $B > 8.750T$ and continuing until the end of the sweep. Inset cartoon illustrates the how the chemical potential would be changing in equilibrium as the magnetic field is changed from 8.6T to 8.9T, however the true chemical potential (in gray) lags behind its equilibrium value as the charge slowly trickles into the interferometer while the chemical potential passes by a series of localized states. **(b)** Same as panel a, however the magnetic field is swept in the reverse direction, back from 9T to 8.7T. Now, the sudden phase jumps differ in exact location, number, and magnitude, not beginning until $B < 8.9T$. Notably the region in field between 8T and 8.9T is phase slip free and exhibits pure AB oscillations, indicating no quasi-particles have been added to the interferometer bulk. **(c)** Upper panel: G_D plotted against V_C versus time while the magnetic field is varied. Lower panel: B-field magnitude versus time for the data in the upper panel. **(d)** Upper panel: G_D potted versus V_C and time. Middle panel: B-field magnitude versus time for the data in the upper panel. After the field is swept to its final value at t = 5min a series of sharp phase slips is observed indicating a slow equilibration of N_{qp} in the interferometer. Lower panel: magnitude of the sudden phase jumps in the upper panel.

which is significantly less than $2\pi/3$, as expected for an edge-coupled defect. In contrast, the charging of one or more defects deep in the interferometer bulk is slower, occuring on 10 minute timescales and giving a nearly perfectly quantized phase slip magnitude.

4.6 Evolution of Phase Slips in $\nu = -1$ and Localization Transitions

To study the evolution of the bulk charging time, we study integer filling of $\nu = -1$ at B = 4T in a second device of identical structure to one shown in Fig. 4.1c. Working at integer filling allows us to operate the quantum point contacts over a larger range of voltages, while the single chiral edge mode of $\nu = -1$ avoids the complexities of multiple edges, which can give complex interference behavior [87, 57]. Moreover, because no anyon phase slips are expected, working at $\nu = -1$ allows us to characterize bulk edge coupling which is responsible for any observed phase shifts[142]. Here we show the interference patterns at three distinct locations within the $\nu = -1$ field plateau marked in Fig. 4.4a. Fig. 4.4b shows interference data taken at the low-field end of the $\nu = -1$ plateau. Notably, as this data was taken at $\nu = -1$, depleting the interferometer area requires positive instead of negative voltage. Here we observe repeatable 'soft' small magnitude phase slips. These phase-slips occur along lines of positive slope in the B-A_I plane which is consistent with the Rosenow-Stern-Halperin model of bulk-edge coupling where the bulk is highly compressible and adding charge affects the outer area of the interferometer resulting in a phase slip with every charge added.

As we increase the magnetic field and move closer to the center of the $\nu = -1$ transport plateau, we observe a qualitative change in the behavior of the 'soft' phase slips. While the phase slips are still both regular and visible with positive slope in the

B-A_I plane, instead of having a continuous evolution with plunger gate and magnetic field, we observe 'glitchy' behavior near each charge degeneracy point; this is shown in Fig. 4.4b. As we increase the magnetic field further near the center of the $\nu = -1$ plateau, the 'glitchy' behavior stops, and we recover the same behavior observed in the fractional quantum Hall regime where the interference data shows lines of AB phase interrupted by sharp non-repeatable phase slips, shown in Fig. 4.4d. The magnitudes of the extracted phase slips in Fig. 4.4d are shown in Fig. 4.4; the values are extracted in an identical manner to those in Fig. 4.2d.

This behavior for a graphene based system is not fundamentally unexpected. As the magnetic field increases and the filling factor moves closer into the hard gap at $\nu = -1$ one expects any remaining quasiparticle density of states to become localized at sharp coulombic impurity potentials created by defects in the hBN substrate [**?**, **?**]. A cartoon of this transition is shown in Fig. 4.4f. In region I the expectation is the bulk is highly compressible and there is a large set of quasi-particle states which have some net capacitance to the edge of the interferometer. This coupling is expected to shift $A_I(B, N_{qp})$ for every additional flux-quantum threaded through the interferometer, leading to the repeatable 'soft' slips observed. In region II as the field is increased and the filling factor moves more towards the center of the transport plateau. The expectation here is that the states begin to become localized eventually becoming sharp localized impurities as depicted in the cartoon in Fig. 4.4f for region III.

As the quasiparticle density of states becomes more localized the average distance from any bulk impurity to the edge should decrease. The tunneling rate Γ for a quasi-particle on the edge to a local impurity in the bulk scales as $\Gamma \sim e^{-(L/l_b)^2}$, where L is the distance from the edge to the impurity, and l_b is the magnetic length. While the tunneling rate is gaussian in the distance from the edge, the bulk-edge coupling scales exponentially in the gate distance (from the monolayer to the top gate), which in our

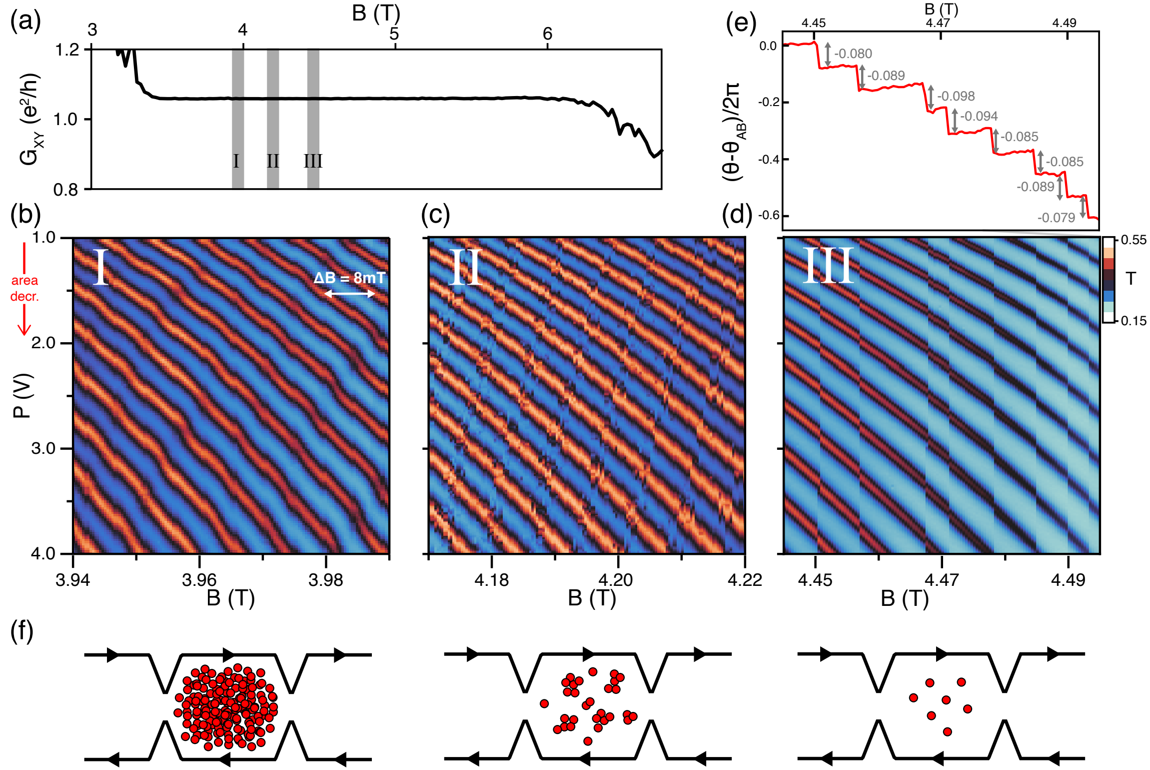

Figure 4.4: **Evolution of the quasi-particle charging timescale in the IQH regime. (a)** Three ranges within the $\nu = -1$ field plateau at fixed density, in which the Fabry-Perot interference pattern is measured and shown below. **(b)** Interference in region I, showing gradual phase slips that occur approximately with every addition of one flux quantum. The phase slips occur along positively sloped lines. **(c)** Interference data across region II, showing phase slips which are now observed as two-state switching noise concentrated along positively sloped "glitchy lines". **(d)** In region III, the phase slips are now sudden in time and do not reverse as the measurement continues, a manifestation of a switching time much longer than the time taken to measure several line traces. **(e)** The phase calculated from the FFT of panel D, with a linear-in-B Aharonov-Bohm contribution subtracted. The average magnitude of the discrete jumps, determined from the hard-slip regime (III), is $\Delta\theta = -0.087$, consistent with a mild amount of bulk-edge coupling as observed in panel b. **f** Schematic illustration of bulk quasi-particle distribution for the corresponding regions I, II and III respectively.

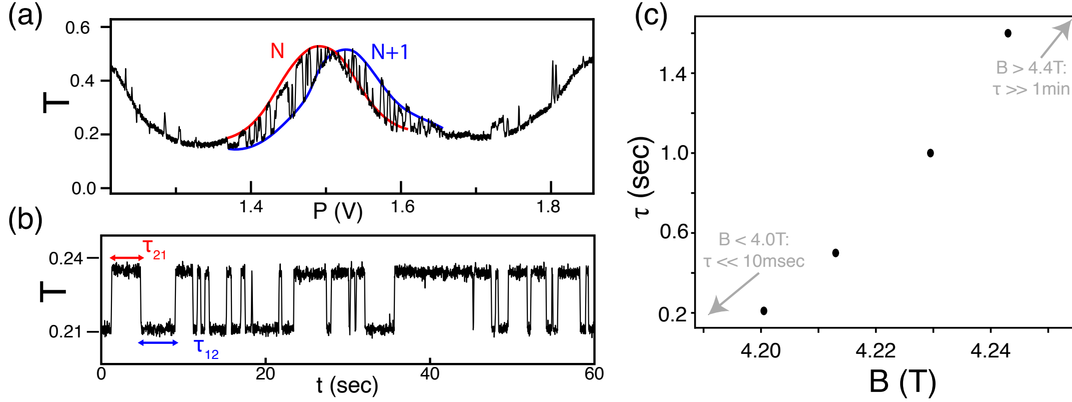

Figure 4.5: **Two-state switching noise for "glitchy" phase slips in region II.** **(a)** A line trace of an interference fringe measured slowly across a noisy line by tuning the plunger gate. The interference signal can be seen to be switching between two envelopes (drawn in as guides to the eye) which are phase shifted. **(b)** The transmitted current plotted as a function of time while the plunger gate is fixed on one of the noisy charge-degeneracy lines. **(c)** The characteristic time τ as a function of magnetic field, determined from fitting the time separation of switching events to an exponential distribution, from switching noise measured at four distinct charge-degeneracy lines near region II.

device is $\approx 45\,\text{nm} > 3.5 l_b$. This remarkable difference in length scale enables us to observe an increase of over three orders of magnitude in the tunneling time $\tau \sim 1/\Gamma$ by measuring the effect on the interference phase resulting from weak bulk-edge coupling.

For $B < 4.0T$ where we observe the continously tunable 'soft' slips, the tunneling time from the edge to states in the bulk is less than the measurement time, set to 10ms (set via our lock-in time constant). Similarly, for $B > 4.4T$ where the phase slips become unrepeatable and occur instantaneously, the tunneling time should be much greater than the time it takes to perform a single line trace, in this case 1 minute. To extract τ quantitatively as a function of magnetic field we focus on the 'glitchy' slip regime in Fig. 4.4c. A line trace of the transmission coefficient, $T \equiv I_{out}/I_{src}$ where I_{src} is the sourced current into the interferometer, versus V_P measured slowly across a characteristic 'glitchy' phase slip is shown in Fig. 4.5a. Here the tunneling time into a bulk quasi-particle state from the edge is shorter than the line-trace time, but longer

than the measurement averaging time set by the lock-in amplifier. As the plunger gate is swept at a fixed magnetic field (B = 4.183T), near the charge degeneracy point T can be observed to bounce between two possible curves (guides to the eye are drawn in red and blue in Fig. 4.5a). We attribute these two envelopes to the two possible interference patterns which correspond to either N or N+1 quasi-particles in the bulk, and the phase shift simply comes from a small bulk-edge coupling effect as in region I but now the average distance from the edge to the bulk is on the order of ℓ_b such that 10ms $<< \tau <<$ 1min.

To verify that indeed the noise observed in Fig. 4.5a is really the result of a two-state quantum switching model, we park at a fixed value of $V_P = 1.45V$ and B = 4.183T and monitor T as a function of time as shown in Fig. 4.5b. We see that the trace takes on a binary distribution and switches instantaneously back and forth between two values. At the charge degeneracy point we expect that the tunneling rate has some characteristic time τ, however at an arbitrary magnetic field and plunger gate voltage de-tuned in energy slightly from the the charge degeneracy point we expect that the ratio $P_{1\to2}/P_{2\to1} = e^{-\Delta/k_bT}$, where $P_{1\to2}$ is the probability for an electron to hop from state 1 to state 2, $P_{2\to1}$ is the probability for the electron to hop from state 2 to 1, and Δ is the de-tuning in energy away from the charge degeneracy point. This implies there are two characteristic time scales: τ_{12} which is the average occupation time in state 1 before transitioning to state 2 and τ_{21} which is the average occupation time in state 2 before transitioning to state 1. In a two-state switching model then the expected τ at charge degeneracy follows the equation

$$\frac{1}{\tau} = \frac{1}{\tau_{12}} + \frac{1}{\tau_{21}} \tag{4.3}$$

If we define the low conductance value to be state 1 and the high conductance value to be state 2 in Fig. 4.5b, then we may histogram the values of τ_{12} and τ_{21} respectively.

Following equation (4.2) we find that for this point at B = 4.183T τ = 200ms.

We can repeat this analysis for several 'glitchy' slips at increasing values of magnetic field. The extracted τ is plotted verus B-field in Fig. 4.5c. The tunneling time τ is observed to increase by nearly an order of magnitude with only a 40mT change in magnetic field. This rapid increase in τ with magnetic field shows that as the filling becomes close to the hard-gap region, the bulk quasi-particle states rapidly become localized and edge quasi-particles can no longer tunnel into the edge on short time scales leading to the non-repeatable instantaneous hard-slips observed in region III. At $\nu = 1/3$ at B = 9T, the data is primarily analogous to region III. However, the observed phase shifts no longer only come from bulk-edge coupling effects, but also pick up a contribution from the anyon phase, θ_a. In the middle of the hard-gap at $\nu = 1/3$ there will be a few edge-coupled local defects, however the majority of tunneling events will come from strongly localized defects deep in the bulk. These should have negligible bulk-edge coupling and they account for the vast majority of phase slips we observe at $\nu = 1/3$ that are nearly quantized to a magnitude of $2\pi/3$.

4.7 Measurements at fixed B and A_I but different N_{qp}

The fact that the quasi-particle content of the interferometer seems to be out of equilibrium for 10s of minutes makes it extremely easy to identify different phase classes related to addition of anyons into the bulk. Fig. 4.6a shows G_D versus V_C and time. Initially, V_C is rapidly pulsed near the edge of the $\nu = 1/3$ plateau at $V_C = 2.2V$, this is done to populate a series of quasi-holes out of equilibrium. Then V_C is rapidly returned to near the center of the plateau. In Fig. 4.6a V_C is varied rapidly back and

forth over a range of about 4mV. Here nearly 12 periods may be observed within the 4mV window indicating a change of 12 flux-quantum through the active interferometer area. In principle V_C should directly control the electronic density in the bulk of the interferomter, however despite changing the flux through the interferometer by several flux-quanta, the phase remains stable implying no anyons have tunneled into the bulk. As the average value of V_C is increased, a series of 17 distinct phase slips can be observed. These slips are nearly quantized to $\Delta\theta/2\pi = 1/3$, and the phase slip magnitude versus time is plotted in Fig. 4.6b.

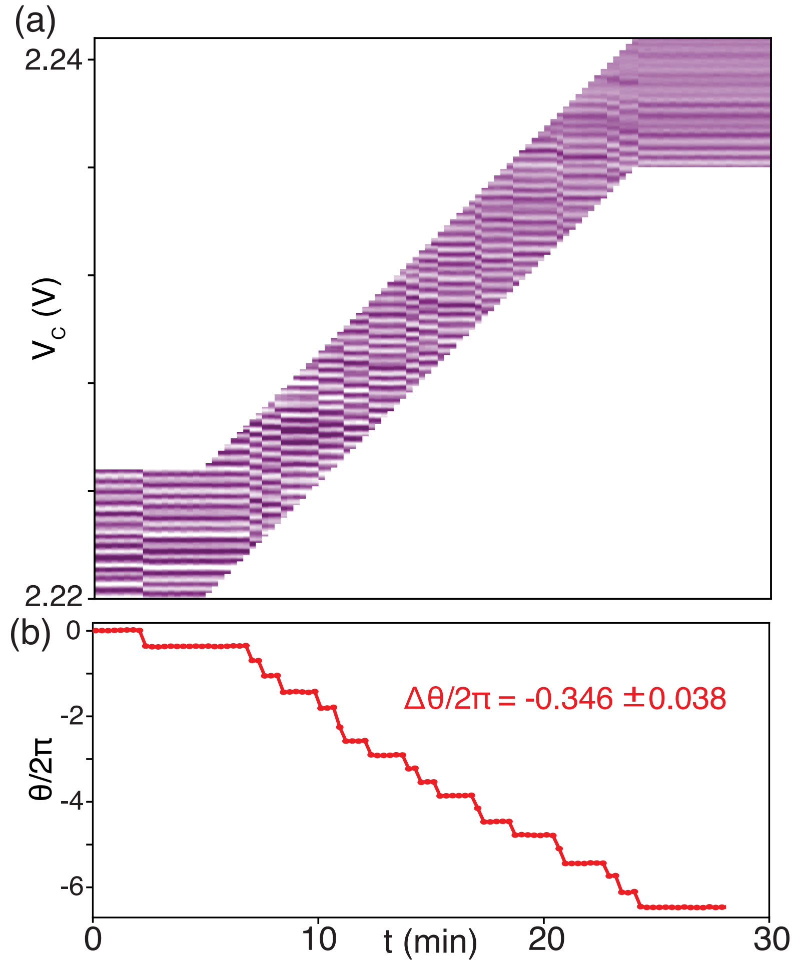

Figure 4.6: **Percolation of anyons into the interferometer (a)** G_D versus V_C and time. Here V_C is swept in a $\approx$ 4mV window rapidly back and forth. The mean value of this window is moved slowly over the course of 30 minutes, as the average value of V_C is increased anyons can be seen to slowly percolate into the interferometer, each time causing a sharp sudden slip in the phase of the interference. Notably before this sweep occurred, V_C made large, rapid excursion to the edge of the $\nu = 1/3$ plateau to 2.2V to populate a series of states in the bulk out of equilibrium. **(b)** Phase slip magnitude versus time for each detected slip. The average value of $\Delta\theta/2\pi = -0.346 \pm 0.038$.

Remarkably, because the charge equilibration time is so long, we are able to take many traces within the same range of V_C and at fixed B while the anyon charge slowly equilibrates. This implies that we can perform measurements at exactly the same A_I and at exactly the same B and purely isolate the effect of N_{qp}. Fig. 4.7 shows a representative

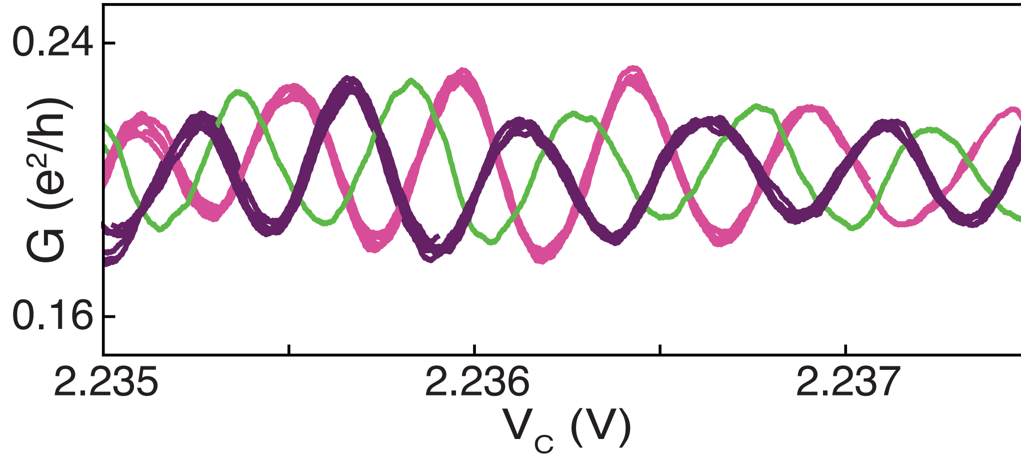

Figure 4.7: **Anyon phase classes** Representative traces of the interference as a function of the center gate voltage as the center of the sweep range is varied over time. The traces are seen to fall into three distinct classes of phase, and the phase remains stable on the timescale minutes as the sweep location changes.

set of 1d traces of the interference taken at different average values of V_C in Fig. 4.6a. Despite rapid sweeping of V_C over several interference periods, the phase remains stable on minute time scales. Eventually when an anyon percolates into the bulk of the interferometer, the trace is seen to shift by $\Delta\Phi \approx 2\pi/3$, and then the phase then remains stable over many additional sweeps of V_C. In Fig. 4.7 we only observe three distinct phase classes which we attribute to -1, 0, and 1 anyon in the interferometer mod 3.

A

Appendix A: QPC Fabrication

To fabricate our quantum point contact devices, the Graphene and hBN crystals were mechanically exfoliated from bulk crystals using a combination of thermal release tape and scotch magic tape. The initial mother-tape is prepared using 3M Scotch-brand magic tape for graphite or 3M Scotch-brand greener magic tape for hBN, and additional daughter tape for each crystal is prepared by placing a piece of tape over the original mother tape on the exposed crystal side. The daughter-tape is removed from the mother-tape, cleaving the bulk crystals along the c-axis, then transferred onto a 1cm x 1cm doped Si chip with 285nm of thermally-grown SiO_2 on the surface for hBN, and 90nm

of thermally grown SiO_2 for graphite. For graphite, the substrate is heated to 110° C for 60 seconds, before removing the tape quickly to reduce glue residue remaining on the SiO_2 surface. For hBN, the daughter-tape is transferred onto the SiO_2 surface at room temperature and is removed from the SiO_2 slowly. The Si/SiO_2 substrates are cleaned by a standard solvent process: the chip is cleaned in acetone for 5 minutes in a high power ultrasonic bath, followed by an IPA wash, and finished with an N2 blow-dry. Additionally, for graphite the SiO_2 surface is treated in O_2 plasma at 100W and 300mTorr for 60 seconds in order to promote adhesion of large multilayers. The resulting exfoliated crystals are then characterized by optical microscopy.

AFM-LAO was performed on a Bruker Dimension Icon AFM. Exfoliated graphite flakes, prepared as described above, are loaded into the AFM. The humidity is controlled using a bang-bang style humidity controller. The plant is formed by a beaker filled with 250mL of deionized water placed on a hot plate at 120° C. Once the humidity sensor measures higher than 50% RH, the hot-plate is switched off. We pattern sub 100 nm crosses into a 3 nm graphite flake to form the top gate of the quantum point contact. This is accomplished using a Pt/Ir coated Arrow-NcPt AFM probe from nanoandmore. A topographical map of the graphite flake is obtained and the cross pattern is placed in an area with no visible defects. The lithography is performed in Bruker's Nanoman software package which allows for precise control of the direction, speed, and deflection of the conducting AFM probe. Graphite can be etched with AFM-LAO under a variety of conditions, however we have found that lithography performed in contact mode with an 18V peak-to-peak excitation at 150kHz provided the smallest line-widths achievable in our system. For new AFM probes, typical line-widths are on the order of 60-70 nm. This leads to a QPC critical dimension (tip-to-tip distance) between 90 and 100 nm . However, due most likely to hydrocarbon build up or natural wear on the AFM probe, the cut-width broadens to 100 nm after $\sim$150 μm of cutting.

Before assembling the van der Waals heterostructure we fabricate a 'transfer-slide:' a PDMS stamp adhered to a glass slide with a polycarbonate laminate transferred on top used to 'pick-up' the first layer of hBN. Initially, 8g of Sylgard 184 PDMS is mixed in a 10:1 ratio by weight with a curing agent and poured into a standard 100 mm plastic petri dish. The PDMS is left to cure at room temperature for 24 hours in a vacuum chamber in order to remove any bubbles that formed during mixing. Additionally, another 3g of Sylgard 184 PDMS solution is mixed with a curing agent and left to cure partially at room temperature under vacuum for 2 hours. A PDMS cylinder is cut out using a 2 mm hole punch from the 8g PDMS batch and is then adhered to a glass slide using the partially cured PDMS. An additional droplet of partially cured PDMS is pipetted onto the cylinder in order to form a dome. Slides are left to finish curing for another 24 hours at room temperature. The resulting slides are then inspected under an optical microscope for dirt particulates.

The polycarbonate laminate is made from a 13.3% wt/vol ratio of Bisphenol-A polycarbonate (PC) in cyclopentanone. Unaided, cyclopentanone will only dissolve a 4% wt/vol solution of PC, however by using the QSonica 500 ultrasonic wand, solutions up to 15% wt/vol can be made. This recipe was derived from previous work by Abbas [**?**]. Due to its significantly lower vapor pressure than chloroform, PC dissolved in cyclopentanone can be effectively spun onto a Si substrate. Thin films of PC are prepared by spinning the mixture onto a Si substrate at 1400 rpm for 60 seconds. The thin film is then subsequently transferred onto a domed PDMS stamp. The transfer slide is heated between 160°C to 180°C for 5 minutes in order to increase the adhesion between the PC film and the PDMS stamp as well as to remove any air bubbles that may have formed during transfer of the film.

We begin the assembly of the van der Waals heterostructure by picking up an hBN flake larger than 100um in both width and length. Ensuring the first hBN has the largest

area aids in assembling the remaining layers since subsequent crystals will adhere entirely to another van der Waals material. The transfer slide is engaged at a 0° tilt angle, with the substrate heated to 70°C, and with the touch-down point 100-150um away from the center of the first hBN layer. Once the transfer slide is brought into near contact the substrate is heated to 105°C. This causes the transfer slide to fully engage and laminate over the first hBN layer. The substrate is then cooled naturally back down to 70° which retracts the transfer slide and removes the target hBN flake from the SiO_2. Next, the AFM-LAO etched graphite top gate is picked up while entirely encapsulated by the large initial hBN layer. There are a number of advantages to using a domed PDMS transfer slide, one of which is that the engage point is in the center of the PDMS stamp, as opposed to the edge, which has fewer dust particulates that can interfere with assembly. Moreover, domed PDMS transfer slides are known to reduce strain during vDH assembly [**?**]; it turns out this technique is critical for picking up AFM-LAO nano-structures without inducing tears or folds.

The PC laminate is extremely uniform as a result of being spun onto a Si substrate. This also minimizes a common issue in assembling van der Waals heterostructures where the polycarbonate exhibits stochastic adherence to the SiO_2 substrate. This often causes a 'jerk' like motion during stacking which easily can cause graphite nano-structures to tear. The remaining layers are assembled in the same manner; the full resulting device stack can be seen in Fig. 2.4c. The stack is then deposited onto a doped silicon substrate with 285nm of thermally grown oxide, which forms the basis for a global bottom gate used to dope the graphene contacts. This is accomplished by engaging the transfer slide and heating the substrate to 180°C (above the glass transition temperature of PC) to detach the PC from the PDMS stamp. The laminate is then dissolved in chloroform for a minimum of 30 min. Afterwards, the sample is rinsed in acetone and IPA, and then blown-dry with N2.

Heterostructures are post-processed using standard electron beam lithography, vacuum deposition, and dry-etching processes. A device-defining plasma etch is used to separate the nanotextured graphite into four quadrants that we label North (N), South (S), East (E), and West (W): this is accomplished by inductively coupled plasma (ICP) etching in 40 sccm of CHF_3 and 4 sccm of O_2. This etch also separates the graphene contacts C1-8 such that any two contacts are only connected through the dual-gated region. Additionally, the conducting Si substrate is used to dope each contact and prevent the formation of p-n junctions at the boundary between the contacts and the dual-gated region. Finally, several trenches are etched across the boundary to the dual-gated region to introduce local scattering sites that improve equilibration between the contacts and quantum Hall edge modes in the device region.

The etch mask is patterned by lifting off 40nm of Al using a polymethyl methacrylate (PMMA) A4 495K / A2 950K bilayer resist. The PMMA is exposed using a 30kV electron-beam in an FEI SEM at 4004uC/cm^2 and developed in a mixture of DI:IPA 1:3 kept at 10°C. Al is deposited at 0.3A/s and the lift off is done for over 12 hours in N-Methyl-2-Pyrrolidone (NMP). Post etching, the Al is dissolved in AZMIF300 photoresist developer which contains $< 3\%$ by weight of Tetramethylammonium hydroxide (TMAH). Edge contacts are deposited onto the exposed graphene contacts and graphite gates using the same bilayer PMMA mask. Before vacuum deposition, a brief contact cleaning etch in an ICP with 40 sccm of CHF_3 and 9 sccm of O_2 is performed. Subsequently, a metal stack of Cr/Pd/Au 3/15/185 nm is deposited and lifted off. Special care is taken to deposit the Cr layer at 0.3A/s in order to improve coating uniformity.

B

Appendix B: Measurement Methods

B.1 QPC Experiments Chapter 3, Sections 3.3 - 3.6

Experiments were performed in a dry dilution refrigerator with a base temperature of 20mK. Electronic filters are used in line with transport and gate contacts in order to lower the effective electron temperature. To improve edge mode equilibration to the contacts most measurements are performed at 300mK unless otherwise noted. Electronic measurements were performed using standard lock-in amplifier techniques. For the diagonal conductance measurements an AC voltage bias at 17.77Hz is applied via a 1000x

resistor divider to (see Fig. 3.2a or Fig. B.1 for contact references) C3-4 and the resulting current is measured using an Ithaco 1211 trans-impedance amplifier on C5-6 with a gain of 10^{-7} A/V. We use transport contacts in pairs to decrease the contact resistance and improve edge-state equilibration, exciting an AC voltage on contacts C3/C4, and the measuring the current I_{out} on contacts C5/C6. The diagonal voltage drop, V_D, is measured between C1/C2 and C7/C8. We then define $G_{\mathrm{D}} \equiv I_{out}/V_D$. Note that the sign convention used here is such that G_D is positive for data measured on the hole side of the device, $\nu < 0$. The voltage is measured between contacts C1-2 and C7-8 with an SR560 voltage pre-amplifier with a gain of 1000. For two terminal measurements the same AC bias is applied to contacts C1-4 and the current is measured via C5-8. DC bias was added on top of the AC bias using a passive summer.

B.2 QPC Experiments Chapter 3, Section 3.7

B.2.1 Measurement

Experiments were performed in a dry dilution refrigerator with a base temperature of 20mK. Electronic filters are used in line with transport and gate contacts in order to lower the effective electron temperature. To improve edge mode equilibration to the contacts most measurements are performed at 300mK unless otherwise noted. Electronic measurements were performed using standard lock-in amplifier techniques. For the diagonal conductance measurements an AC voltage bias at 17.77Hz is applied via a 1000x resistor divider to (see supplementary Fig. 1 for contact references) C3-4 and the resulting current is measured using an Ithaco 1211 trans-impedance amplifier on C5-6 with a gain of 10^{-7} A/V. The voltage is measured between contacts C1-2 and C7-8 with an SR560 voltage pre-amplifier with a gain of 1000. For two terminal measurements the

same AC bias is applied to contacts C1-4 and the current is measured via C5-8. DC bias was added on top of the AC bias using a passive summer.

We use transport contacts in pairs to decrease the contact resistance - improving transport quality (See Fig. B.1). The diagonal conductance is determined by exciting an AC voltage on contacts C3/C4, and then measuring the resulting AC current I_{out} on contacts C5/C6. The diagonal voltage drop, V_D, is measured from C1/C2 to C7/C8. The differential diagonal conductance is then defined as $G_D = I_{\text{out}}/V_D$.

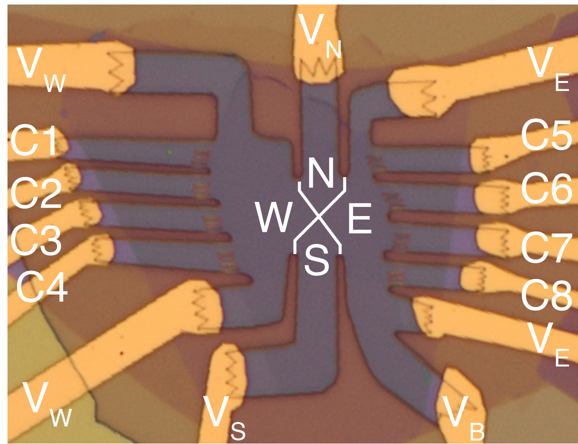

Figure B.1: **Optical Micrograph of Measured Device** Transport contacts to the monolayer are labeled C1-8, while the gates are labeled by their corresponding control voltages V_i.

C

Appendix C: Analysis and Supplementary Information for Chapter 3

C.1 Paritioning FQH Edge Modes

C.1.1 DC Voltage Bias Correction

We used a set of cryogenic filters at the mixing chamber in order to help equilibrate the electrons in the graphene 2DEG to the temperature of the dilution refrigerator (at

the mixing chamber). These filters contain a set of RF pi-filters with small component values which at low meausrement frequencies are negligible. In addition, there are a set of RC filters with a roll-off frequency of 6.6kHz; these filters have a series resistance of $R = 3\,\mathrm{k}\Omega$ each. In order to investigate the DC bias directly across the QPC it is necessary to take into account known filter resistances since they inherently form a voltage divider between themselves and the two-terminal resistance across the QPC defined as R_{DUT}. Determining the relationship between the applied DC voltage at the input of the filters (a known value defined as V_{DC}) and the voltage bias across the sample, defined as V_{DUT}, is straightforward. At low frequencies, the current drawn to any floating contacts is negligible so the DC voltage across the sample is well approximated by

$$V_{\mathrm{DUT}} = V_{\mathrm{DC}} - (2(R/2) + 50\Omega) \cdot I \tag{C.1}$$

where I is the DC current through R_{DUT}. In all tunneling measurements performed in this work pairs of contacts are tied together, so the effective series filter resistance is $R/2$. The $50\,\Omega$ is the lock-in output impedance. While the DC current is not known a priori, differentiating with respect to V_{DUT} the above equation gives:

$$1 = \frac{\mathrm{d}V_{\mathrm{DC}}}{\mathrm{d}V_{\mathrm{DUT}}} - (R + 50\Omega)\frac{\mathrm{d}I}{\mathrm{d}V_{\mathrm{DUT}}} \tag{C.2}$$

This equation can be rearranged to isolate $\mathrm{d}V_{\mathrm{DUT}}$ and $\mathrm{d}V_{\mathrm{DC}}$, given below.

$$\mathrm{d}V_{\mathrm{DUT}} = \frac{\mathrm{d}V_{\mathrm{DC}}}{1 + (R + 50\Omega)\frac{\mathrm{d}I}{\mathrm{d}V_{\mathrm{DUT}}}} \tag{C.3}$$

The differential conductance across the QPC, $G_{\mathrm{D}} = \mathrm{d}I/\mathrm{d}V_{\mathrm{DUT}}$, appears in the denominator. Integrating this equation leaves the final correction formula, which can be expanded

for $3050\Omega \cdot G_{\mathrm{D}} \ll 1$ to give:

$$V_{\mathrm{DUT}} = \int_0^{V_{\mathrm{DC}}} \frac{\mathrm{d}V'_{\mathrm{DC}}}{1 + (R + 50\Omega)G_{\mathrm{D}}(V'_{\mathrm{DC}})} \approx V_{\mathrm{DC}} - (3050\Omega)\int_0^{V_{\mathrm{DC}}} \mathrm{d}V'_{\mathrm{DC}} G_{\mathrm{D}}(V'_{\mathrm{DC}}) \quad \text{(C.4)}$$

This correction is applied for all the tunneling curves in the main text Fig. 3.7d and the collapsed curves in the main text Fig. 3.7f.

C.2 Luttinger Liquid Tunneling Data Analysis

The theoretical expectation given by main text Eq. (1) is that the reflection coefficient R has no terms which depend solely on voltage bias and not temperature. Consequently, to compare our raw data with the predictions from chrial Luttinger liquid theory we need to remove a temperature independent background. Fig. C.1a shows the unprocessed dependence of $1/G_{\mathrm{D}}$ versus V_{bias} for the same series of temperatures listed in main text Fig. 3d. At large voltage bias, the temperature dependent part of $1/G_D$ is expected to flatten out, however while we do observe negligible temperature dependence for $|V_{\mathrm{bias}}| > 500\,\mu\mathrm{V}$, there is a smooth variation in the bias dependence which is the same for all temperatures. Fig. C.1b shows the standard deviation of $1/G_D$ over temperature, denoted as $\sigma_T(1/G_D)$, versus V_{bias}. We define the voltage bias value for which there is no longer any discernible temperature variation between the data sets by choosing V_{bias} such that $\sigma_T(1/G_D) < 0.0012$. This range includes all values of V_{bias} which fall outside the bounds of the black dashed lines in Fig. C.1b. Fig. C.1c shows $1/G_D$ versus V_{bias} averaged over all data sets at varying temperatures between 141 mK and 550 mK, defined as $\overline{1/G_D}$ (additional data sets not shown in Fig. C.1a for clarity are included in this average). The background, plotted in Fig. C.1d, is then defined by $\overline{1/G_D}$ where ever $\sigma_T(1/G_D) < 0.0012$; the black dashed line in the same panel is the best-fit fourth order polynomial

to the extracted background. Fig. C.1e shows $1/G_D$, for the same temperatures in Fig. C.1a, with the background polynomial subtracted (not including the constant offset). Here we define the saturation resistance R_{sat} as the value $\overline{1/G_D}$ saturates to at high bias for all temperatures; practically this is computed by averaging $\overline{1/G_D}$ over $V_{\text{bias}} \in [-1\,\text{mV}, -0.75\,\text{mV}]$ and $V_{\text{bias}} \in [0.75\,\text{mV}, 1\,\text{mV}]$, yielding an $R_{\text{sat}} = 0.775\ h/e^2$. Knowing R_{sat}, the value of the reflection coefficient can be computed from $R_D \equiv 1/G_D$, given by the formula inset into Fig. C.1f, following the procedure outlined in Refs. [82, 38, 83].

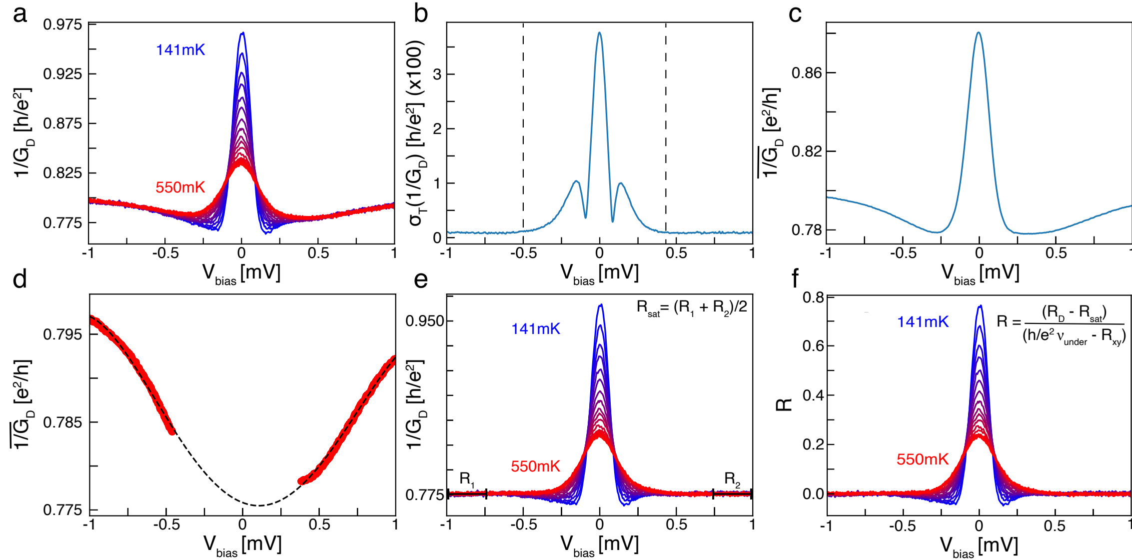

Figure C.1: **Extended analysis of temperature dependent tunneling data (a)** Diagonal resistance, defined as $1/G_{\text{D}}$, versus V_{bias} for the same gate configuration as main text Fig. 3c at $V_{\text{NS}} = -3.925V$ and same temperature values as main text Fig. 3d. **(b)** The standard deviation of R_D defined as σR_D versus bias taken across all temperatures between $T = 141\,\text{mK}$ and $T = 550\,\text{mK}$. Additional temperature values at finer increments are included which are not shown in panel (a). Dashed lines indicate threshold in V_{bias} where $\sigma R_D < 0.0012$. **(c)** R_D versus V_{bias} averaged over all temperatures. **(d)** Portion of the temperature averaged R_D in panel (c) plotted only where the standard deviation σR_D falls below 0.0012. The black dashed line is a fit to a quartic polynomial which then defines the temperature independent background. **(e)** R_D plotted versus V_{bias} for various temperatures with the quartic background extracted in panel d subtracted (except for the constant term). A value for R_{sat}, i.e, the resistance which panel (e) saturates to can be defined by averaging R_D over a window of $250\,\mu\text{V}$ on either side of $V_{\text{bias}} = 0$ at high bias, and then averaging together the results. **(f)** R plotted versus V_{bias} for the same temperatures in main text Fig. 3.7d.

C.3 Universal Chiral Luttinger Liquid Behavior at a Graphene Fractional Quantum Hall Point Contact

C.4 Junction Electrostatics: Reconstruction Effects and Resonant Scattering

If the slope of the confining electric potential is soft a bevy of edge reconstruction effects may arise. These include resonant transmission through reconstruction-stabilized local states, complicating the interpretation of the conductance across the QPC. In this manuscript we focus on the regime of "sharp" electrostatics where the edge reconstructions are negligible, which can be achieved by tuning the gates in our device geometry[26]. The sharpness of a potential is defined via the competition between two energy scales: the "confinement energy" associated with the applied potential, $E_V \equiv e|\nabla V|\ell_B$, and the Coulomb energy, $E_C = \frac{e^2}{4\pi\epsilon\ell_B}$. $E_V < E_C$ corresponds to the "soft" electrostatic regime; here, the charge may distribute itself primarily by minimizing the Coulomb repulsion energy. Along a translation-invariant quantum Hall edge, this leads to the formation of additional incompressible strips along the boundary, resulting in additional edge modes that do not correspond to the primary bulk filling factor[78, 94]. In quantum point contacts made identically to the one presented in this work, the soft-edge regime is characterized by local islands of charge stabilized at the potential saddle point, which mediate resonant tunneling between edge modes across the quantum point contact[26]. In contrast, in the sharp electrostatic regime where the confinement energy is larger than the Coulomb energy, $E_V/E_C > 1$, simple tunneling between two edge modes at a point is recovered.

The gate voltages necessary to achieve appropriately sharp confinement can be identified by observing the qualitative behavior of the conductance near pinch-off. First we examine a regime where the phenomenology is simplest—Fig. C.2A presents a plot of the conductance measured with a fixed filling factor $\nu = 1$ in both the East and West quadrants. On the x-axis, V_{NS} is changed to vary the filling factor in the North and South quadrants across a fixed range of densities by changing the quantity $V_{\mathrm{NS}} + \alpha V_{\mathrm{BG}}$, where α is the capacitance ratio between the top and bottom graphite gates. Along the y axis, V_{BG} is swept while concurrently sweeping V_{EW} in the opposite direction to fix the quantity $V_{\mathrm{EW}} + \alpha V_{\mathrm{BG}}$, maintaining a constant filling factor in the East and West quadrants while varying the difference $V_{\mathrm{EW}} - V_{\mathrm{BG}}$, which effectively tunes the confinement energy E_V.

To illustrate this in more detail, we analyze the electrostatics near the points marked I and II in Fig. C.2A, which are representative of the "sharp" and "soft" regimes, respectively. In the "sharp" regime represented by point I, the conductance exhibits a monotonic step from $G = 0$ to $G = \frac{e^2}{h}$ as the QPC is opened; this is what is expected for non-resonant tunneling between two integer edge modes at a QPC. In contrast, for the "soft" regime represented by point II, the conductance behaves non-monotonically, displaying several peaks and dips as the junction is opened.

Fig. C.2B-C present finite element analysis simulations of the electrostatic potential at the graphene layer of the device (calculated using COMSOL Multiphysics) for an idealized device geometry with voltages corresponding to these two operating points.

Note that COMSOL calculates the *unscreened* potential applied by the gates. The two dimensional system will then screen this potential. Theoretical literature on quantum Hall edges[78, 115, 111, 116] indicates that the nature of the charge carrier density caused by the this screening undergoes one or more phase transitions as a function of the steepness, leading to the well known edge reconstruction; roughly, simple edge structures

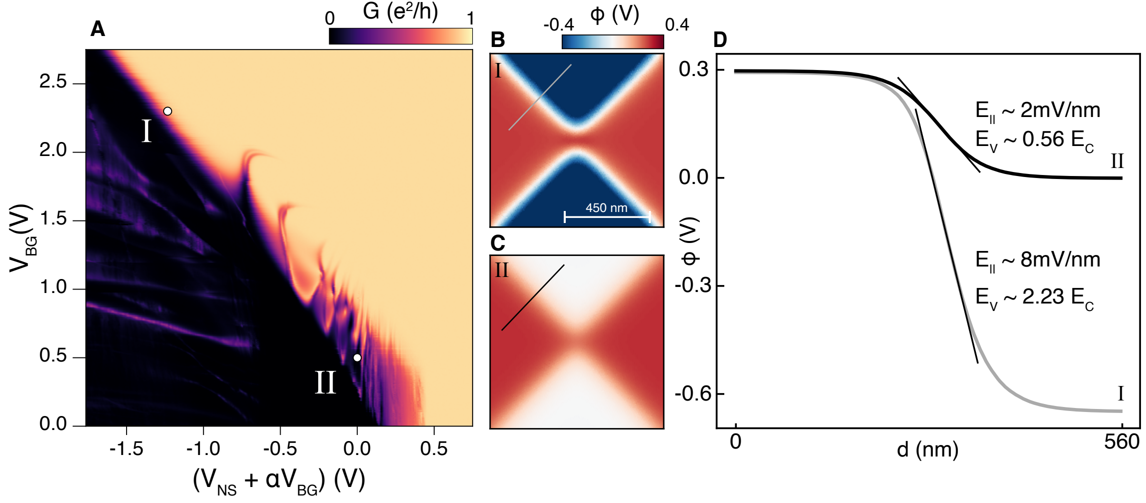

Figure C.2: **Signatures of reconstruction in G between $\nu = 1$ edge modes. (a)** The conductance measured across the QPC with both the East and West regions in $\nu = 1$ at B = 8T. The East and West gate voltages are swept in the opposition direction of V_{BG} along the y axis, through the range $V_{\mathrm{EW}} \in (0.6V, -2.191V)$, to maintain a fixed filling factor while varying the voltage difference and thereby the potential sharpness. **(b)** The simulated electric potential at the monolayer, corresponding to the operating point I. **(c)** Same as (b) but at the operating point II, where the potential is much softer. **(d)** Simulated potential along the contours marked in grey and black in panels B and C, respectively. The softness is quantified by the maximum magnitude of the in-plane confining electric field, $E_{\|}$ (*i.e.* simply the gradient of the potential normal to the boundary between the N(/S) and E(/W) regions).

obtain for when $E_V/E_C \gtrsim 1$, and more complex edges including counterpropagating modes obtain for $E_V/E_C < 1$. A phenomenological treatment of edge reconstruction in graphene devices with the same device geometry is described in [26].

Fig. C.2D shows the potential along the illustrated lines normal to the boundary between the $\nu = 1$ and depleted regions. We can quantitatively characterize the threshold sharpness by estimating the ratio E_V/E_C from the simulated confining electric field. At $B = 8$ T the Coulomb energy is $E_C \approx 33$ meV, where the relevant $\epsilon = \sqrt{\epsilon_\perp \epsilon_\|} \approx 4.8$ taking $\epsilon_\perp = 3.5$ and $\epsilon_\| = 6.6$. Experimentally, the effects of resonant transmission disappear above $E_V \approx 61$ meV, so $E_V/E_C > 1.85$.

Fig. C.2A makes it clear that in the IQH regime, local effects from edge reconstruction

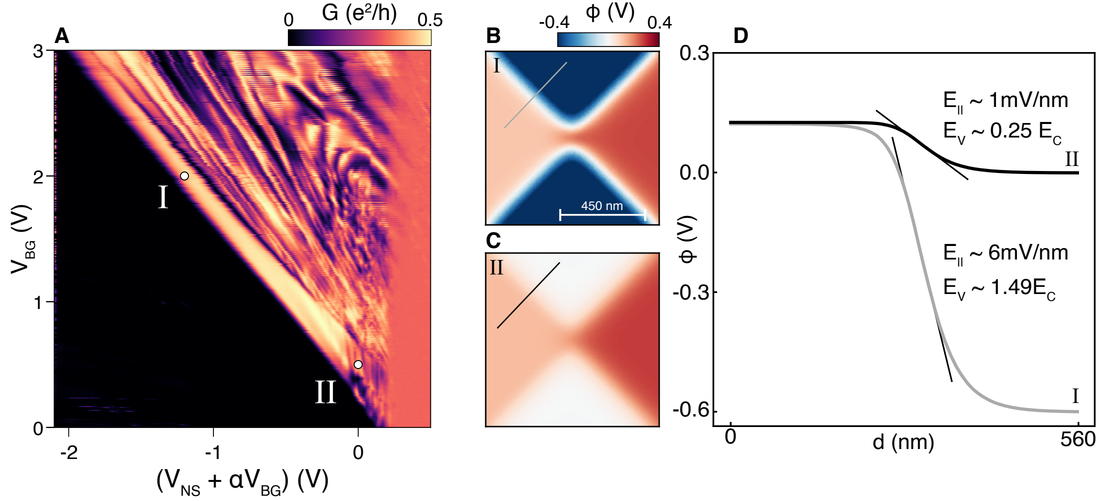

Figure C.3: **Signatures of reconstruction in G between $\nu = 1$ and $\nu = 1/3$ edge modes (a)** The conductance measured across the QPC with $\nu_\mathrm{W} = 1/3$ and $\nu_\mathrm{E} = 1$ at B = 9T. Along the y-axis, both the East and West gates must be swept in the opposite direction of the back gate, but at distinct voltages $V_\mathrm{E} \in (0.57V, -2.475V), V_\mathrm{W} \in (0.256V, -2.79V)$, to maintain fixed filling factors. **(b)** The simulated electric potential at the monolayer, corresponding to the operating point I. **(c)** Same as (b) but at the operating point II, where the potential is much softer. **(d)** Simulated potential along the contours marked in grey and black in panels B and C, respectively, at the boundary of the $\nu_\mathrm{W} = 1/3$ region. The boundary of the $\nu_\mathrm{E} = 1$ region is necessarily sharper since $V_\mathrm{E} - V_\mathrm{BG} > V_\mathrm{W} - V_\mathrm{BG}$.

can be suppressed by making the confining potential sufficiently sharp. To find a similarly universal regime for the $\nu = 1$ to $\nu = 1/3$ configuration, we repeat the characterization above with the East and West regions fixed to those filling factors, shown in Fig. C.3A. While many additional peaks and dips occur beyond the initial conductance step, many features are consistent with the $\nu = 1$ to $\nu = 1$ case. First, focusing only on the region near the first conductance step, when the QPC is just barely open, the qualitative features are similar Fig. C.2A, with a smooth step up to a plateau (here with a value of $G \approx \frac{e^2}{2h}$) in the sharp regime, near point I, and number of resonant peaks arising in the soft regime at point II. Notably, resonant transmission effects near the initial conductance step disappear at a threshold of about $E_V > 30$ meV, indicating a much lower threshold than in the IQH case. The data sets presented in the main text are measured at relatively

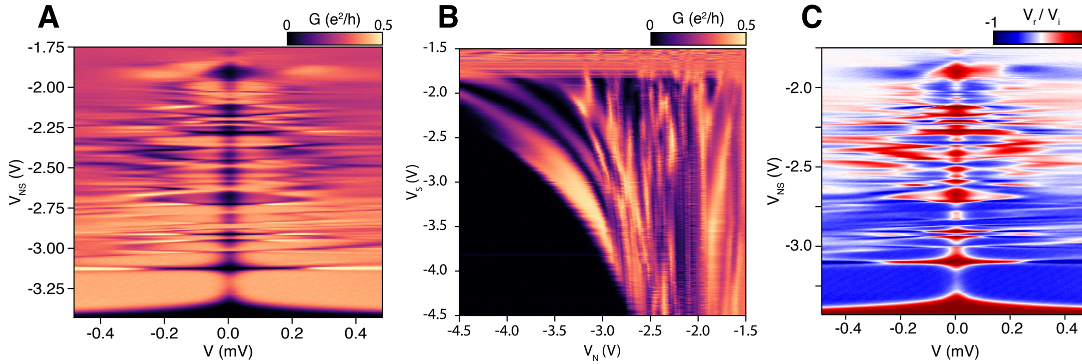

Figure C.4: **Resonances at high QPC transmission.** **(a)** The differential conductance across the 1-1/3 junction vs. North/South gate voltage V_{NS} and DC bias voltage V: B=9T, T=56mK, V_{E}=-1.460V, V_{W}=-1.775V, V_{BG}=2.0V. A large number of resonant dips and peaks arise as the voltage V_{NS} is increased, effectively widening the junction. **(b)** The zero-bias conductance G in the same regime, but varying V_{N} and V_{S} independently. Following the rationale of reference [26] we may determine the ratio of the capacitance of the local island to the North and South gates from the slope of the resonant peak trajectory: $\frac{dV_{\mathrm{N}}}{dV_{\mathrm{S}}} = -\frac{C_{\mathrm{S}}}{C_{\mathrm{N}}}$. **(c)** The ratio of the reflected voltage to the incident voltage, V_r/V_i, plotted against the DC voltage bias V, and the North/South gate voltages V_{NS} under the same conditions as panel A.

sharp confinement, similar to that of point I for the $B = 9$ T and $B = 10$ T data.

The most obvious difference between Figures C.2A and C.3A is the sheer number of features visible within the range beyond the initial conductance step, where the QPC is very "open." The presence of nontrivial structure in this regime is due to a fundamental difference between the $\nu = 1$ to $\nu = 1$ junction and the $\nu = 1$ to $\nu = 1/3$ heterojunction, with the latter involving a change in the topological order of the bulk. To explore this further, Fig. C.4A shows the differential conductance as a function of both the DC bias V and V_{NS} starting near the operating point marked I in Fig. C.3A. The data in the main text focuses on the regime near the first step (analogous to $V_{\mathrm{NS}} < -3.25V$ in Fig.C.4A). However, extending the range of V_{NS} reveals additional structure. Throughout the plot, the conductance dips nearly to 0 several times near $V = 0$. Notably, the first several low-bias dips are reminiscent of the initial conductance step analyzed in the main text, where the nonlinearity results from the chiral Luttinger liquid nature of the $\nu = 1/3$ edge.

An appealing narrative is that at least the first several resonances arise intrinsically, from reconstruction within the point contact, resulting in a single re-entrant resonant scatterer with similarly universal physics[123].

We may test this idea by independently varying V_N and V_S, shown in Fig.C.4B. From this data, it is evident that the first several features follow curved trajectories in V_N vs. V_S, as expected for a scattering center that varies its position strongly with gate voltages. This is consistent with an intrinsic effect tied to reconstruction, where the scatterer is pinned to the saddle point in the applied potential (see [26] for a similar analysis). To further explore the role of resonant scattering, Fig. C.4C shows the voltage of the reflected $\nu = 1/3$ edge, measured in the same configuration shown in Fig. C.4A. V_r/V_i attains a negative value at finite bias even when the low-bias conductance is suppressed, both on the initial conductance step discussed in the main text but also between the first few resonances; indeed after the first resonance a nearly quantized $V_r/V_i \approx -1/2$ is again observed.

As the QPC is opened further, additional conductance dips appear accompanied by their own strong nonlinearities. For $V_{NS} \gtrsim -2.75V$, these features show little curvature in $V_\mathrm{N} - V_\mathrm{S}$, and seem to depend more strongly on V_N than V_S. This is consistent with scattering mediated by extrinsic disorder centers that are fixed in space. Concomitant with the onset of these features, the conductance at high bias tends toward $G = e^2/3h$ (rather than $e^2/(2h)$), and V_r becomes positive even at high bias.

The behavior we observe for the open junction is qualitatively consistent with theoretical models, such as those proposed in Ref. [111]. In the integer quantum Hall case (Fig. C.2), a fully open QPC is equivalent to a uniformly doped macroscopic sample: there is no communication between chiral edge states on opposite edges, and the conductance is quantized at $G = \frac{e^2}{h}$ for arbitrary junction width. In contrast, in the fractional case of Figs. C.3 and C.4, opening the QPC more widely simply leads to an "edge state"

following a vertical trajectory through the center of the QPC. Equilibration between the integer and fractional quantum Hall edge states is necessarily going to be sensitive to the presence of localized scatterers along this boundary. In the wide junction limit, the presence of multiple, possibly coherent scattering processes complicates analysis of the tunneling process, restoring the 'line junction' limit first explored by Refs. [85, 37].

The high-bias behavior of the junction as more scattering centers are added, whether intrinsic or disorder driven, is well captured by theoretical models proposed in Ref. [111]. In fact, the transition from a high bias saturation of $G = \frac{e^2}{2h}$ to $G = \frac{e^2}{3h}$ as the number of scattering sites goes from one to many, is a physical demonstration of the physics which causes disequilibrium between integer quantum Hall (IQH) edge modes and FQH edge modes in high magnetic field graphene transport contacts. Typical boundaries between dual graphite gated and single graphite gated regions within a device host only a few sites where the incident IQH edge modes can strongly couple to the FQH edge modes. This results in the typically poor Hall resistance quantization seen in many graphene edge state transport experiments in the low temperature, high magnetic field limit. As can be observed in Fig.C.4A, a countable number of resonant scatterers may be observed to cause a transition between a saturation conductance of $G = e^2/2h$ and $e^2/3h$. As such, the effect of adding only a few additional disorder sites at the IQH and FQH interface in the contact (as we do purposely by adding etched trenches in each contact, see Fig.3.18A) can serve to significantly improve bulk Hall transport quantization in the FQH regime.

C.5 DC Voltage Transformer from FQH Andreev Scattering

A true DC voltage step-up transformer cannot be realized using the same approach as standard AC voltage transformers, which rely on Faraday's law of induction, without relying on the use of AC/DC interconversion. As such more exotic effects must be used to pursue a design of this type - one design proposed and realized in the 1960s by Giaever utilized the drag between vortices in parallel type-II superconducting films [125]. Subsequent proposals suggest exploiting the Coulomb drag in parallel semiconducting wells, either at zero magnetic field or in bilayer quantum Hall systems [124]. Here, following a proposal by Halperin [121], a DC voltage transformer is realized using a different approach which makes use of the dissipationless current-splitting action of the FQH Andreev process.

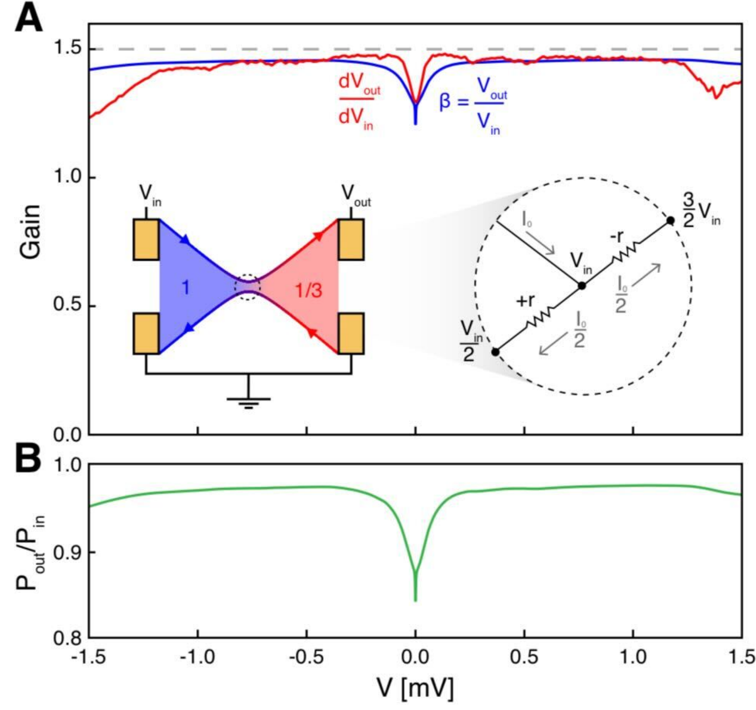

Figure C.5: **Zero frequency voltage step-up transformer.** **(A)** The differential gain $dV_\mathrm{o}/dV_\mathrm{i}$ and resulting integrated DC gain $\beta = V_\mathrm{o}/V_\mathrm{i}$, measured in the configuration shown in the inset, with B=9T, T_probe=48mK, V_E=-1.460V, V_W=-1.775V, V_NS=-3.225V, V_BG=2.0V. The FQH Andreev scattering process yields an enhancement of the output voltage on the FQH side [121], with the DC gain predicted to reach a value of 1.5 in the dissipationless limit. Experimentally, we find a gain $\beta = 1.46$, despite the nonlinearity at low bias arising from the suppression of the Andreev scattering at low energies. **(B)** The DC power dissipation ratio, calculated from β via $P_\mathrm{out}/P_\mathrm{in} = (2\beta/3)^2 - (2\beta/3) + 1$, is plotted versus V, and reaches a maximum value of 97.6% [124].

The microscopic picture of the FQH Andreev scattering process illustrated in the main text applies when a current is incident on the junction from the FQH side. When a voltage bias is applied on the IQH side of the junction, however, the equivalent scattering process is described by one in which two electrons incident on the junction split, with one transmitted to the FQH side and one reflected to the IQH side[112]. Importantly, this is a correlated scattering process, which has the effect of evenly splitting the incoming current

from a single quantum conduction mode without the introduction of any dissipation. This is in stark contrast to, for example, the case of a conventional QPC junction tuned to partial transmission of a single mode, where the transmission probability $0 < P < 1$ of the incoming particles creates fluctuations in the transmitted current, resulting in a nonzero amount of dissipation.

FQH Andreev process enforces an outgoing distribution of currents and voltages which may be modeled by a Y-junction with resistances $+R_K$ and $-R_K$ (R_K is the von Klitzing constant, h/e^2) on the outgoing legs of the junction, illustrated by the effective circuit model in the inset of Fig. C.5A. Currents outside of the junction flow dissipationlessly in the chiral edge channels. With one of the resistors being negative, the circuit operates not as a voltage *divider* but as an *amplifier*, since the negative resistance causes the current through the $-R_K$ leg to flow from low voltage to high voltage.

This is identical to the principle used in some standard AC voltage amplifiers, which exploit the negative *differential* resistance of a tunnel-diode. In such circuits, a DC voltage bias is applied to the tunnel-diode to achieve a small-signal negative resistance ($\partial v/\partial i < 0$). When a voltage is applied across a standard resistor and the tunnel-diode in series, the negative differential resistance of the tunnel-diode causes an amplification of the voltage between the two elements—an extraordinary property of the FQH Andreev Junction is that its effective circuit description contains a component of negative *absolute* resistance, so it can act as an amplifier even in the DC limit. The effectively negative-resistance component cannot, of course, exist in isolation, since Joule's law would predict that it acts as a source of power: $P = I^2R < 0$! In the effective circuit, the resistance $-r$ must be paired with a resistance $+r$ such that the same amount of power generated by the negative resistor is fully dissipated by the positive resistor. It should be kept in mind that this circuit is merely an effective model of the behavior resulting from the local FQH Andreev scattering process—in reality, no part of the device is generating nor

dissipating power in this process.

C.6 Data Analysis

C.6.1 Effects of cryogenic electronic filters

The measurements presented in this paper were performed in a dilution refrigerator setup with a base temperature of 56 mK. To improve thermalization of the electron system to the phonon bath, we heavily filter the measurement wires. However, these filters give a finite contribution to the measured value of G that must be corrected for to give quantitatively reliable results. In this section we describe how the true conducatance is extracted from the measured voltages and currents at room temperature.

All measurements were performed using standard lock-in techniques with an excitation frequency of $f = 2.74\,\text{Hz}$. In order to extract the differential tunneling conductance we measure $G \equiv I/V_D$, shown schematically in Fig. 1B. We source current via C3 on the $\nu = 1/3$ side of the junction and measure the output current at C7 through the Ithaco 1211 transimpedance amplifier. The diagonal voltage V_D is extracted by measuring the voltage drop between C4 and C8 with an SR560. The Ithaco is modeled as a perfect ammeter, while the SR560 is treated as a perfect voltmeter. Furthermore, we assume – due to the chiral nature of the edge states – that upstream contacts from the source do not contribute to the cross-device conductance. The equivalent device circuit schematic is given in Fig. C.6A. Each device contact is effectively connected to room temperature instrumentation, or ground, via a two-stage low-pass RC filter; while there are RF low-pass Pi filters, they have small component values and can be ignored in the low-frequency limit. While only C3 and C4 contribute on the $\nu = 1/3$ side of the junction (C2/C1 are upstream), C5/C6 are downstream of the source and must be included as floating con-

tacts on the $\nu = 1$ side of the junction. Tunneling at the heterojunction is modeled as a resistor labeled R_{DUT} which should be considered as voltage bias dependent.

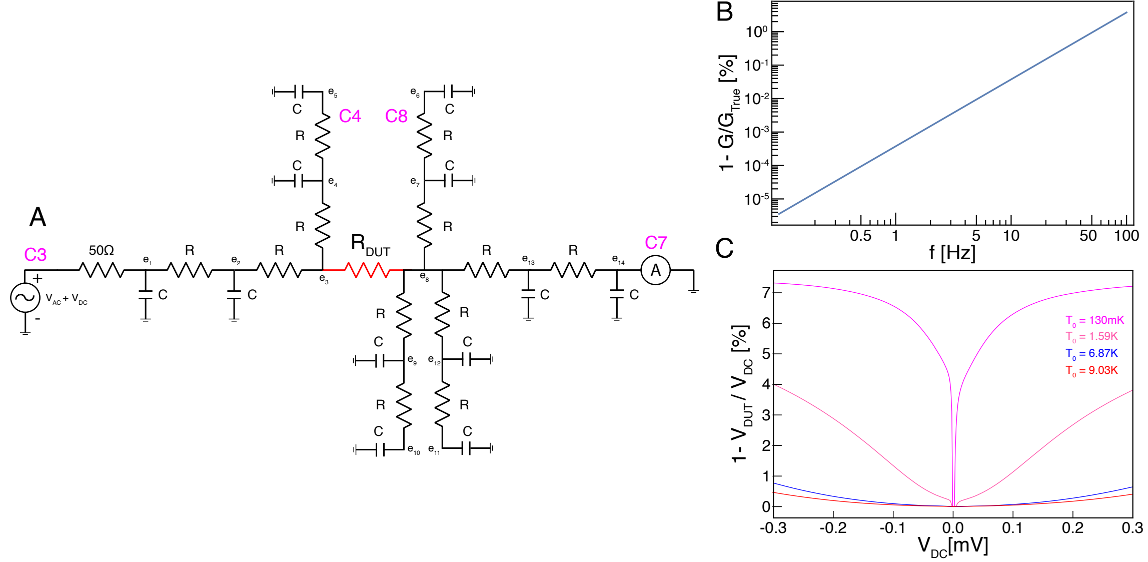

Figure C.6: **Measurement circuit including electronic filters.** **(a)** Model of the sample plus the electronic low-pass filters attached to each contact. Here $R = 1k\Omega$ and $C = 20\text{nF}$. **(b)** Percentage deviation of the measured value of the conductance $G \equiv \text{Re}[e_{13}]/(R{\cdot}\text{Re}[e_5 - e_6])$ to the true value of the conductance G_{true}. **(c)** Percentage deviation of the corrected bias voltage (V_{DUT}) from the applied bias voltage (V_{DC}) versus V_{DC}. The value of this deviation is plotted for each of the curves given in the main text Fig. 3C.

Given the extra components surrounding R_{DUT}, it is not guaranteed for every frequency that an AC four-terminal measurement will provide an accurate measure of the true differential conductance, G_{true}. Using the notation defined in Fig. C.6A, $V_D \equiv \text{Re}[e_6 - e_5]$, and $I \equiv \text{Re}[(e_{13} - e_{14})]/R \approx \text{Re}[e_{13}]/R$. At our measurement frequency of $f = 2.74\,\text{Hz}$, it can be shown by solving the set of Kirchoff's laws – set by the schematic in Fig. C.6A – that $G \equiv I/V_D = \text{Re}[e_{13}]/(R \cdot \text{Re}[e_6 - e_5])$ is a good approximation to G_{true}. The percentage error, $\eta \equiv 100\frac{G_{\text{true}} - G}{G_{\text{true}}}$, is plotted for a fixed value of $G_{\text{true}} = 10^{-3}e^2/h$ in Fig. C.6B versus frequency. While $G \approx G_{\text{true}}$ for sufficiently low frequencies, η scales as f^2, and quickly grows to be large; additionally η decays monotonically with increasing G_{true} so the value of η with $G_{\text{true}} = 10^{-3}e^2/h$ represents a good

upper-bound on the error given the resistance ranges in our measurement. For $f > 75\,\mathrm{Hz}$, η becomes greater than 1% even for values of $G_{\mathrm{true}} \gg e^2/h$. Consequently, we chose to measure at a frequency significantly lower than this threshold such that any reduction in f resulted in an experimentally undetectable change in G, and so that we could safely assume $G \approx G_{\mathrm{true}}$ over a wide range of conductance values.

While at $f = 2.74\,\mathrm{Hz}$, four-terminal measurements of G remain a good approximation of G_{true}, the DC voltage bias across R_{DUT} requires some additional analysis. In order to investigate the DC bias directly across the sample it is necessary to take into account the filter resistances since they inherently form a voltage divider between themselves and R_{DUT}. Determining the relationship between the applied DC voltage at the input of the filters (a known value defined as V_{DC}) and the voltage bias across the sample, defined as V_{DUT}, is straightforward. At low frequencies, the current drawn to the floating contacts is negligible so the DC voltage across the sample is well approximated by

$$V_{\mathrm{DUT}} = V_{\mathrm{DC}} - (4R + 50\Omega) \cdot I \tag{C.5}$$

where I is the DC current through R_{DUT}. While the DC current is not known a priori, differentiating with respect to V_{DUT} the above equation gives:

$$1 = \frac{\mathrm{d}V_{\mathrm{DC}}}{\mathrm{d}V_{\mathrm{DUT}}} - (4R + 50\Omega)\frac{\mathrm{d}I}{\mathrm{d}V_{\mathrm{DUT}}} \tag{C.6}$$

This equation can be rearranged to isolate $\mathrm{d}V_{\mathrm{DUT}}$ and $\mathrm{d}V_{\mathrm{DC}}$, given below.

$$\mathrm{d}V_{\mathrm{DUT}} = \frac{\mathrm{d}V_{\mathrm{DC}}}{1 + (4R + 50\Omega)\frac{\mathrm{d}I}{\mathrm{d}V_{\mathrm{DUT}}}} \tag{C.7}$$

The differential conductance, $G_{\mathrm{true}} = \mathrm{d}I/\mathrm{d}V_{\mathrm{DUT}} \approx G$, appears in the denominator. Integrating this equation leaves the final correction formula, which can be expanded for

$4050\Omega \cdot G \ll 1$ to give:

$$V_{\mathrm{DUT}} = \int_0^{V_{\mathrm{DC}}} \frac{\mathrm{d}V'_{\mathrm{DC}}}{1 + (4R + 50\Omega) G_{\mathrm{true}}(V'_{\mathrm{DC}})} \approx V_{\mathrm{DC}} - (4050\Omega) \int_0^{V_{\mathrm{DC}}} \mathrm{d}V'_{\mathrm{DC}} G(V'_{\mathrm{DC}}) \quad \text{(C.8)}$$

While in general this correction remains small for low conductance values, indicating the bias voltage in the range where universal power-law behavior is observed is unaffected, for measurements where the conductance is large for the entire bias-dependence the corrections can be significant. The effect of this correction is plotted in Fig. C.6C corresponding to the tunneling data presented in Fig. 3C. For the largest values of T_0, i.e, $T_0 = 6.87\,\mathrm{K}$ and $T_0 = 9.02\,\mathrm{K}$ respectively, the corrected bias remains less than 1% of the applied bias voltage. However, for lower values of T_0 this correction becomes significant.

C.6.2 Determining the theoretically expected range of universal power-law scaling

For sufficiently low temperatures and bias voltages, the Lagrangian in Eq. (1) is expected to flow to the weakly coupled fixed point where $G \propto V^2, T^2$. However, while in this regime where the temperature and bias dependence is expected to be universal and irreverent of microscopic details, the range over where this behavior persists does care about the sample specifics. Even in the most ideal case, where Eq. (1) describes the system for *all* bias voltages and temperatures, the range where the $O(V^2, T^2)$ terms in Eq. (2) dominate is determined by the bare value of Γ. As such, when extracting the power-law exponents and assessing the quality of the scaling collapse it is important to not over-extend the fitting range beyond where universality is expected, i.e, where $G \propto V^2, T^2$. In general, while the cross over from weak to strong coupling predicts de-

viations from $G \propto V^2, T^2$ behavior at sufficiently high energies, additional perturbations in Eq. (1) will generally reduce the range where universal behavior may be expected. Consequently, the bias voltages and temperatures given by the quantum impurity model where significant deviations from $G \propto V^2, T^2$ are predicted provides a self-consistent range where power law behavior should be observed.

For our fridge base temperature of $T_{\text{probe}} = 56\,\text{mK}$, we may evaluate the threshold bias voltage V_{Th} above which the conductivity predicted by Eq. (2) exceeds the conductivity given by the full quantum impurity model (Eq. (3)) by more than 5%. For a simulated temperature of $T = 56\,\text{mK}$, when $T_0 = 9\,\text{K}$, $V_{\text{Th}} \approx 170\mu V$. Consequently, in order to extract T_0 for the data presented in Fig. 1C, T_0 is initially guessed to be 9 K. T_0 is then fit over a range of $V = 15\,\mu\text{V}$ to $V = 170\,\mu\text{V}$. The fit results in a $T_0 = 9.020(7)\,\text{K}$, which does not effectively change the fitting range given a bias step of $5\,\mu\text{V}$ per data point. This procedure leads to a self-consistent result where both T_0 and the range over which T_0 is fit simultaneously converge.

We may also consider the scaling collapse in Fig. 1F, which in particular, is only valid when $T << T_0/2\pi$. The experimental scaling collapse data is repeated in Fig.C.7A and may be directly compared to Fig.C.7B showing the theoretically predicted scaled conductance for a $T_0 = 6.87\,\text{K}$ for the same temperature values used in the experimental scaling collapse. The scaling collapse begins to fail under two conditions; $eV >> k_bT$, and $T >> T_0/2\pi$. From Fig.C.7B it is clear that at low voltage bias, the curves are expected theoretically to collapse on to each other well up to $T = 550\,\text{mK}$, then are predicted to deviate from the low-energy prediction of Eq.(2) at higher temperatures. Additionally, all the curves regardless of temperature deviate from Eq.(2) at sufficiently high bias. In direct comparison to Fig.C.7B, the the onset of deviations from from Eq.(2) in both temperature and voltage bias in the experimental data in Fig.C.7A are well capture by the theoretical model to within experimental uncertainty.

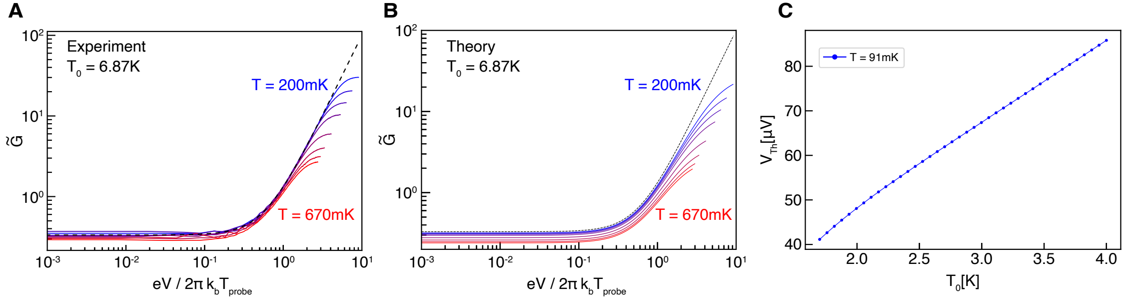

Figure C.7: **Analysis of Deviations from Universal Luttinger Liquid Behavior.** **(a)** The scaled conductance $\widetilde{G} = \frac{2h}{e^2}(\frac{T_0}{2\pi T})^2 G$ versus the scaled voltage bias $eV/2\pi k_b T$ as in the main text Fig. 1F (temperature values are listed in the caption of Fig. 1). **(b)** Theoretically predicted scaled conductance $\widetilde{G}$ versus $eV/2\pi k_b T$. Here $\widetilde{G}$ is computed the same way as in panel (a), however, the unscaled conductance is computed from the conductance in Eq. (3) from the full quantum impurity model. Black dashed line is the theoretical curve for the low energy scaled conductance: $\widetilde{G} = 1/3 + x^2$. $T_0 = 6.87K$ and the values of T are kept the same as in panel (a). **(c)** The threshold voltage V_{Th} below which the Sommerfeld expansion of $O(V^2, T^4)$ of Eq. (3) (given in Eq.(C.9)) is expected to be valid for a fixed $T = 91\,\mathrm{mK}$.

In general, as $T_0 \sim T/2\pi$ for the lowest experimentally accessible temperatures, Eq. (2) will no longer be an accurate model of the system for any range of voltage bias. However, it may be observed that the data presented in Fig. 3C with $T_0 = 1.59\,\mathrm{K}$ does have a V^2 dependence for some substantial range of V despite $T_0/2\pi \approx 250\,\mathrm{mK}$ being sufficiently close to the lowest available electron temperatures. This can be understood by computing the Sommerfeld expansion of Eq. (3) to $O(V^2, T^4)$, given in Eq. (C.9).

$$G(V,T) = \left[\frac{1}{6}(\frac{2\pi T}{T_0})^2 - \frac{7}{30}(\frac{2\pi T}{T_0})^4\right] + \left[\frac{1}{2} - (\frac{2\pi T}{T_0})^2 + \frac{7}{2}(\frac{2\pi T}{T_0})^4\right](\frac{eV}{k_b T_0})^2 \tag{C.9}$$

V_{Th}, now calculated as the bias voltage above which the conductivity predicted by Eq. (C.9) differs from that predicted by Eq. (3) by more than 5%, is given in Fig. C.7B for a fixed simulated temperature of $T = 91\,\mathrm{mK}$ versus T_0. It is clear that even for a moderate temperature of 91 mK, the range of V where a quadratic bias dependence is expected is significant. While the conductivity in Eq. (C.9) is still entirely parameterized

by a single value T_0, the curvature of the bias depdence is weakly temperature dependent. This becomes relevant when attempting to calculate T_0 from the low-energy bias dependence for the data presented in Fig. 3C with $T_0 \sim 1.6K$.

C.6.3 Extracting power-law exponent

It is clear from the inset of Fig. 1C that the bias dependence appears to be well fit by parabola, with a curvature leading to a $T_0 \approx 9\,\text{K}$. However, one would like to asses the power law exponent and its uncertainty while allowing T_0 to vary. Given that we can determine the approximate range over which $G \propto V^2$ behavior would be expected, given a rough value of T_0, we can directly measure the power-law exponent and check for self-consistency. Fig. C.8A shows the same data in Fig. 1C; the two gray circles mark the range over which the scaling exponent is extracted. The upper bound of this range is set by the curvature of the bias dependence, $T_0 \approx 9\,\text{K}$, which can be seen from Fig.C.7A, at a temperature $T_{\text{probe}} = 55\,\text{mK}$, is about $170\,\mu\text{V}$. The lower bound, $V = 15\,\mu\text{V}$, is set by signal to noise. To asses the quality of the power-law behavior over this range, we take the finite-difference of $\log(G - G_{\text{min}})$ and divide it by the finite-difference of $\log(V)$. This is plotted in Fig. C.8B versus data point index; the data is passed through a 10-point digital rolling average filter in order to reduce the noise generated by taking a numerical derivative. If the system is well described by a power law, the value of $\mathrm{d}\log(G - G_{\text{min}})/\mathrm{d}\log(V)$ should be a constant. It is clear that the data in Fig. C.8B is well approximated by a constant and the extracted fit value, γ, over the bias range highlighted in Fig. C.8A yields $\gamma = 1.997 \pm 0.055$. This indicates that fitting the data in Fig. C.8A to a quadratic defined as $G(V) - G_{\text{min}} = \frac{1}{2}(\frac{eV}{k_b T_0})^2$ to extract T_0 precisely is self-consistent.

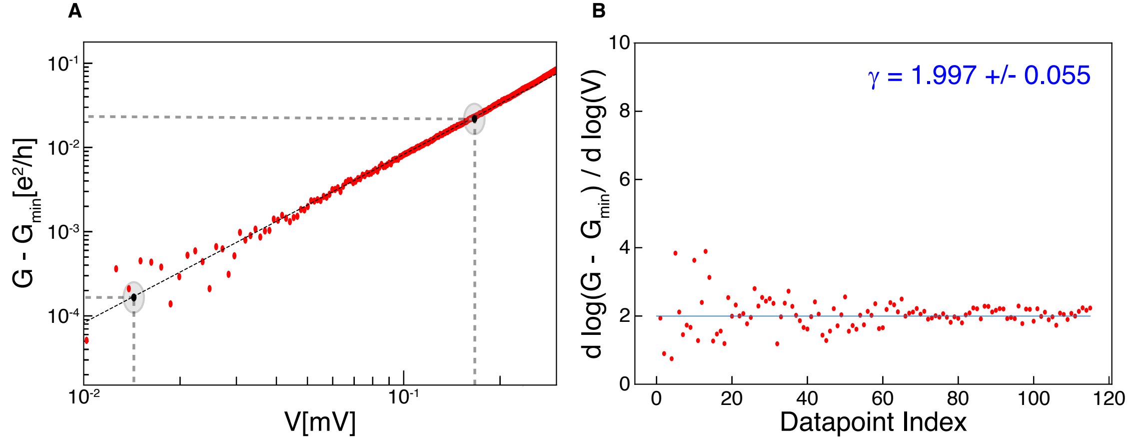

Figure C.8: **Computing power law exponent from the voltage bias-dependence (a)** $G - G_{\text{min}}$ as in Fig 1C. Points marked by gray circles indicate upper and lower bounds of included data ($V \in [15\,\mu\text{V}, 167\,\mu\text{V}]$) used to extract power-law exponent. **(b)** Derivative of the log of $G = G - G_{\text{min}}$ divided by the derivative of the log of V versus data point index. Data is fit to a constant which is plotted as the dashed blue line. The exponent is found to be $\gamma = 1.997 \pm 0.055$

C.6.4 Extracting the low-energy value of T_0 for comparison to the quantum impurity model

The four line cuts presented in Fig. 3C represent tunneling spectra each individually associated with a T_0 which varies by nearly two orders of magnitude between the data sets. Based on general renormalization group arguments, the Lagrangian given in (1) becomes a better approximation to the system at low voltage biases and temperatures, relative to the energy scale set by $T_0 \propto 1/\Gamma$ [31]. While a lower-bound on T is set by cryogenic instrumentation, V can be made nearly arbitrarily small. So generally, the low-bias regime of each data set in Fig. 3C is where Eq. (1) is likely to be an accurate model of the system.

In principle, at low voltage bias, a perturbative expansion like that in Eq. (2) or Eq. (C.9) should produce the same behavior as the full quantum impurity model in this regime within some accuracy threshold. As a result, the T_0 which parameterizes the

low-energy behavior also parameterizes the entire bias-dependence if Eq. (1) holds up to the strong coupling limit. The converse of this, is that while Eq. (1) may be accurate at low voltage bias, the effect of additional operators (like electron co-tunneling) may cause deviations from the full quantum impurity model at high-bias. This way we may assess how well the data in Fig. 3C agrees with the full quantum impurity model. We extract T_0 from the low-energy (voltage bias) region of the curve, and the same T_0 can then be used to interpolate between the weak and strong coupling regimes via Eq. (3). While these curves are all taken at a fixed electronic temperature $T_e = 91\,\mathrm{mK}$, the large variance in T_0 implies that even the low-bias regime of each curve requires careful treatment in order to be an accurate low-energy expansion of Eq. (3).

For all curve fits, a systematic zero-bias shift of $2.5\,\mu\mathrm{V}$ is accounted for. For the data sets with the largest values of T_0 in Fig. 3C, i.e, $T_0 = 9.02\,\mathrm{K}$ and $T_0 = 6.87\,\mathrm{K}$ respectively at a base temperature of $T = 56\,\mathrm{mK}$, there is a significant bias range where Eq. (2) is accurate. In this regime at low bias, T_0 is directly related to the curvature of the bias-dependence and is temperature independent; consequently T_0 can be fit agnostic of the electronic temperature for these two data sets by subtracting the residual conductance and fitting the resulting parabola (as shown in Fig. 1C). As is mentioned in the main text, for these values of T_0, all of the temperature dependence falls in the residual conductance when $V = 0$ and we utilize this to realize a sensitive primary thermometer, using the $T_0 = 9.02\,\mathrm{K}$, to accurately extract the electron temperature, $T_e = 91\,\mathrm{mK}$. This measured electronic temperature then becomes an input parameter to the remaining data sets in Fig. 3C. The success of this procedure can be seen in Fig. 3C where the zero-bias conductance value is well predicted for the $T_0 = 6.87\,\mathrm{K}$ data (where T_0 is extracted from the curvature of G agnostic of T_e) given the measured value of T_e.

However, for the curve with $T_0 \approx 1.6\,\mathrm{K}$ Eq. (2) will not be accurate even when $V = 0$ when $T = 91\,\mathrm{mK}$. However, Fig. C.7C shows that the Sommerfeld expansion in

Eq. (C.9), for a temperature of 91 mK, even with $T_0 \approx 1.6K$ will be within 5% of the full quantum impurity model for $V < 45\,\mu$V. To extract T_0, we fit this data set to the Sommerfeld expansion (in a range between $-45\,\mu$V and $45\,\mu$V) given in Eq. (C.9), where $T = T_e = 91$ mK resulting in a fit value $T_0 = 1.59(1)$ K. For the final data set in Fig. 3C, with $T_0 \approx 130$ mK, it is clear from Fig. C.7C that even the Sommerfeld expansion will not be accurate even for $V = 0$ in this regime. The only way to systematically extract T_0 from this data set is to directly fit the data to Eq. (3) where $T = T_e = 91$ mK. Following this procedure, $T_0 = 132(2)$ mK, and the low bias regime is well fit by this value while some deviation is observed at high-bias, further emphasizing that for low biases and temperatures, even for extremely low values of T_0, the system is governed by the Lagrangian in Eq. (1) to a high degree of accuracy.

C.7 Additional Data at a different magnetic field

We present here additional tunneling data at $B = 9$ T between the $\nu = 1/3$ and $\nu = 1$ edges. All of the features presented in the main text are reproduced at a different magnetic field and set of gate voltages; this includes both the weak coupling universal scaling behavior, the strong coupling Andreev reflection of fractionalized quasiparticles, and near agreement with the full quantum impurity model. Notably, in this data set at $B = 9$ T and the data presented in the main text at $B = 10$ T, the west side of the junction sits at different locations within the $\nu = 1/3$ plateau. Figure C.11 shows the two terminal conductance as a function of V_W, with $V_{BG} = -2V$, for both the 9T data set presented here, and the 10T data presented in the main text. Point I corresponds to the gate voltages at which the tunneling data were measured at $B = 10T$ in the main text, and point II corresponds to the regime of the data in Figure C.9. The agreement between the measured exponents demonstrates the repeatability of the tunneling behavior

for varying configurations of the junction parameters including voltage bias, temperature, T_0, and electron density within the $\nu = 1/3$ plateau.

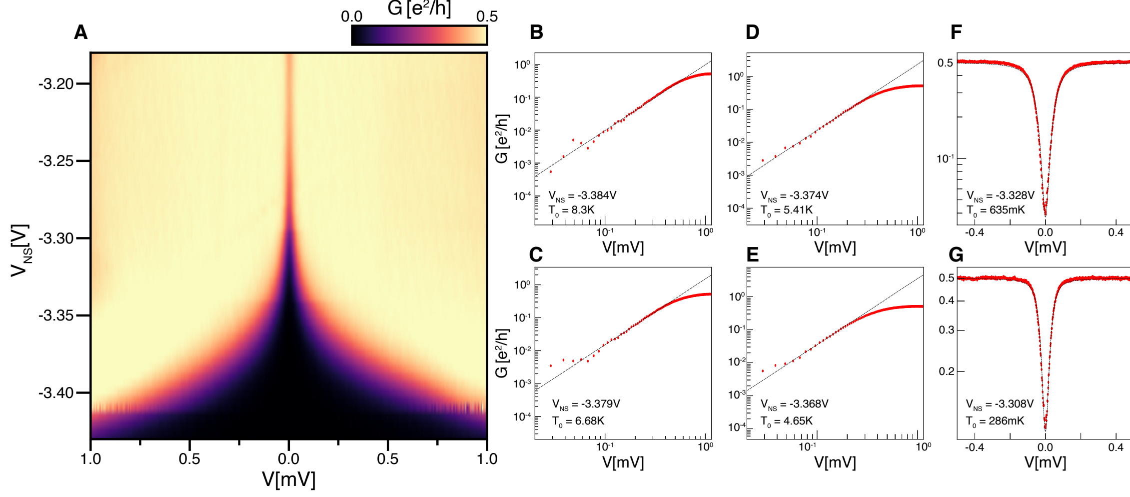

Figure C.9: **Bias dependence of tunneling data between 1/3 and 1 QH edges at B = 9T. (a)** G plotted as a function of voltage bias V and North/South gate voltage $V_{\rm NS}$. The other gates are held at fixed voltages: $V_{\rm BG} = 2V$, $V_{\rm E} = -1.46V$, $V_{\rm W} = -1.775$. (**B-E**) Line cuts of panel A at different values of $V_{\rm NS}$ plotted on a log-log scale. Data points are averaged together in windows of 160 points and a systematic zero-bias shift of $5\,\mu$V is removed. Black dashed lines are fits to $G = \frac{1}{2}(\frac{eV}{k_b T_0})^2$; the fit value of T_0 inset within each plot. The power-law behavior extracted from the line cuts of panel A were not taken with enough averaging to distinguish $G(V = 0)$ from 0. Consequently, panels B-E were fit over a half-decade of bias where the lower bound was set by where the V^2 term is expected to dominate over the constant offset in Eq. (2). **(F-G)** Additional line cuts of panel A at two distinct values of $V_{\rm NS}$ plotted on a semi-log scale. Black dashed line is a fit to the conductivity predicted by the full quantum impurity model given in Eq. (3). The fitted values of T_0 are inset in each plot.

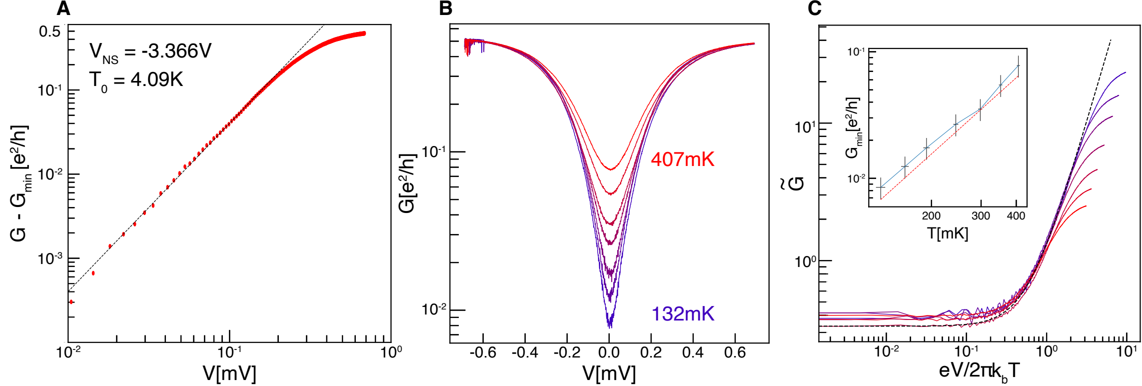

Figure C.10: **Scaling collapse of tunneling data between 1/3 and 1 QH edges at B = 9T.** **(a)** $G-G_{\mathrm{min}}$ plotted versus V for $V_{\mathrm{NS}}=-3.366V$. The black dashed line represents the fit to the function $\frac{1}{2}(\frac{eV}{k_b T_0})^2$, yielding a fit $T_0=4.09\,\mathrm{K}$. **(b)** G plotted versus V for the probe temperatures: 132 mK, 161 mK, 192 mK, 244 mK, 298 mK, 352 mK, 407 mK. **(c)** Same curves as in panel B, but the conductance is scaled such that $\widetilde{G}=2G(\frac{T_0}{2\pi T_{\mathrm{probe}}})^2(\frac{h}{e^2})$, and is plotted against $eV/(2\pi k_b T_{\mathrm{probe}})$ where $T_0=4.09\,\mathrm{K}$ is extracted from the bias dependence shown in panel A. Inset is $G(V=0)\equiv G_{\mathrm{min}}$ plotted against the probe temperature on a log-log scale. A rough T^2 dependence is observed between $T=132\,\mathrm{mK}$ and 407 mK. The red dashed line corresponds to $G(V=0)=\frac{1}{2}(\frac{eV}{k_b T_0})^2$, with $T_0=4.09\,\mathrm{K}$. Error bars are computed assuming a current uncertainty of $\pm 500\,\mathrm{fA}$ and a voltage uncertainty of $\pm 100\,\mathrm{nV}$, as well as a temperature uncertainty of $\pm 5\,\mathrm{mK}$. While the curves collapse onto each other well, a small systematic deviation between the collapsed data set and the prediction of Eq. (2) is observed. This may be attributed to a systematic scaling in the zero-bias conductance as a result of insufficient averaging times near zero-bias for a fixed gate-sweep rate.

C.8 Excess Conductance Observed in IQH-FQH Heterojunctions with $\nu_{FQH}<1/2$

The main text describes a systematic investigation of the overshoot in conductance across the heterojunction to $G_D=1/2e^2/h$ when the filling factors are set to $\nu_E=1$ and $\nu_W=1/3$. We also find that the overshoot to $G_D=1/2e^2/h$ persists for several other FQH filling factors below $\nu=1/2$, which is expected if the outermost edge mode in these

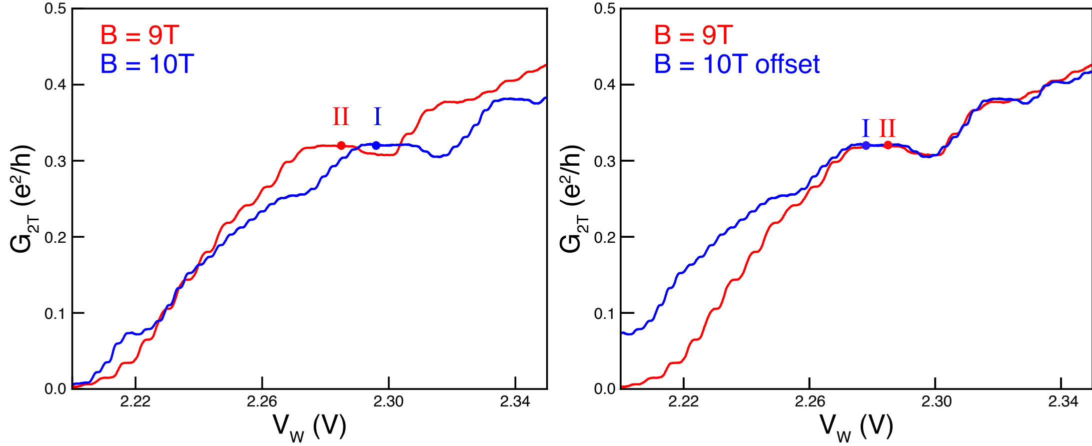

Figure C.11: **Comparison of location within the $\nu = 1/3$ plateau for 9T and 10T data.** **(a)** Two terminal conductance on the W side at B=10T and B=9T, $V_{BG} = -2V$, with point I and II indicating the locations within the plateau at which tunneling data were taken for the main text (I) and Figs. C.9 and C.10 (II). **(b)** Same as in panel a, but with 10T data shifted to the left by 18mV to make the different locations within the 1/3 plateau between the two data sets more apparent.

states remains a chiral Luttinger liquid with the same characteristics of the $\nu = 1/3$ edge. In particular, Figure C.12A shows the maximum G_D across the junction while varying V_{NS} to tune the QPC from completely pinched off to completely open. This is repeated while varying V_W across the range shown in Figure C.12B to tune the filling factor ν_W from 1/3 to 2/3. The full conductance data are plotted in Figure C.12C, from which the maximum values were extracted to plot in Figure C.12A.

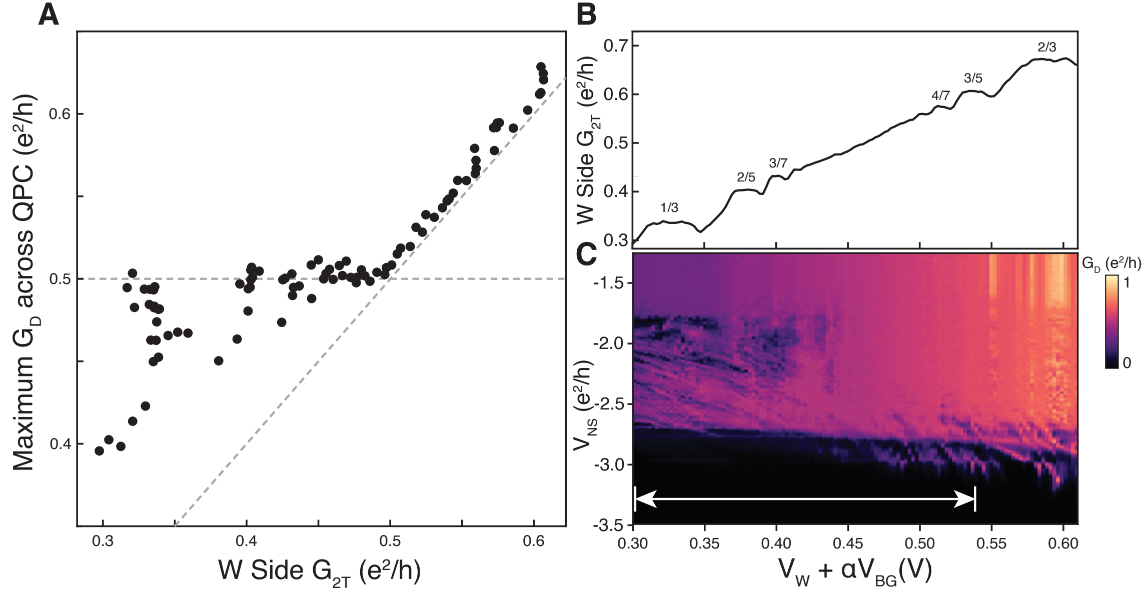

Figure C.12: **The maximum conductance across the junction from $\nu_E = 1$ to variable $\nu_W < 1$.** **(A)** On the x axis is plotted the two terminal conductance on the W side of the device, as a proxy for the filling factor. On the y axis is the maximum value obtained of the conductance across the QPC while varying the QPC from totally pinched off to totally open using the NS gates. The dotted lines show $max(G_D) =$ West G_{2T} and $max(G_D) = 0.5e^2/h$. The max conductance saturates to $G = 1/2e^2/h$ for FQH fillings between 1/3 and 1/2 (*i.e.* 1/3, 2/5, 3/7, ...), then tracks linearly with the filling factor for $\nu > 1/2$. **(B)** The two terminal conductance G_{2T} measured on the W side of the device, as a function of $V_W + \alpha V_{BG}$, used as a proxy for the filling factor in panel A. **(C)** The raw data from which A is taken - plotted points in A correspond to the maximum conductance of each vertical slice of C. This analysis is done over the x-axis range shown by the white arrow. Outside of this range the maximum conductance even when the QPC is fully open exceeds ν, suggesting poor equilibration of the leads to the hole-conjugate FQH states 2/3, 3/5, etc.

D

Appendix D: Nanofabrication Procesess and Recipes

D.1 AFM Cutting Recipes

Here is a list of the parameters we use to perform the local anodic oxidation lithography:

1. Graphite is exfoliated onto a doped, conducting, Si wafer with a 90nm dry-chlorinated

oxide grown on top.

2. A graphite flake, typical thickness $< 5nm$, is brought into our Bruker Dimension Icon AFM.

3. The relative humidity is set between 45-50%

4. Anodic oxidation is performed with the Arrow NcPt tips purchased from Nanoandmore, with a spring constant of 42N/m, and a typical resonant frequency of about 285kHz.

5. The deflection set point is set to 0.4V

6. The excitation frequency is set to 200kHz

7. The amplitude of the voltage excitation is 9.5V

8. The tip is rastered at a rate of 2-3 $\mu m/s$

D.2 Lithography and Lift-off of Metal Finger Gates for Quantum Dots

In order to perform high resolution liftoff of metal finger gates, it is necessary to employ a thin bilayer resist which can avoid dog-ear effects but also be sufficiently thick to put down 20nm of metal. The resist features an MMA-copolymer / PMMA bilayer; the copolymer is more dose sensitive than the thin PMMA capping layer so it naturally forms a strong undercut. The details of the resist stack is given in Table D.2. It is recommended to wait 60 seconds after baking the first resist layer to allow the first layer to cool and prevent resist mixing. This recipe can be used to achieve finger gates with

an isolated minimum width of 30nm, and when written as high density lines, can be used to write 40nm finger gates at an 80nm pitch.

Layer Number	Resist	Spin Speed	Bake Temperature	Bake Time
1	COPOL:Ethyl Lactate 1:2	5000rpm	180C	5min
2	PMMA 950k:Anisole 1:7	3000rpm	180C	5min

Table D.1: Resist stack for high-resolution liftoff of quantum dot finger gates

To write the finger gates, use the JEOL 6300FS EBL system at an accelerating voltage of 100kV. The beam current should be set to 50pA using the 4th lens. In principle better resolution can be achieved using the 100pA setting with the 5th lens, however the aperture for the 5th lens is only 60μm, which makes aligned writes challenging. Exposure depends on the job, but for dense lines I used $600\frac{\mu C}{cm^2}$, and for isolated lines I used $800\frac{\mu C}{cm^2}$.

Development is done for 60 seconds in a mixed solution of MIBK:IPA 1:1 which is stored in a fridge at 10C. Development is stopped in pure IPA for 20 seconds and then the sample is blown dry with N2.

Layer Number	Metal	Deposition Rate	Thickness	Deposition Pressure
1	Chrome	0.3A/s	3nm	1E-6 Torr
2	Gold	0.5A/s	12nm	1E-6 Torr

Table D.2: Metal stack for high-resolution liftoff of quantum dot finger gates

Metalization is done with a CHA Industries SEC-600-RAP multi-wafer evaporator, and the exact metal stack used is given in Table D.2. The tooling in the evaporator is designed for continuous rotation and angled such that the evaporated metal jet is perpendicular to all substrates in the tooling. Deposition is performed manually, i.e., without an automatic deposition controller, in order to avoid extra metal deposition due to poor initial feedback immediately after the shutter opens.

Bibliography

[1] C. R. Dean, A. F. Young, I. Meric, C. Lee, L. Wang, S. Sorgenfrei, K. Watanabe, T. Taniguchi, P. Kim, K. L. Shepard, and J. Hone, *Boron nitride substrates for high-quality graphene electronics*, *Nature Nanotechnology* **5** (2010) 722–726.

[2] K. S. Novoselov, A. K. Geim, S. V. Morozov, D. Jiang, Y. Zhang, S. V. Dubonos, I. V. Grigorieva, and A. A. Firsov, *Electric Field Effect in Atomically Thin Carbon Films*, *Science* **306** (2004), no. 5696 666–669.

[3] C. R. Dean, L. Wang, P. Maher, C. Forsythe, F. Ghahari, Y. Gao, J. Katoch, M. Ishigami, P. Moon, M. Koshino, T. Taniguchi, K. Watanabe, K. L. Shepard, J. Hone, and P. Kim, *Hofstadter's butterfly and the fractal quantum Hall effect in moiré superlattices*, *Nature* **497** (May, 2013) 598–602.

[4] C. R. Dean, A. F. Young, L. Wang, I. Meric, G. H. Lee, K. Watanabe, T. Taniguchi, K. Shepard, P. Kim, and J. Hone, *Graphene based heterostructures*, *Solid State Communications* **152** (2012), no. 15 1275–1282.

[5] C. R. Dean, A. F. Young, P. Cadden-Zimansky, L. Wang, H. Ren, K. Watanabe, T. Taniguchi, P. Kim, J. Hone, and K. L. Shepard, *Multicomponent fractional quantum Hall effect in graphene*, *Nature Physics* **7** (2011), no. 9 693–696.

[6] Y. Cao, V. Fatemi, S. Fang, K. Watanabe, T. Taniguchi, E. Kaxiras, and P. Jarillo-Herrero, *Cao*, *Nature* **556** (Apr., 2018) 43–50.

[7] A. F. Young and L. S. Levitov, *Capacitance of graphene bilayer as a probe of layer-specific properties*, *Physical Review B* **84** (Aug., 2011) 085441.

[8] A. F. Young, C. R. Dean, I. Meric, S. Sorgenfrei, H. Ren, K. Watanabe, T. Taniguchi, J. Hone, K. L. Shepard, and P. Kim, *Electronic compressibility of layer-polarized bilayer graphene*, *Physical Review B* **85** (2012), no. 23 235458.

[9] A. F. Young, Y. Zhang, and P. Kim, *Experimental Manifestation of Berry Phase in Graphene*, in *NanoScience and Technology* (H. Aoki and M. S. Dresselhaus, eds.), pp. 3–27. Springer International Publishing, 2014.

[10] A. A. Zibrov, C. Kometter, H. Zhou, E. M. Spanton, T. Taniguchi, K. Watanabe, M. P. Zaletel, and A. F. Young, *Tunable interacting composite fermion phases in a half-filled bilayer-graphene Landau level*, *Nature* **549** (Sept., 2017) 360–364.

[11] R. L. Willett, R. R. Ruel, K. W. West, and L. N. Pfeiffer, *Experimental demonstration of a Fermi surface at one-half filling of the lowest Landau level*, *Physical Review Letters* **71** (Dec., 1993) 3846–3849.

[12] C. Nayak, *Microsoft has demonstrated the underlying physics required to create a new kind of qubit*, Mar., 2022.

[13] A. Assouline and et al., *Energy gap of the even-denominator fractional quantum hall state in bilayer graphene*, *Phys. Rev. Lett.* **132** (January, 2024).

[14] A. A. Zibrov, E. M. Spanton, H. Zhou, C. Kometter, T. Taniguchi, K. Watanabe, and A. F. Young, *Even-denominator fractional quantum Hall states at an isospin transition in monolayer graphene*, *Nature Physics* **14** (Sept., 2018) 930–935.

[15] X. Huang, T. Wang, S. Miao, C. Wang, Z. Li, Z. Lian, T. Taniguchi, K. Watanabe, S. Okamoto, D. Xiao, S.-F. Shi, and Y.-T. Cui, *Correlated Insulating States at Fractional Fillings of the WS2/WSe2 Moir\'e Lattice*, *arXiv:2007.11155 [cond-mat]* (Nov., 2020). arXiv: 2007.11155.

[16] M. Serlin, C. L. Tschirhart, H. Polshyn, Y. Zhang, J. Zhu, K. Watanabe, T. Taniguchi, L. Balents, and A. F. Young, *Intrinsic quantized anomalous Hall effect in a moiré heterostructure*, *Science* **367** (Feb., 2020) 900–903. Publisher: American Association for the Advancement of Science Section: Report.

[17] C. Dean, P. Kim, J. I. A. Li, and A. Young, *Fractional Quantum Hall Effects in Graphene*, in *Fractional Quantum Hall Effects: New Developments*, pp. 317–375. World Scientific, Singapore, Jan., 2020.

[18] H. Polshyn, H. Zhou, E. M. Spanton, T. Taniguchi, K. Watanabe, and A. F. Young, *Quantitative Transport Measurements of Fractional Quantum Hall Energy Gaps in Edgeless Graphene Devices*, *Physical Review Letters* **121** (Nov., 2018) 226801.

[19] H. Zhou, C. Huang, N. Wei, T. Taniguchi, K. Watanabe, M. P. Zaletel, Z. Papić, A. H. MacDonald, and A. F. Young, *Strong-Magnetic-Field Magnon Transport in Monolayer Graphene*, *arXiv:2102.01061 [cond-mat]* (Feb., 2021). arXiv: 2102.01061.

[20] H. Zhou, T. Xie, T. Taniguchi, K. Watanabe, and A. F. Young, *Superconductivity in rhombohedral trilayer graphene*, *Nature* **598** (Oct., 2021) 434–438.

[21] F. Yang, A. A. Zibrov, R. Bai, T. Taniguchi, K. Watanabe, M. P. Zaletel, and A. F. Young, *Experimental Determination of the Energy per Particle in Partially Filled Landau Levels*, *Physical Review Letters* **126** (Apr., 2021) 156802. Publisher: American Physical Society.

[22] K. Zimmermann, A. Jordan, F. Gay, K. Watanabe, T. Taniguchi, Z. Han, V. Bouchiat, H. Sellier, and B. Sacépé, *Tunable transmission of quantum Hall edge channels with full degeneracy lifting in split-gated graphene devices*, *Nature Communications* **8** (Apr., 2017) 14983. Bandiera_abtest: a Cc_license_type: cc_by Cg_type: Nature Research Journals Number: 1 Primary_atype: Research Publisher: Nature Publishing Group Subject_term: Electronic properties and devices;Quantum Hall Subject_term_id: electronic-properties-and-devices;quantum-hall.

[23] C. Déprez, L. Veyrat, H. Vignaud, G. Nayak, K. Watanabe, T. Taniguchi, F. Gay, H. Sellier, and B. Sacépé, *A tunable Fabry-Pérot quantum Hall interferometer in graphene*, *Nature Nanotechnology* **16** (May, 2021) 555–562.

[24] Y. Ronen, T. Werkmeister, D. Haie Najafabadi, A. T. Pierce, L. E. Anderson, Y. J. Shin, S. Y. Lee, Y. H. Lee, B. Johnson, K. Watanabe, T. Taniguchi, A. Yacoby, and P. Kim, *Aharonov-Bohm effect in graphene-based Fabry-Pérot quantum Hall interferometers*, *Nature Nanotechnology* **16** (May, 2021) 563–569.

[25] H. Li, Z. Ying, B. Lyu, A. Deng, L. Wang, T. Taniguchi, K. Watanabe, and Z. Shi, *Electrode-Free Anodic Oxidation Nanolithography of Low-Dimensional Materials*, *Nano Letters* **18** (Dec., 2018) 8011–8015. Publisher: American Chemical Society.

[26] L. A. Cohen, N. L. Samuelson, T. Wang, K. Klocke, C. C. Reeves, T. Taniguchi, K. Wantanbe, S. Vijay, M. P. Zaletel, and A. F. Young, *Nanoscale electrostatic control in ultraclean van der waals heterostructures by local anodic oxidation of graphite gates*, *Nature Physics* **6** (2023), no. 26 1–7.

[27] L. A. Cohen, N. L. Samuelson, T. Wang, T. Taniguchi, K. Watanabe, M. P. Zaletel, and A. F. Young, *Universal chiral Luttinger liquid behavior in a graphene fractional quantum Hall point contact*, *Science* **382** (Nov., 2023) 542–547.

[28] L. A. Cohen, N. L. Samuelson, T. Wang, K. Klocke, C. C. Reeves, T. Taniguchi, K. Watanabe, S. Vijay, M. P. Zaletel, and A. F. Young, *Spontaneous localization at a potential saddle point from edge state reconstruction in a quantum hall point contact*, *ArXiv* **2401** (January, 2024).

[29] L. A. Cohen, N. L. Samuelson, T. Wang, T. Taniguchi, K. Watanabe, M. P. Zaletel, and A. F. Young, *Universal chiral luttinger liquid behaviour in a graphene fractional quantum hall point contact*, *Science* **382** (Nov, 2023) 542–547.

[30] X. G. Wen, *Chiral Luttinger liquid and the edge excitations in the fractional quantum Hall states*, *Physical Review B* **41** (June, 1990) 12838–12844. Publisher: American Physical Society.

[31] C. L. Kane and M. P. A. Fisher, *Transmission through barriers and resonant tunneling in an interacting one-dimensional electron gas*, *Physical Review B* **46** (Dec., 1992) 15233–15262. Publisher: American Physical Society.

[32] F. P. Milliken, C. P. Umbach, and R. A. Webb, *Indications of a Luttinger liquid in the fractional quantum Hall regime*, *Solid State Communications* **97** (Jan., 1996) 309–313.

[33] I. Maasilta and V. Goldman, *Line shape of resonant tunneling between fractional quantum hall edges*, *Phys. Rev. B* **55** (February, 1997).

[34] D. Feldman and B. I. Halperin, *Robustness of quantum hall interferometry*, *Physical Review B* **105** (2022), no. 165310.

[35] S. Nakaharai, J. Williams, and C. Marcus, *Gate-defined graphene quantum point contact in the quantum hall regime*, *Physical Review Letters* **107** (2011), no. 036602.

[36] K. Zimmermann, *Quantum point contact in high mobility graphene*. PhD thesis, Grenoble.

[37] A. M. Chang, *Chiral Luttinger liquids at the fractional quantum Hall edge*, *Reviews of Modern Physics* **75** (Nov., 2003) 1449–1505.

[38] I. P. Radu, J. B. Miller, C. M. Marcus, M. A. Kastner, L. N. Pfeiffer, and K. W. West, *Quasi-Particle Properties from Tunneling in the =5/2 Fractional Quantum Hall State*, *Science* **320** (2008), no. 5878 899–902.

[39] K. Moon, H. Yi, C. L. Kane, S. M. Girvin, and M. P. A. Fisher, *Resonant tunneling between quantum Hall edge states*, *Physical Review Letters* **71** (Dec., 1993) 4381–4384.

[40] L. Wang, I. Meric, P. Y. Huang, Q. Gao, Y. Gao, H. Tran, T. Taniguchi, K. Watanabe, L. M. Campos, D. A. Muller, J. Guo, P. Kim, J. Hone, K. L. Shepard, and C. R. Dean, *One-Dimensional Electrical Contact to a Two-Dimensional Material*, *Science* **342** (Nov., 2013) 614–617.

[41] J. Kim, H. Dev, R. Kumar, A. Haug, V. Bhardwaj, C. Hong, K. Watanabe, T. Taniguchi, A. Stern, and Y. Ronen, *Aharonov-bohm interference and the evolution of phase jumps in fractional quantum hall fabry-perot interferometers based on bi-layer graphene*, *ArXiv* (2024).

[42] R. Held, T. Heinzel, P. Studerus, and K. Ensslin, *Nanolithography by local anodic oxidation of metal films using an atomic force microscope*, *Physica E: Low-dimensional Systems and Nanostructures* **2** (1998), no. 1-4 748–752.

[43] S. Shingubara, Y. Murakami, K. Morimoto, and T. Takahagi, *Formation of aluminum nanodot array by combination of nanoindentation and anodic oxidation of aluminum*, *Surface Science* **532-535** (June, 2003) 317–323.

[44] E. Snow and P. Campbell, *Afm fabrication of sub-10-nanometer metal-oxide devices with in situ control of electrical properties*, *Science* **270** (December, 1995) 1639–1641.

[45] P. Avouris, R. Martel, T. Hertel, and R. Sandstrom, *Afm-tip-induced and current-induced local oxidation of silicon and metals*, *Applied Physics A: Materials Science & Processing* **66** (1997) S659–S667.

[46] J. Dagata, W. Tseng, J. Bennett, J. Schneir, and H. H. Harary, *Nanolithography on iii-v semiconductor surfaces using a scanning tunneling microscope operating in air*, *Journal of Applied Physics* **70** (1991) 3661–3665.

[47] S. Masubuchi, M. Arai, and T. Machida, *Atomic force microscopy based tunable local anodic oxidation of graphene*, *Nano Lett.* **11** (2011), no. 11 4542–4546.

[48] S. Masubuchi, M. Ono, K. Yoshida, K. Hirakawa, and T. Machida, *Fabrication of graphene nanoribbon by local anodic oxidation lithography using atomic force microscope*, *Appl. Phys. Lett.* **94** (2009), no. 082107.

[49] T. Gowthami, M. Gadhewal, and G. Raina, *Study of stability of local anodic oxidation on hopg and few layer graphene using afm in ambient*, *IEEE Transactions on Nanotechnology* **12** (July, 2013) 1002–1006.

[50] M. Arai, S. Masubuchi, K. Nose, Y. Mitsuda, and T. Machida, *Fabrication of 10-nm-scale nanoconstrictions in graphene using atomic force microscopy-based local anodic oxidation lithography*, *Japanese Journal of Applied Physics* **54** (2015), no. 04DJ06.

[51] S. Ko, S. jun Lee, M. Son, D. Ahn, and S.-W. Lee, *Investigation of humidity-dependent size control of local anodic oxidation on graphene by using atomic force microscopy*, *Journal of the Korean Physical Society* **66** (2015) 617–620.

[52] L. Weng, L. Zhang, Y. P. Chen, and L. P. Rokhinson, *Atomic force microscope local oxidation nanolithography of graphene*, *Appl. Phys. Lett.* **93** (2008), no. 093107.

[53] S. Neubeck, L. Ponomarenko, A. Mayorov, S. Morozov, R. Yang, and K.S.Novosolev, *Scanning gate microscopy on a graphene quantum point contact*, *Physica E: Low-dimensional Systems and Nanostructures* **44** (2012) 1002–1004.

[54] A. K. Geim and I. V. Grigorieva, *Van der Waals heterostructures*, *Nature* **499** (2013), no. 7459 419–425.

[55] K. S. Novoselov, A. Mishchenko, A. Carvalho, and A. H. C. Neto, *2D materials and van der Waals heterostructures*, *Science* **353** (July, 2016) aac9439.

[56] Y. Song, D. Mandelli, O. Hod, M. Urbakh, M. Ma, and Q. Zheng, *Robust microscale superlubricity in graphite/hexagonal boron nitride layered heterojunctions*, *Nature Materials* **17** (Oct., 2018) 894–899. Number: 10 Publisher: Nature Publishing Group.

[57] T. Werkmeister, J. R. Ehrets, Y. Ronen, M. E. Wesson, D. Najafabadi, Z. Wei, K. Watanabe, T. Taniguchi, D. Feldman, B. I. Halperin, A. Yacoby, and P. Kim, *Strongly coupled edge states in a graphene quantum hall interferometer*, *ArXiv* (December, 2023).

[58] D. Sedin and K. Rowlen, *Adhesion forces measured by atomic force microscopy in humid air*, *Anal. Chem.* **72** (2000), no. 10 2183–2189.

[59] J. I. A. Li, C. Tan, S. Chen, Y. Zeng, T. Taniguchi, K. Watanabe, J. Hone, and C. R. Dean, *Even denominator fractional quantum Hall states in bilayer graphene*, *Science* (Oct., 2017) eaao2521.

[60] J. I. A. Li, T. Taniguchi, K. Watanabe, J. Hone, and C. R. Dean, *Excitonic superfluid phase in double bilayer graphene*, *Nature Physics* **13** (Aug., 2017) 751–755.

[61] X. Liu, K. Watanabe, T. Taniguchi, B. I. Halperin, and P. Kim, *Quantum Hall drag of exciton condensate in graphene*, *Nature Physics* **13** (Aug., 2017) 746–750.

[62] T. Li, S. Jiang, B. Shen, Y. Zhang, L. Li, Z. Tao, T. Devakul, K. Watanabe, T. Taniguchi, L. Fu, J. Shan, and K. F. Mak, *Quantum anomalous Hall effect from intertwined moiré bands*, *Nature* **600** (Dec., 2021) 641–646. Number: 7890 Publisher: Nature Publishing Group.

[63] E. M. Spanton, A. A. Zibrov, H. Zhou, T. Taniguchi, K. Watanabe, M. P. Zaletel, and A. F. Young, *Observation of fractional Chern insulators in a van der Waals heterostructure*, *Science* **360** (Apr., 2018) 62–66.

[64] Y. Xie, A. T. Pierce, J. M. Park, D. E. Parker, E. Khalaf, P. Ledwith, Y. Cao, S. H. Lee, S. Chen, P. R. Forrester, K. Watanabe, T. Taniguchi, A. Vishwanath, P. Jarillo-Herrero, and A. Yacoby, *Fractional Chern insulators in magic-angle*

twisted bilayer graphene, *Nature* **600** (Dec., 2021) 439–443. Number: 7889 Publisher: Nature Publishing Group.

[65] M. Yankowitz, S. Chen, H. Polshyn, Y. Zhang, K. Watanabe, T. Taniguchi, D. Graf, A. F. Young, and C. R. Dean, *Tuning superconductivity in twisted bilayer graphene*, *Science* **363** (Mar., 2019) 1059–1064.

[66] H. Zhou, L. Holleis, Y. Saito, L. Cohen, W. Huynh, C. L. Patterson, F. Yang, T. Taniguchi, K. Watanabe, and A. F. Young, *Isospin magnetism and spin-polarized superconductivity in Bernal bilayer graphene*, *Science* **375** (Feb., 2022) 774–778. Publisher: American Association for the Advancement of Science.

[67] Y. Zhang, R. Polski, A. Thomson, É. Lantagne-Hurtubise, C. Lewandowski, H. Zhou, K. Watanabe, T. Taniguchi, J. Alicea, and S. Nadj-Perge, *Spin-Orbit Enhanced Superconductivity in Bernal Bilayer Graphene*, May, 2022. Number: arXiv:2205.05087 arXiv:2205.05087 [cond-mat].

[68] A. S. Mayorov, R. V. Gorbachev, S. V. Morozov, L. Britnell, R. Jalil, L. A. Ponomarenko, P. Blake, K. S. Novoselov, K. Watanabe, T. Taniguchi, and A. K. Geim, *Micrometer-Scale Ballistic Transport in Encapsulated Graphene at Room Temperature*, *Nano Letters* **11** (June, 2011) 2396–2399.

[69] S. J. Haigh, A. Gholinia, R. Jalil, S. Romani, L. Britnell, D. C. Elias, K. S. Novoselov, L. A. Ponomarenko, A. K. Geim, and R. Gorbachev, *Cross-sectional imaging of individual layers and buried interfaces of graphene-based heterostructures and superlattices*, *Nat Mater* **11** (Oct., 2012) 764–767.

[70] H.-J. Butt, M. Farshchi-Tabrizi, and M. Kappl, *Using capillary forces to determine the geometry of nanocontacts*, *Journal of Applied Physics* **100** (July, 2006) 024312. Publisher: American Institute of Physics.

[71] B. J. van Wees, H. van Houten, C. W. J. Beenakker, J. G. Williamson, L. P. Kouwenhoven, D. van der Marel, and C. T. Foxon, *Quantized conductance of point contacts in a two-dimensional electron gas*, *Phys. Rev. Lett.* **60** (Feb., 1988) 848–850.

[72] S. Datta, *Electronic Transport in Mesoscopic Systems*. Cambridge Studies in Semiconductor Physics and Microelectronic Engineering. Cambridge University Press, Cambridge, 1995.

[73] S. Baer, C. Rössler, E. C. de Wiljes, P.-L. Ardelt, T. Ihn, K. Ensslin, C. Reichl, and W. Wegscheider, *Interplay of fractional quantum hall states and localization in quantum point contacts*, *Phys. Rev. B* **89** (Feb, 2014) 085424.

[74] M. D. Johnson and A. H. MacDonald, *Composite edges in the =2/3 fractional quantum Hall effect*, *Physical Review Letters* **67** (Oct., 1991) 2060–2063.

[75] C. L. Kane, M. P. A. Fisher, and J. Polchinski, *Randomness at the edge: Theory of quantum Hall transport at filling =2/3*, *Phys. Rev. Lett.* **72** (June, 1994) 4129–4132.

[76] J. Nakamura, S. Liang, G. Gardner, and M. Manfra, *Half-integer conductance plateau at the = 2 / 3 fractional quantum hall state in a quantum point contact*, *Physical Review Letters* **130** (February, 2023).

[77] R. Sabo, I. Gurman, A. Rosenblatt, F. Lafont, D. Banitt, J. Park, M. Heiblum, Y. Gefen, V. Umansky, and D. Mahalu, *Edge reconstruction in fractional quantum Hall states*, *Nature Physics* **13** (May, 2017) 491–496.

[78] C. d. C. Chamon and X. G. Wen, *Sharp and smooth boundaries of quantum Hall liquids*, *Physical Review B* **49** (Mar., 1994) 8227–8241.

[79] Y. Meir, *Composite edge states in the = 2/3 fractional quantum Hall regime*, *Physical Review Letters* **72** (Apr., 1994) 2624–2627. Publisher: American Physical Society.

[80] C. L. Kane and M. P. A. Fisher, *Edge-State Transport*, in *Perspectives in Quantum Hall Effects*, pp. 109–159. John Wiley & Sons, Ltd, 1996.

[81] J. M. Luttinger, *An Exactly Soluble Model of a Many-Fermion System*, *Journal of Mathematical Physics* **4** (Sept., 1963) 1154–1162. Publisher: American Institute of Physics.

[82] S. Roddaro, V. Pellegrini, F. Beltram, G. Biasiol, L. Sorba, R. Raimondi, and G. Vignale, *Nonlinear quasiparticle tunneling between fractional quantum hall edges*, *Phys. Rev. Lett.* **90** (Jan, 2003) 046805.

[83] S. Baer, C. Rössler, T. Ihn, K. Ensslin, C. Reichl, and W. Wegscheider, *Experimental probe of topological orders and edge excitations in the second landau level*, *Phys. Rev. B* **90** (Aug, 2014) 075403.

[84] X.-G. Wen, *Theory of the edge states in fractional quantum hall effects*, *International Journal of Modern Physics B* **06** (May, 1992) 1711–1762. Publisher: World Scientific Publishing Co.

[85] A. M. Chang, L. N. Pfeiffer, and K. W. West, *Observation of Chiral Luttinger Behavior in Electron Tunneling into Fractional Quantum Hall Edges*, *Physical Review Letters* **77** (Sept., 1996) 2538–2541. Publisher: American Physical Society.

[86] A. M. Chang, M. K. Wu, C. C. Chi, L. N. Pfeiffer, and K. W. West, *Plateau Behavior in the Chiral Luttinger Liquid Exponent*, *Physical Review Letters* **86** (Jan., 2001) 143–146. Publisher: American Physical Society.

[87] R. Bhattacharyya, M. Banerjee, M. Heiblum, D. Mahalu, and V. Umansky, *Melting of Interference in the Fractional Quantum Hall Effect: Appearance of Neutral Modes*, *Physical Review Letters* **122** (June, 2019) 246801. Publisher: American Physical Society.

[88] V. Venkatachalam, S. Hart, L. Pfeiffer, K. West, and A. Yacoby, *Local thermometry of neutral modes on the quantum Hall edge*, *Nature Physics* **8** (Oct., 2012) 676–681.

[89] Z.-X. Hu, R. N. Bhatt, X. Wan, and K. Yang, *Realizing Universal Edge Properties in Graphene Fractional Quantum Hall Liquids*, *Physical Review Letters* **107** (Dec., 2011) 236806.

[90] G. Li, A. Luican-Mayer, D. Abanin, L. Levitov, and E. Y. Andrei, *Evolution of Landau levels into edge states in graphene*, *Nature Communications* **4** (Apr., 2013).

[91] A. Coissard, A. G. Grushin, C. Repellin, L. Veyrat, K. Wantanabe, T. Taniguchi, F. Gay, H. Courtois, H. Sellier, and B. Sacépé, *Absence of edge reconstruction for quantum hall edge channels in graphene devices*, *Science Advances* **9** (May, 2023).

[92] M. Flöser, T. Champel, and S. Florens, *Transmission coefficient through a saddle-point electrostatic potential for graphene in the quantum Hall regime*, *Physical Review B* **82** (Oct., 2010) 161408. arXiv: 1009.1713.

[93] S. S. Hegde, V. Subramanyan, B. Bradlyn, and S. Vishveshwara, *Quasinormal Modes and the Hawking-Unruh Effect in Quantum Hall Systems: Lessons from Black Hole Phenomena*, *Physical Review Letters* **123** (Oct., 2019) 156802. Publisher: American Physical Society.

[94] U. Khanna, M. Goldstein, and Y. Gefen, *Fractional edge reconstruction in integer quantum Hall phases*, *Physical Review B* **103** (Mar., 2021) L121302.

[95] L. Zhao, E. G. Arnault, T. F. Q. Larson, Z. Iftikhar, A. Seredinski, T. Fleming, K. Watanabe, T. Taniguchi, F. Amet, and G. Finkelstein, *Graphene-based quantum Hall interferometer with self-aligned side gates*, June, 2022. arXiv:2206.05623 [cond-mat, physics:quant-ph].

[96] S. itiro Tomonaga, *Remarks on bloch's method of sound waves applied to many-fermion problems*, *Progress of Theoretical Physics* **5** (July, 1950) 544–569.

[97] T. Giamarchi, T. Nattermann, and P. L. Doussal, *Quantum Physics in One Dimension.* Clarendon Press - Oxford, 2003.

[98] M. P. A. Fisher and L. I. Glazman, *Transport in a One-Dimensional Luttinger Liquid*, in *Mesoscopic Electron Transport* (L. L. Sohn, L. P. Kouwenhoven, and G. Schön, eds.), NATO ASI Series, pp. 331–373. Springer Netherlands, Dordrecht, 1997.

[99] M. Bockrath, D. H. Cobden, J. Lu, A. G. Rinzler, R. E. Smalley, L. Balents, and P. L. McEuen, *Luttinger-liquid behaviour in carbon nanotubes*, *Nature* **397** (Feb., 1999) 598–601. Number: 6720 Publisher: Nature Publishing Group.

[100] H. I. et. al., *Direct observation of tomonaga–luttinger-liquid state in carbon nanotubes at low temperatures*, *Nature* **426** (2003) 540–544.

[101] B. I. Halperin, *Quantized Hall conductance, current-carrying edge states, and the existence of extended states in a two-dimensional disordered potential*, *Phys. Rev. B* **25** (Feb., 1982) 2185–2190.

[102] M. Grayson, D. C. Tsui, L. N. Pfeiffer, K. W. West, and A. M. Chang, *Continuum of Chiral Luttinger Liquids at the Fractional Quantum Hall Edge*, *Physical Review Letters* **80** (Feb., 1998) 1062–1065. Publisher: American Physical Society.

[103] V. J. Goldman and E. V. Tsiper, *Dependence of the Fractional Quantum Hall Edge Critical Exponent on the Range of Interaction*, *Physical Review Letters* **86** (June, 2001) 5841–5841. Publisher: American Physical Society.

[104] S. S. Mandal and J. K. Jain, *Relevance of Inter-Composite-Fermion Interaction to the Edge Tomonaga-Luttinger Liquid*, *Physical Review Letters* **89** (Aug., 2002) 096801. Publisher: American Physical Society.

[105] S. Jolad and J. K. Jain, *Testing the Topological Nature of the Fractional Quantum Hall Edge*, *Physical Review Letters* **102** (Mar., 2009) 116801. Publisher: American Physical Society.

[106] X. Wan, F. Evers, and E. H. Rezayi, *Universality of the Edge-Tunneling Exponent of Fractional Quantum Hall Liquids*, *Physical Review Letters* **94** (Apr., 2005) 166804. Publisher: American Physical Society.

[107] D. Varjas, M. P. Zaletel, and J. E. Moore, *Chiral Luttinger liquids and a generalized Luttinger theorem in fractional quantum Hall edges via finite-entanglement scaling*, *Physical Review B* **88** (Oct., 2013) 155314. Publisher: American Physical Society.

[108] L. A. Cohen, N. L. Samuelson, T. Wang, K. Klocke, C. C. Reeves, T. Taniguchi, K. Watanabe, S. Vijay, M. P. Zaletel, and A. F. Young, *Tunable fractional quantum Hall point contacts in graphene via local anodic oxidation of graphite gates*, *arXiv:2204.10296 [cond-mat]* (Apr., 2022). arXiv: 2204.10296.

[109] D.-H. Lee and X.-G. Wen, *Edge excitations in the fractional-quantum-Hall liquids*, *Physical Review Letters* **66** (Apr., 1991) 1765–1768.

[110] I. Safi, *Propriétés d'un fil quantique connecté à des fils de mesure*, *Annales de Physique* **22** (1997), no. 5 463–679.

[111] C. d. C. Chamon and E. Fradkin, *Distinct universal conductances in tunneling to quantum Hall states: The role of contacts*, *Physical Review B* **56** (July, 1997) 2012–2025. Publisher: American Physical Society.

[112] N. P. Sandler, C. d. C. Chamon, and E. Fradkin, *Andreev reflection in the fractional quantum Hall effect*, *Physical Review B* **57** (May, 1998) 12324–12332.

[113] J. B. Miller, I. P. Radu, D. M. Zumbühl, E. M. Levenson-Falk, M. A. Kastner, C. M. Marcus, L. N. Pfeiffer, and K. W. West, *Fractional quantum Hall effect in a quantum point contact at filling fraction 5/2*, *Nature Physics* **3** (Aug., 2007) 561–565.

[114] M. Hashisaka, T. Jonckheere, T. Akiho, S. Sasaki, J. Rech, T. Martin, and K. Muraki, *Andreev reflection of fractional quantum Hall quasiparticles*, *Nature Communications* **12** (May, 2021) 2794.

[115] X. Wan, E. H. Rezayi, and K. Yang, *Edge reconstruction in the fractional quantum Hall regime*, *Physical Review B* **68** (Sept., 2003) 125307.

[116] K. Yang, *Field theoretical description of quantum hall edge reconstruction*, *Physical Review Letters* **91** (July, 2003).

[117] H. Overweg, H. Eggimann, X. Chen, S. Slizovskiy, M. Eich, R. Pisoni, Y. Lee, P. Rickhaus, K. Watanabe, T. Taniguchi, V. Fal'ko, T. Ihn, and K. Ensslin, *Electrostatically Induced Quantum Point Contacts in Bilayer Graphene*, *Nano Letters* **18** (Jan., 2018) 553–559.

[118] X. Wan, K. Yang, and E. Rezayi, *Reconstruction of fractional quantum hall edges*, *Physical Review Letters* **88** (February, 2002).

[119] L. Cohen, *Supplementary Information*, *Supplementary Information* (2022).

[120] M. Milovanović and N. Read, *Edge excitations of paired fractional quantum Hall states*, *Physical Review B* **53** (May, 1996) 13559–13582. Publisher: American Physical Society.

[121] D. B. Chklovskii and B. I. Halperin, *Consequences of a possible adiabatic transition between =1/3 and =1 quantum Hall states in a narrow wire*, *Physical Review B* **57** (Feb., 1998) 3781–3784.

[122] P. Fendley, H. Saleur, and N. P. Warner, *Exact solution of a massless scalar field with a relevant boundary interaction*, *Nuclear Physics B* **430** (Nov., 1994) 577–596.

[123] C. L. Kane, *Resonant Tunneling between quantum Hall states at filling \nu = 1 and \nu = 1/3*, Sept., 1998. arXiv:cond-mat/9809020.

[124] B. I. Halperin, A. Stern, and S. M. Girvin, *dc voltage step-up transformer based on a bilayer = 1 quantum Hall system*, *Physical Review B* **67** (June, 2003) 235313.

[125] I. Giaever, *A dc transformer*, *IEEE Spectrum* **3** (Sept., 1966) 117–122. Conference Name: IEEE Spectrum.

[126] S. M. Girvin, *DC Transformer and DC Josephson(-like) Effects in Quantum Hall Bilayers*, *Physica Scripta* **2002** (Jan., 2002) 112.

[127] Y. Kim, A. C. Balram, T. Taniguchi, K. Watanabe, J. K. Jain, and J. H. Smet, *Even denominator fractional quantum Hall states in higher Landau levels of graphene*, *Nature Physics* **15** (Feb., 2019) 154–158.

[128] D.-K. Ki, V. I. Fal'ko, D. A. Abanin, and A. F. Morpurgo, *Observation of Even Denominator Fractional Quantum Hall Effect in Suspended Bilayer Graphene*, *Nano Letters* **14** (Apr., 2014) 2135–2139.

[129] X.-G. Wen, *Topological order and edge structure of \ensuremath{\nu}=1/2 quantum Hall state*, *Physical Review Letters* **70** (Jan., 1993) 355–358. Publisher: American Physical Society.

[130] P. Fendley, M. P. A. Fisher, and C. Nayak, *Dynamical Disentanglement across a Point Contact in a Non-Abelian Quantum Hall State*, *Physical Review Letters* **97** (July, 2006) 036801. Publisher: American Physical Society.

[131] R. Ohashi, R. Nakai, T. Yokoyama, Y. Tanaka, and K. Nomura, *Andreev-like Reflection in the Pfaffian Fractional Quantum Hall Effect*, Aug., 2022. arXiv:2208.03336 [cond-mat].

[132] W. Bishara and C. Nayak, *Edge states and interferometers in the Pfaffian and anti-Pfaffian states of the $\ensuremath{\nu}=\frac{5}{2}$ quantum Hall system*, *Physical Review B* **77** (Apr., 2008) 165302. Publisher: American Physical Society.

[133] C. Nayak, S. H. Simon, A. Stern, M. Freedman, and S. Das Sarma, *Non-Abelian anyons and topological quantum computation*, *Reviews of Modern Physics* **80** (Oct., 2008) 1083–1159.

[134] J. Nakamura, S. Fallahi, H. Sahasrabudhe, R. Rahman, S. Liang, G. C. Gardner, and M. J. Manfra, *Aharonov–Bohm interference of fractional quantum Hall edge modes*, *Nature Physics* **15** (June, 2019) 563–569.

[135] J. M. Leinaas and J. Myrheim, *On the theory of identical particles*, *Il Nuovo Cimento B* **37** (1977), no. 1 1–23.

[136] F. Wilczek, *Quantum Mechanics of Fractional-Spin Particles*, *Physical Review Letters* **49** (Oct., 1982) 957–959.

[137] D. Arovas, J. R. Schrieffer, and F. Wilczek, *Fractional Statistics and the Quantum Hall Effect*, *Physical Review Letters* **53** (Aug., 1984) 722–723. Publisher: American Physical Society.

[138] B. I. Halperin, *Statistics of Quasiparticles and the Hierarchy of Fractional Quantized Hall States*, *Physical Review Letters* **52** (Apr., 1984) 1583–1586. Publisher: American Physical Society.

[139] S. Kivelson, *Semiclassical theory of localized many-anyon states*, *Physical Review Letters* **65** (Dec., 1990) 3369–3372. Publisher: American Physical Society.

[140] C. d. C. Chamon, D. E. Freed, S. A. Kivelson, S. L. Sondhi, and X. G. Wen, *Two point-contact interferometer for quantum Hall systems*, *Physical Review B* **55** (Jan., 1997) 2331–2343.

[141] E.-A. Kim, *Aharanov-Bohm Interference and Fractional Statistics in a Quantum Hall Interferometer*, *Physical Review Letters* **97** (Nov., 2006) 216404. Publisher: American Physical Society.

[142] B. I. Halperin, A. Stern, I. Neder, and B. Rosenow, *Theory of the Fabry-Perot quantum Hall interferometer*, *Physical Review B* **83** (Apr., 2011) 155440.

[143] N. Read and S. D. Sarma, *A perspective on anyonic braiding statistics*, Aug., 2023. arXiv:2308.12986 [cond-mat].

[144] J. Nakamura, S. Liang, G. C. Gardner, and M. J. Manfra, *Direct observation of anyonic braiding statistics*, *Nature Physics* **16** (Sept., 2020) 931–936. Bandiera_abtest: a Cg_type: Nature Research Journals Number: 9 Primary_atype: Research Publisher: Nature Publishing Group Subject_term: Quantum Hall;Quantum information Subject_term_id: quantum-hall;quantum-information.

[145] J. Nakamura, S. Liang, G. Gardner, and M. Manfra, *Fabry-Pérot Interferometry at the =2/5 Fractional Quantum Hall State*, *Physical Review X* **13** (Oct., 2023) 041012. Publisher: American Physical Society.

[146] N. Ofek, A. Bid, M. Heiblum, A. Stern, V. Umansky, and D. Mahalu, *Role of interactions in an electronic Fabry–Perot interferometer operating in the quantum Hall effect regime*, *Proceedings of the National Academy of Sciences* **107** (Mar., 2010) 5276–5281.

[147] H. K. Choi, I. Sivan, A. Rosenblatt, M. Heiblum, V. Umansky, and D. Mahalu, *Robust electron pairing in the integer quantum hall effect regime*, *Nature Communications* **6** (June, 2015).

[148] J. Nakamura, S. Liang, G. C. Gardner, and M. J. Manfra, *Impact of bulk-edge coupling on observation of anyonic braiding statistics in quantum Hall interferometers*, *Nature Communications* **13** (Jan., 2022) 344. Publisher: Nature Publishing Group.

[149] H. Fu, K. Huang, K. Watanabe, T. Taniguchi, M. Kayyalha, and J. Zhu, *Aharonov–Bohm Oscillations in Bilayer Graphene Quantum Hall Edge State Fabry–Pérot Interferometers*, *Nano Letters* **23** (Jan., 2023) 718–725.

[150] J. Kim, H. Dev, R. Kumar, A. Ilin, A. Haug, V. Bhardwaj, C. Hong, K. Watanabe, T. Taniguchi, A. Stern, and Y. Ronen, *Aharonov-Bohm interference and the evolution of phase jumps in fractional quantum Hall Fabry-Perot interferometers based on bi-layer graphene*, Feb., 2024. arXiv:2402.12432 [cond-mat].